

Experimental characterization of material by means of shear testing at intermediate strain rate and elevated temperatures

# Experimental characterization of material by means of shear testing at intermediate strain rate and elevated temperatures

**Ph.D. THESIS**

presented to obtain the degree of

**Doctor**

**Dhawale Trunal Bhujangrao**



*11/2021, Bilbao*

**THESIS ADVISOR**

Prof. Franck Andrés Girot Mata, University of the Basque Country-UPV/EHU

Dr. Catherine Froustey, University of Bordeaux, I2M, France

**Dhawale Trunal Bhujangrao**



Universidad del País Vasco Euskal Herriko Unibertsitatea

Departamento de Ingeniería Mecánica / Ingeniaritza Mekanikoa Saila



Universidad del País Vasco Euskal Herriko Unibertsitatea

INGENIARITZA  
MEKANIKOA  
SAILA  
DEPARTAMENTO  
DE INGENIERÍA  
MECÁNICA



Universidad  
del País Vasco

Euskal Herriko  
Unibertsitatea

BILBOKO  
INGENIARITZA  
ESKOLA  
ESCUELA  
DE INGENIERÍA  
DE BILBAO

**Doctoral Thesis**

**Experimental characterization of material by  
means of shear testing at intermediate strain rate  
and elevated temperatures**

Presented by:

**Dhawale Trunal Bhujangrao**

at the

**Department of Mechanical Engineering**

belonging to the

**Universidad del País Vasco – Euskal Herriko Unibertsitatea**

In order to obtain the degree of

**Doctor from the UPV/EHU**

Directed by

**Prof. Franck Girot Mata**

**Dr. Catherine Froustey**

Bilbao, November 2021



## ACKNOWLEDGEMENT

First of all, I would like to thank my thesis directors Prof. Franck Andrés Girot Mata and Dr. Catherine Froustey for their guidance, dedicated support, and invaluable advice. Without them, it is impossible for me to complete the thesis. It is really a pleasure for me to work here with them for such a long time.

Second, I would like to thank the ENABLE project for providing the funding (the European Union's Horizon 2020 research and innovation program under Marie Skłodowska-Curie grant agreement N°764979) to support my studies. I thank Olivier Cahuc and Sara Marin, responsible for the ENABLE project, as well as all the ESRs and members of this project with whom the exchange of knowledge has been enriching.

I would like to thank my supervisory team, from Tecnalía, Spain, the support and trust in me to carry out my work without any hesitation and hosting me as an early stage researcher. I would also like to thank the professors from University of Bordeaux, France for all the advice on the design of the parts and our numerous discussions which allowed us to decide on the technological choice for the torsion device. Special thanks to the Prof. Paul Åkerström and Lars-Erik Lindgren from Luleå University of Technology, Sweden, who provided me with knowledge on material modeling and helped me during my stay in Luleå.

An experimental thesis is obviously not realized in an autonomous way, and most of my work is conducted in the I2M laboratory in Bordeaux, on the site of the École des Arts et Métiers - ParisTech of Bordeaux Talence. Therefore, I would like to thank all the technicians and engineers, Jonathan Merzeau, for the precision work, who took the time to teach me everything about the experimental testing, Jérémie Béga, for his help in micrography and polishing and his various advices, Frederic Pinassou, for the manufacturing of the metallic parts, who have all been of great support throughout this thesis and who are more than colleagues.

A thesis is above all an extraordinary human adventure and for that I would like to thank all the researchers, doctoral and post-doctoral students who have helped me in my work and who have grown together in this adventure.

## Acknowledgement

I am extremely grateful to my family, my father, my mother, my sister and newly born my little niece. I grow up under their encouragement, support and sacrifice.

Last but not least, I also want to thank all the people who helped me and filled my life with laugh and happiness.

## ABSTRACT

The PhD is a part of the ENABLE (European Network for Alloys Behaviour Law Enhancement) project which received funding from the European Union's Horizon 2020 research and innovation programme under the Marie Skłodowska-Curie grant agreement N°764979. The work has also been developed within the framework of the joint cross-border laboratory LTC ÆNIGME, between the University of the Basque Country (UPV/EHU), the University of Burgos (UBx) and Arts et Métiers Science et Technologie (ENSAM). The aim of the PhD is to experimental characterize the shear behaviour of an aluminium alloy (AA7075-T6), in the range of intermediate strain rate ( $10^1$ - $10^3$ s<sup>-1</sup>)and elevated temperature (up to 0.7 times the melting temperature).

The manufacturing of metallic components often involves material deformation at medium to high strain rates and high temperatures, especially for the processes of forming, machining, friction stir welding (FSW), etc. Moreover, in a lot of manufacturing processes, the deformation within the material is generated by shear stress and not by tensile or compressive stresses. But, exiting mechanical testing devices are not able to provide complete material behaviour history occurred during the manufacturing process in the range of strain rate and temperature.

The main technological and scientific steps to overcome concern :

- Design and development of a new experimental test bench to perform the shear test at intermediate strain rate.
- The definition of thermomechanical tests able to reproduce the same solicitations as during machining (medium strain rate and medium range deformation), FSW (medium strain rate, high deformation), etc.
- To provide a detailed experimental behaviour of material and perform microstructural investigations.

A new experimental torsion test device based on the principle of the inertia flywheel wheel is developed to reproduce locally the stress levels and strain rates encountered in processes such as machining or FSW. In a first step, this device allows, by means of torsional stress, to achieve deformations at average deformation speeds (in the range of  $10^2$ - $10^3$  s<sup>-1</sup>).

An evolution will then be made to perform temperature tests (up to 0.7 times the melting temperature for the three alloys studied). The novelty of this equipment lies in the dynamic tests in torsion that can be carried out under intermediate strain rates by controlling the speed of loading. Strain in the sample will be measured by means of high-speed recording camera and load is measured by using the Hopkinson bar technique. The new test bench is implemented on the dynamic platform present in the I2M, Bordeaux, France.

After the manufacturing of the test device, the calibration of the different measuring components is carried out in order to obtain accurate torque and strain results. Finally, the preliminary tests are performed. Once the test bench has been validated, room temperature and high temperature tests are carried out. For this purpose, the design of the experiment (DOE) is adopted, in order to optimize and organize tests campaign. The tests are performed at different loading speeds and temperatures. Several microstructural investigations are also performed in order to clearly identify the mechanisms governing the evolution for plastic response covering a wide range of temperature, strain, and strain rates. Mechanical and microstructural characterization of the material is thoroughly studied.

Finally, the flow stress curves obtained from the new torsion test bench at different strain rates and at different temperatures compared with the classic existing material models commonly used for constitutive behavior modelling of AA7075-T6. The parameters for the material models are experimentally determined. The comparison with the experimental results allows to evaluate the adequacy of the existing models and to propose a baseline for the improvement of the existing model or the development of a new material model.

## Resumen

El doctorado forma parte del proyecto ENABLE (European Network for Alloys Behaviour Law Enhancement) que ha recibido financiación del programa de investigación e innovación Horizon 2020 de la Unión Europea bajo el acuerdo de subvención Marie Skłodowska-Curie N°764979. El trabajo también se ha desarrollado en el marco del laboratorio transfronterizo conjunto LTC ÆNIGME, entre la Universidad del País Vasco (UPV/EHU), la Universidad de Burgos (UBx) y Arts et Métiers Science et Technologie (ENSAM). El objetivo del doctorado es caracterizar experimentalmente el comportamiento a cizalla de una aleación de aluminio (AA7075-T6), en el rango de velocidad de deformación intermedia ( $10^1$ - $10^3$ s<sup>-1</sup>) y temperatura elevada (hasta 0,7 veces la temperatura de fusión).

La fabricación de componentes metálicos implica a menudo la deformación del material a velocidades de deformación de medias a altas y a temperaturas elevadas, especialmente en los procesos de conformación, mecanizado, soldadura por fricción (FSW), etc. Además, en muchos procesos de fabricación, la deformación dentro del material se genera por esfuerzos de cizallamiento y no por esfuerzos de tracción o compresión. Sin embargo, los dispositivos de ensayo mecánico existentes no son capaces de proporcionar un historial completo del comportamiento del material durante el proceso de fabricación en el rango de la velocidad de deformación y la temperatura.

Los principales pasos tecnológicos y científicos para superar la preocupación:

- Diseño y desarrollo de un nuevo banco de pruebas experimental para realizar el ensayo de cizallamiento a una velocidad de deformación intermedia.
- La definición de ensayos termomecánicos capaces de reproducir las mismas sollicitaciones que durante el mecanizado (velocidad de deformación media y deformación de rango medio), FSW (velocidad de deformación media, alta deformación), etc.
- Proporcionar un comportamiento experimental detallado del material y realizar investigaciones microestructurales.

Se desarrolla un nuevo dispositivo experimental de prueba de torsión basado en el principio de la rueda volante de inercia para reproducir localmente los niveles de tensión y las tasas de deformación que se encuentran en procesos como el mecanizado o el FSW. En una primera etapa, este dispositivo permite, mediante esfuerzos de torsión, alcanzar deformaciones a velocidades de deformación medias (en el rango de  $10^2$ - $10^3$ s<sup>-1</sup>). A



continuación, se realizará una evolución para realizar ensayos de temperatura (hasta 0,7 veces la temperatura de fusión para las tres aleaciones estudiadas). La novedad de este equipo radica en los ensayos dinámicos en torsión que pueden realizarse bajo velocidades de deformación intermedias controlando la velocidad de carga. La deformación de la muestra se mide mediante una cámara de grabación de alta velocidad y la carga se mide mediante la técnica de la barra de Hopkinson. El nuevo banco de pruebas se implementa en la plataforma dinámica presente en el I2M, Burdeos, Francia.

Tras la fabricación del dispositivo de prueba, se lleva a cabo la calibración de los diferentes componentes de medición para obtener resultados precisos de par y deformación. Por último, se realizan las pruebas preliminares. Una vez validado el banco de pruebas, se realizan ensayos a temperatura ambiente y a alta temperatura. Para ello, se adopta el diseño del experimento (DOE), con el fin de optimizar y organizar la campaña de ensayos. Los ensayos se realizan a diferentes velocidades de carga y temperaturas. También se realizan varias investigaciones microestructurales con el fin de identificar claramente los mecanismos que rigen la evolución de la respuesta plástica cubriendo un amplio rango de temperaturas, deformaciones y velocidades de deformación. Se estudia a fondo la caracterización mecánica y microestructural del material.

Por último, se comparan las curvas de tensión de flujo obtenidas en el nuevo banco de ensayos de torsión a diferentes velocidades de deformación y a diferentes temperaturas con los modelos clásicos de material existentes que se utilizan habitualmente para la modelización del comportamiento constitutivo del AA7075-T6. Los parámetros de los modelos de material se determinan experimentalmente. La comparación con los resultados experimentales permite evaluar la adecuación de los modelos existentes y proponer una línea de base para la mejora del modelo existente o el desarrollo de un nuevo modelo de material.

## Résumé

Le doctorat fait partie du projet ENABLE (European Network for Alloys Behaviour Law Enhancement) qui a reçu un financement du programme de recherche et d'innovation Horizon 2020 de l'Union européenne sous la convention de subvention Marie Skłodowska-Curie N°764979. Les travaux ont également été développés dans le cadre du laboratoire commun transfrontalier LTC ÆNIGME, entre l'Université du Pays basque (UPV/EHU), l'Université de Burgos (UBx) et Arts et Métiers Science et Technologie (ENSAM). L'objectif du doctorat est de caractériser expérimentalement le comportement au cisaillement d'un alliage d'aluminium (AA7075-T6), dans la gamme de vitesse de déformation intermédiaire ( $10^1$ - $10^3$ s<sup>-1</sup>) et de température élevée (jusqu'à 0,7 fois la température de fusion).

La fabrication de composants métalliques implique souvent une déformation du matériau à des vitesses de déformation moyennes à élevées et à des températures élevées, notamment pour les processus de formage, d'usinage, de soudage par friction-malaxage (FSW), etc. De plus, dans de nombreux procédés de fabrication, la déformation du matériau est générée par une contrainte de cisaillement et non par des contraintes de traction ou de compression. Mais les dispositifs d'essais mécaniques existants ne sont pas en mesure de fournir l'historique complet du comportement du matériau au cours du processus de fabrication dans la plage de vitesse de déformation et de température.

Les principales mesures technologiques et scientifiques à prendre pour résoudre ce problème sont les suivantes :

- La conception et le développement d'un nouveau banc d'essai expérimental pour réaliser l'essai de cisaillement à une vitesse de déformation intermédiaire.
- La définition de tests thermomécaniques capables de reproduire les mêmes sollicitations que lors de l'usinage (vitesse de déformation moyenne et déformation de gamme moyenne), FSW (vitesse de déformation moyenne, déformation élevée), etc.
- Fournir un comportement expérimental détaillé du matériau et réaliser des études microstructurales.

Un nouveau dispositif expérimental de test de torsion basé sur le principe du volant d'inertie est développé pour reproduire localement les niveaux de contrainte et les taux de déformation rencontrés dans des processus tels que l'usinage ou la FSW. Dans un premier

temps, ce dispositif permet, au moyen d'une contrainte de torsion, de réaliser des déformations à des vitesses de déformation moyennes (de l'ordre de  $10^2$ - $10^3$ s<sup>-1</sup>). Une évolution sera ensuite faite pour réaliser des essais en température (jusqu'à 0,7 fois la température de fusion pour les trois alliages étudiés). La nouveauté de cet équipement réside dans les essais dynamiques en torsion qui peuvent être réalisés sous des taux de déformation intermédiaires en contrôlant la vitesse de chargement. La déformation de l'échantillon sera mesurée au moyen d'une caméra d'enregistrement à haute vitesse et la charge sera mesurée en utilisant la technique de la barre d'Hopkinson. Le nouveau banc d'essai est implémenté sur la plateforme dynamique présente à l'I2M, Bordeaux, France.

Après la fabrication du dispositif d'essai, la calibration des différents composants de mesure est effectuée afin d'obtenir des résultats précis de couple et de déformation. Enfin, les essais préliminaires sont réalisés. Une fois le banc d'essai validé, des essais à température ambiante et à haute température sont réalisés. Pour ce faire, le plan d'expérience (DOE) est adopté, afin d'optimiser et d'organiser la campagne d'essais. Les essais sont réalisés à différentes vitesses et températures de chargement. Plusieurs études microstructurales sont également réalisées afin d'identifier clairement les mécanismes régissant l'évolution de la réponse plastique couvrant une large gamme de température, de déformation et de taux de déformation. La caractérisation mécanique et microstructurale du matériau est étudiée de manière approfondie.

Enfin, les courbes de contrainte d'écoulement obtenues à partir du nouveau banc d'essai de torsion à différents taux de déformation et à différentes températures sont comparées aux modèles de matériaux classiques existants couramment utilisés pour la modélisation du comportement constitutif du AA7075-T6. Les paramètres des modèles de matériaux sont déterminés expérimentalement. La comparaison avec les résultats expérimentaux permet d'évaluer l'adéquation des modèles existants et de proposer une ligne de base pour l'amélioration du modèle existant ou le développement d'un nouveau modèle de matériau.

# TABLE OF CONTENTS

<b>Abstract .....</b>	<b>3</b>
<b>Table of Contents .....</b>	<b>9</b>
<b>Lists of Tables .....</b>	<b>12</b>
<b>List of Figures .....</b>	<b>13</b>
<b>General Introduction .....</b>	<b>21</b>
<b>Chapter 1 State of the art .....</b>	<b>25</b>
<b>1.1 Introduction .....</b>	<b>25</b>
1.1.1 Material characterization of AA7075-T6.....	26
1.1.2 Material behaviour in manufacturing processes .....	31
<b>1.2 Constitutive material models for metal alloys .....</b>	<b>37</b>
1.2.1 Phenomenological models .....	37
1.2.2 Physical based models .....	40
<b>1.3 Shear testing of metallic alloys .....</b>	<b>47</b>
1.3.1 Simple shear test specimen .....	48
1.3.2 Torsion test specimen .....	52
<b>1.4 Intermediate Strain Rate Testing Devices.....</b>	<b>54</b>
1.4.1 Existing Intermediate Strain Rate Testing Devices .....	56
1.4.2 Load measuring technique .....	64
1.4.3 General Description of Intermediate Strain Rate Testing Device ....	66
1.4.4 Experimental Test at High-temperature.....	67
<b>1.5 Conclusion .....</b>	<b>69</b>
<b>Chapter 2 Design and validation of new torsion test bench .....</b>	<b>71</b>
<b>2.1 Introduction .....</b>	<b>71</b>

<b>2.2</b>	<b>Methodology.....</b>	<b>72</b>
2.2.1	Design criteria.....	72
2.2.2	Torsional loading mechanism.....	73
<b>2.3</b>	<b>Technical functions of a new torsion device.....</b>	<b>77</b>
2.3.1	Train the specimen in rotation (TF1).....	78
2.3.2	Measuring techniques (TF2).....	81
2.3.3	Test at high temperature (TF3).....	90
<b>2.4</b>	<b>Calibration of various components of the torsion device.....</b>	<b>94</b>
2.4.1	Calibration of strain gauges for torque measurement.....	94
2.4.2	Calibration of torque signal on the specimen and bar.....	95
2.4.3	Calibration of the emissivity for the heating device.....	98
<b>2.5</b>	<b>Preliminary tests (for validation of torsion device).....</b>	<b>99</b>
2.5.1	Experimental setup.....	99
2.5.2	Test results.....	101
<b>2.6</b>	<b>Conclusion.....</b>	<b>103</b>
<b>Chapter 3</b>	<b>Test results and outputs.....</b>	<b>104</b>
<b>3.1</b>	<b>Introduction.....</b>	<b>104</b>
<b>3.2</b>	<b>Test at room temperature.....</b>	<b>105</b>
3.2.1	Experimental Results.....	105
3.2.2	Shear strain distribution analysis.....	111
3.2.3	Comparison between short and long specimen.....	118
<b>3.3</b>	<b>Test at elevated temperature.....</b>	<b>120</b>
3.3.1	Design of experiments.....	121

3.3.2	Mechanical characterization of AA7075-T6 alloy .....	134
3.3.3	Microstructure characterization of AA7075-T6 alloy .....	136
<b>3.4</b>	<b>Conclusion .....</b>	<b>146</b>
<b>Chapter 4</b>	<b>Analyzing and modelling of the outputs .....</b>	<b>149</b>
<b>4.1</b>	<b>Introduction .....</b>	<b>149</b>
<b>4.2</b>	<b>Material modelling (thermomechanical behaviour).....</b>	<b>150</b>
4.2.1	Johnson-Cook (JC) model .....	150
4.2.2	Khan–Huang–Liang (KHL) model.....	152
4.2.3	Zerilli-Armstrong (ZA) model.....	154
<b>4.3</b>	<b>Results and discussion .....</b>	<b>156</b>
4.3.1	Experimental data .....	156
4.3.2	Derivation of JC model parameters for AA7075-T6.....	156
4.3.3	Derivation of KHL model parameters for AA7075-T6.....	160
4.3.4	Derivation of modified ZA model parameters for AA7075-T6.....	164
<b>4.4</b>	<b>Accuracy Analysis .....</b>	<b>170</b>
<b>4.5</b>	<b>Conclusion .....</b>	<b>174</b>
	<b>Conclusion and perspectives .....</b>	<b>176</b>
	<b>References.....</b>	<b>181</b>
	<b>Annex .....</b>	<b>200</b>
A1.	Design and dimensioning of the parts required for TF1 .....	200
A2.	Review of intermediate strain rate testing devices .....	206
A3.	New test bench development .....	206
A4.	New test procedure to perform simple shear test using compression/tensile apparatus at high temperature.....	207

## LISTS OF TABLES

Table 1.1:Typical strains, strain rates, and temperature ratio ( $T/T_m$ ) of some manufacturing processes [4]. ( $T$ =Temperature during the process, $T_m$ = melting temperature of the material). .....	25
Table 1.2:Chemical composition of AA7075 in weight % .....	27
Table 1.3:Mechanical properties exhibited by AA7075-T6.....	28
Table 1.4:Comparison of characteristics with typical wrought Aluminium .....	28
Table 1.5:Characterization of the machines based on the strain rate and type of loading. ..	55
Table 2.1:Material parameters used in the numerical simulations. ....	87
Table 2.2:The calibration table.....	95
Table 3.1:Results of dynamic torsion tests.....	111
Table 3.2:Doehlert matrix for two-variables .....	124
Table 3.3:Two-factor design of experiments.....	126
Table 3.4:Table of quantified responses obtained using DOE .....	133
Table 3.5:Chemical composition of Al-matrix and white intermetallic.....	138
Table 3.6:Grain size distribution .....	141
Table 4.1:Material constants obtained for the JC model.....	158
Table 4.2:Constants for KHL model .....	163
Table 4.3:The value of $S_1$ and $I_1$ for 15 strains. ....	166
Table 4.4:Material constants for modified ZA constitutive model. ....	168
Table 4.5: Correlation coefficient and average absolute relative error between experimental and predicted flow data for different formulated constitutive models. ....	171
Table 4.6:JC parameters based on Brar et al [51].....	173
Table 4.7: Modified ZA model parameters based on Ma et al.....	173

## LIST OF FIGURES

Figure 1.1:Application of Al alloys in commercial aircraft production .....	27
Figure 1.2:Schematic temperature profile of a T6 heat treatment.....	29
Figure 1.3:(a) Microstructure of as-received material in the direction perpendicular to the tensile (extrusion) direction. The average grain diameter is 70 $\mu$ m. (b) Microstructure of the as-received material in the direction parallel to the tensile direction near the centre of the rod. Black precipitates are coarse intermetallic[17]. .....	29
Figure 1.4: (a) TEM micrograph of AA7050-T6: Dark field (DF) showing the variation in grain size and nanometric precipitation at the grain boundaries and within the matrix, (b) TEM micrograph of AA7050-T6: Bright field (BF) showing fine distribution of precipitates and GP zones within the Al matrix, and (c) Crystal structure of MgZn <sub>2</sub> [18].....	30
Figure 1.5: Schematic representation of two studied manufacturing processes.....	31
Figure 1.6: (a)major shear zones during orthogonal cutting, (b) heat sources and heat flux during orthogonal cutting[23,24].....	32
Figure 1.7:Chip flow patterns evolving with cutting speeds [26]. .....	33
Figure 1.8:Schematic drawing of friction stir welding [29]. .....	34
Figure 1.9:Cross-section and detail of the different parts that constitute FSW joint of AA7075-T6 material [36].....	35
Figure 1.10:Schematic illustration of microstructure evolution during FSW for aluminium alloy[31] .....	36
Figure 1.11:Typical flow stress curve [37].....	45
Figure 1.12:Double-shear specimen [72] .....	49
Figure 1.13:Modified double-shear specimen and the clamping system [80].....	49
Figure 1.14: a) Split Hopkinson pressure bar b) stop ring c) Schematic diagram of the hat-shaped specimen, representation of the shear zone d) Hat shaped specimens[75].....	50



Figure 1.15: a) Eccentric notch shape shear specimen (dimensions in mm) b) Sample glued between Hopkinson bars before testing. c) Simulated and experimental data using the eccentric notch specimen d) DIC data Measured on the surface of the eccentric notch specimen[84]. ..... 51

Figure 1.16: Thin wall tubular specimen [88] ..... 52

Figure 1.17:Schematic diagram of a torsion split Hopkinson bar apparatus..... 53

Figure 1.18:a) Stress-Strain behavior of HY-100 steel in dynamic shear. b) Photographs of the grid lines showing deformation pattern at instants of the numbered arrows in (a) [90]. 53

Figure 1.19:Micro-voids and coalesced voids (cracks) seen in the wake of ASB in Ti-6Al-4V alloy. After [91]. ..... 54

Figure 1.20:Design zones for car body structures [2] A = Deformation zone at lower impact speed B = Deformation zone at higher impact speed C = Stiff and stable compartment [120]. ..... 57

Figure 1.21:a) Schematic diagram of the high-speed testing machine, b) Typical response of cement composite and comparison of the stress oscillation between the SDOF (single degree of freedom) model and the experiment at a nominal strain rate of  $22 \text{ s}^{-1}$ [121]. ..... 57

Figure 1.22:(a) modified hybrid machine and (b) stress–strain relation for aluminum obtained by the piezoelectric load sensor method (P1 and P2) and by the Hopkinson bar technique (B3 and B4) [124]. ..... 59

Figure 1.23:(a) overall view of Dropkinson bar test and (b) illustration of specimen displacement measurements [114]. ..... 60

Figure 1.24:Flywheel and its long pendulum system (load sensor) [115]. ..... 62

Figure 1.25:Schematic diagram of pendulum device before and after setting in position [115] ..... 62

Figure 1.26:Scheme of compression module on flywheel [134]. ..... 63

## List of Figures

Figure 1.27:Load signals measured by the two different load sensors under (a) $10 \text{ s}^{-1}$ ; (b) $100 \text{ s}^{-1}$ ; and (c) $200 \text{ s}^{-1}$ (DP780: An advanced high strength steel and 2024-T4an aluminium alloy) [136].	65
Figure 1.28:Configuration of split Hopkinson bar technique.	66
Figure 1.29:True stress-strain curves of 7075 aluminium alloy at different strain rates and temperatures (a) $0.01 \text{ s}^{-1}$ , (b) $0.1 \text{ s}^{-1}$ , (c) $1 \text{ s}^{-1}$ , (d) $10 \text{ s}^{-1}$ . [142].	68
Figure 2.1:Global view of the flywheel apparatus	72
Figure 2.2:General principle to transfer the rotational movement	74
Figure 2.3:Schematic representation of possible angular displacement of the anvil cylinder after impact	75
Figure 2.4:The position of contact point during the hammer-anvil impact a) at the beginning of loading b) during the loading c) after the loading	76
Figure 2.5:FAST diagram.	77
Figure 2.6:The anvil is pushed inside the cylindrical axle by a Pneumatic cylinder	78
Figure 2.7:The position of the anvil before (left) and after (right) engaged to the hammer	79
Figure 2.8:Square shape flanges a) Example of AA7075-T6 specimen b) clamping system with square slots to attach the specimen.	80
Figure 2.9:The cylindrical axle is connected to the clamping through coupling pin to avoid the catastrophic damage of the torsion setup.	80
Figure 2.10:Configuration of Hopkinson bar under torque	81
Figure 2.11:Strain gauges connected to the cylindrical bar in the Wheatstone bridge circuit	83
Figure 2.12: a) representation of grid pattern on the example specimen surface b) evolution of grid line when the specimen submitted to the torsion loading.	84
Figure 2.13:Final assembly of the torsion device	85
Figure 2.14:: The exploded view of torsion device	86

## List of Figures

Figure 2.15: The model assembly used for numerical simulations: (a) the assembly, (b) magnification of new specimen designed for the calibration. ....	87
Figure 2.16: FEM simulation to verify the integrity of the torsion device e.g. anvil and cylindrical axle .....	88
Figure 2.17: FEM simulation of the wave's propagation along TSHB setup .....	89
Figure 2.18: Induction heating system .....	91
Figure 2.19: Strain measuring technique for high temperature .....	93
Figure 2.20: Setup for calibration of Hopkinson torsion bar.....	94
Figure 2.21: The calibration curve between Voltage Vs Torque (Nm).....	95
Figure 2.22: Lagrange time-space diagram used for the representation of a torsional wave. a) Strain gauges attached to the surface of the specimen b) Strain gauges on the bar at the distance of x from the specimen. ....	96
Figure 2.23: Torque signals from the specimen and Hopkinson bar.....	97
Figure 2.24: Comparison between the experimental and simulation torque signals obtained on Hopkinson bar and specimen.....	97
Figure 2.25: Setup for emissivity calibration .....	98
Figure 2.26: Temperature effect on the emissivity of AA7075-T6.....	99
Figure 2.27: Experimental test apparatus (a) general view of the flywheel and torsion device (b) Hopkinson bar installed on the torsion device and (c) closer view of the torsion device with the camera setup, specimen. Flashlights and hammer-anvil mechanism .....	99
Figure 2.28: Tubular specimen geometry with square flanges used with a) Schematic representation b) original specimen with grid pattern deposited on the surface. ....	100
Figure 2.29: Typical raw data (wave signal) obtained from the torque sensor at loading speed of 6m/s .....	101
Figure 2.30: Shear strain versus time graph, photographic images shows the evolution of shear strain with respect to the time.....	102
Figure 3.1: Specimens with different lengths a) long specimen b) short specimen .....	105

## List of Figures

Figure 3.2: Torque vs time of AA7075-T6 alloy after before (a) and after (b) filtering the signals for different speed at room temperature for short and long specimens .....	106
Figure 3.3: Shear strain versus time graph of AA7075-T6. The slope of the linear fit line (dashed) corresponds to the average strain rate a) short and b) long specimen .....	107
Figure 3.4: Effect of gauge length on the strain rate .....	108
Figure 3.5: A specimen submitted to the torsion.....	108
Figure 3.6: Shear stress vs. shear strain experimental curves obtained from torsion device for the AA7075-T6 at different loading speed for a) short and b) long specimen. ....	110
Figure 3.7: Photographic evidence of shear strain localization behavior at the flywheel speed of 12m/s (650s <sup>-1</sup> ) average shear strain a) $\gamma=0$ , b) $\gamma=0.1$ , c) $\gamma=0.20$ , d) $\gamma=0.35$ , e) $\gamma=0.41$ (fracture occurred) .....	112
Figure 3.8: a) fractured specimen and b) shear localization and crack in the shear band ...	112
Figure 3.9: Temperature rise for AA7075-T6 at different strain rates .....	114
Figure 3.10: Bar plot for the shear band width vs strain rate .....	115
Figure 3.11: A typical shear stress-strain curve showing photographs of the grid patterns obtained at different shear strain at the flywheel speed of 12m/s (average strain rate 180s <sup>-1</sup> ). .....	116
Figure 3.12: Inhomogenous strain distribution along the length of the specimen at the strain rate of 180s <sup>-1</sup> .....	117
Figure 3.13: State of the specimen at different loading speed.....	117
Figure 3.14: Temperature rise for AA7075-T6 at different strain rates for long specimen	118
Figure 3.15: Shear stress vs strain curves of the specimen at different loading speed for short and long specimen. ....	119
Figure 3.16: Infinite length of the specimen under loading speed of a) 6m/s b) 12m/s....	120
Figure 3.17: Induction heating device setup on torsion test bench .....	121
Figure 3.18: Doehlert matrix in an experimental space with two factors X1 and X2.....	123

## List of Figures

Figure 3.19: Curve of Doehlert matrix for 2 variables $X_1$ and $X_2$ .....	125
Figure 3.20:Representation of the points of the experimental design (red), added test points (blue).....	126
Figure 3.21:Typical raw data obtained from the tests plotted between torque and time for of AA7075-T6 at (a,b) different temperatures with two different loading speed 6m/s and 10m/s respectively (c) different loading speed at constant temperature 300°C. ....	127
Figure 3.22: Torque vs time data after filtering at (a,b) different temperatures with two different loading speed 6m/s and 10m/s respectively (c) different loading speed at constant temperature 300°C.....	128
Figure 3.23:Torque level (Nm) as a function of loading speed and temperature a) contour 2D plot b) response surface (3D) .....	129
Figure 3.24: Surface response of maximum shear strain as a function of loading speed and temperature. ....	130
Figure 3.25:Surface response of maximum strain rate as a function of loading speed and temperature. ....	131
Figure 3.26:Surface response of maximum loading time as a function of loading speed and temperature. ....	132
Figure 3.27:State of the specimens after the high temperature tests .....	133
Figure 3.28:True stress vs true strain curves from hot torsion tests at different temperatures and strain rates .....	135
Figure 3.29:Graphical representation of a sample before and after test, its different surfaces prepared for microscopic analysis. ....	136
Figure 3.30:Initial microstructure of AA7075-T6 alloy a) longitudinal direction (LD) b) transverse direction (TD).....	137
Figure 3.31:(a) BES image of the AA7075 sample, and (b) Magnified BES image depicting the coarse bright and dark intermetallic in the microstructure .....	138

## List of Figures

Figure 3.32:Microstructure of AA7075-T6 samples from the cross-sectional view in Transverse direction after hot torsion tests at different temperatures and strain rates a) 200°C at 200s <sup>-1</sup> b) 300°C at 200s <sup>-1</sup> c) 400°C at 200s <sup>-1</sup> d) 200°C at 400s <sup>-1</sup> e) 300°C at 400s <sup>-1</sup> f) 400°C at 400s <sup>-1</sup> .	139
Figure 3.33: Image processing to measure the grain size a) original image b) image converted into pixel scale c) colored image	140
Figure 3.34: Microstructure behavior along the radial direction of the cut section on TD surface for strain rate of 400s <sup>-1</sup> at 400°C. a) bottom edge b) center c) top edge.	142
Figure 3.35:Microstructure of AA7075-T6 samples from the cross-sectional view in longitudinal direction (LD) after hot torsion tests at different temperatures and strain rates a) 200°C at 200s <sup>-1</sup> b) 300°C at 200s <sup>-1</sup> c) 400°C at 200s <sup>-1</sup> d) 200°C at 400s <sup>-1</sup> e) 300°C at 400s <sup>-1</sup> f) 400°C at 400s <sup>-1</sup> .	144
Figure 3.36:The shear response of alloy AA7075-T6 at different positions of the LD section given by the macro and micro images at strain rate of 400s <sup>-1</sup> and temperature of 400 °C shown in a,b,c.	145
Figure 4.1:True stress vs true strain curves from hot torsion tests at different temperatures and strain rates	156
Figure 4.2:Plot shows the relation between ln (σ – A) and ln (ε) under reference conditions. B and n values are determined.	157
Figure 4.3:Shows the regression line fits for different strain rate values which determines the constant C	157
Figure 4.4:Plot shows the regression line fitted to calculate the constant m at only 2 temperature values	158
Figure 4.5:Constitutive model (JC model) prediction comparison at different temperatures and strain rate of 200s <sup>-1</sup>	159
Figure 4.6:Constitutive model (JC model) prediction comparison at different temperatures and strain rate of 400s <sup>-1</sup>	159

## List of Figures

Figure 4.7:Plot shows the relation between $\ln(\sigma - A)$ and $\ln(\epsilon)$ under reference conditions. B and $n_0$ values are determined .....	161
Figure 4.8:Shows the regression line fits for two different strain rate values which determines the constant C .....	161
Figure 4.9: Plot show the relation between $\ln(1-\sigma K)$ vs $\ln(1-\sigma K)$ under reference condition and m value is determined.....	162
Figure 4.10:Constitutive model (KHL model) prediction comparison at different temperatures and strain rate of $200s^{-1}$ .....	163
Figure 4.11:Constitutive model (KHL model) prediction comparison at different temperatures and strain rate of $400s^{-1}$ .....	164
Figure 4.12:The relations between $\ln\sigma$ and $T^*$ for different strains.....	165
Figure 4.13:The relation between $\ln(\exp(1 - C1))$ and $\ln\epsilon$ . .....	166
Figure 4.14:The relation between S1 and $\epsilon$ . .....	167
Figure 4.15:Relationship between S2 and $T^*$ at different strains.....	168
Figure 4.16:Constitutive model (modified ZA model) prediction comparison at different temperatures and strain rate of $200s^{-1}$ .....	169
Figure 4.17:Constitutive model (modified ZA model) prediction comparison at different temperatures and strain rate of $400s^{-1}$ .....	169
Figure 4.18: Correlation coefficient between the experimental and predicted stress values for: (a) JC model; (b)KHL model; (c) ZA model.....	171
Figure 4.19:Absolute residual values from three models of (a) strain, (b) strain rate, and (c) temperature. ....	172
Figure 4.20: Constitutive model (a) JC model (b)modified ZA model predicted and from the literature (Brar et. al) at different temperatures and strain rate of $200s^{-1}$ .....	174

## **GENERAL INTRODUCTION**

The 4th industrial revolution is a technological revolution, bringing many innovations and creating a new market dynamic. Inside the factories, information technology, communicating sensors, Industrial Internet of Things (IIoT), software tools for simulation, information processing, process control, and most efficient machines make factories more and more agile, more efficient, more and more competitive. It is essential to fully understand the behaviour of a product, measure its performance and identify areas for improvement as soon as possible. Visualizing the behaviour of a product in its final environment makes possible to anticipate design pitfalls.

The growth of Industry 4.0 is now based on mature technologies. In terms of validation, designers benefit from realistic simulation software allowing them to address ever more varied and complex needs. The simulation integrated into the design has made possible to democratize and extend the calculation of finite elements within design offices. In terms of optimization, we can split the need into five major subjects in order to improve a product and to reduce its development cycle: design of reliable and safe products, numerical optimization, multi-scale simulation, modelling and simulation of processes, and virtual testing and qualification.

The common and essential element in these five themes is the material and more particularly the behaviour of this material in often-complex thermomechanical constraints. To obtain precise and reliable results from these different simulations, it is therefore necessary to characterize the material in a realistic manner by tests faithfully representing the thermomechanical constraints, which will be applied to it during its life: manufacturing processes, heat treatments, in service behaviour...

To achieve this objective, the characterization of the material is essential, since the effectiveness and service life of a structural component depends on its material properties and mechanical state under working conditions. These states of a material are influenced by its underlying microstructure that develops during manufacturing processes and post-processing treatments. The mechanical state of a material is usually predicted by numerical calculations based on models describing the behaviour of the material. However, these models generally cannot predict very accurately the kinetic changes that occur in the



microstructure during manufacturing processes. This results in an inaccuracy in the prediction of the mechanical state of the material, which can lead to the failure of the component in service. Therefore, it is very important to be able to predict their mechanical behaviour and these predictions are based on the initial mechanical properties of the parts, which are inherited from their manufacturing

The material experiences different loading conditions under different manufacturing processes including varied strain rates, strains, and temperatures. The manufacturing of metallic components often involves material deformation at medium to high strain rates and high temperatures, especially for the processes of forming, machining, friction stir welding (FSW), etc. Moreover, in a lot of manufacturing processes, the deformation within the material is generated by shear stress and not by tensile or compressive stresses. Hence, the understanding of the material behaviour under shear loading has great importance for a researcher to develop an accurate material model. The use of uniaxial tensile and compression tests to characterize the mechanical behaviour of materials is widespread, including at dynamic strain rates. The evaluation of the deformation and strength of components is based on material parameter. These parameters can be derived from tensile or compression test data in a simple way. In addition, most constitutive material models rely heavily on tensile testing. But, existing mechanical testing devices are not able to provide complete material behaviour history that occurred during the manufacturing process in the range of strain rate and temperature.

This thesis aims to study the material behaviour of the aerospace aluminium alloy AA7075-T6 under different strain rates and temperatures, with special focuses on the issues mentioned above. The first goal is to design and development of a new experimental test bench to perform the shear test at an intermediate strain rate. The new test bench will be equipped with load and strain measuring devices allow to study the accurate mechanical behaviour of the material. The second is to complement the new test bench with high temperature device in order to perform the thermomechanical test and be able to reproduce the same solicitations than during machining (medium strain rate and medium range deformation), FSW (medium strain rate, high deformation) processes, etc. At the same time to provide a detailed experimental behaviour of material and perform microstructural

investigations. Finally, the thermomechanical behaviour of AA7075-T6 under various strain rates and temperatures are compared both experimentally and by constitutive modelling.

Chapter 1 is based on the state of the art and consists of four parts: i) introducing the AA7075-T6 alloy most commonly used in the aerospace industry and the behaviour of the material in different manufacturing processes; ii) constitutive modelling of metal alloys: phenomenological and physical based models; iii) shear testing techniques: simple shear specimen and torsion specimen; iv) intermediate strain rate test devices: existing test device, basic technical assumptions, and high temperature testing.

In chapter 2, a new torsion test bench based on a flywheel mechanism is designed and validated. First, the design criteria and methodology for developing a test bench are discussed, including the technical details of each component. Next, accurate load and strain measurement techniques are developed to study the shear stress behaviour of the material, high temperature techniques are also discussed in detail and their calibrations. Finally, the preliminary experimental tests are performed to validate the test bench and the experimental results are analysed for AA7075-T6 alloy.

In chapter 3, the shear behavior of AA7075-T6 studied extensively based on test at room temperature and test at elevated temperature separately. First, at a room temperature test with different specimen lengths, different speeds, evolution of ASB, etc. was discussed in detail and the flow stress-strain results were compared. After that, induction heating device is coupled with torsion test bench to perform tests at elevated temperature. The design of experiments (DOE) is used to define the test parameters. Here, the temperature and flywheel speed as an input parameters and output parameters torque level, strain level, strain rate, time of loading, state of the specimen (broken / not broken), etc. are discussed in detail. Finally, thermomechanical flow stress behavior and microstructural characterization at different strain rate and temperature are studied.

In chapter 4, we compared the experimental results obtained from new torsion test bench at different strain rate and at different temperature to the prediction of classic existing material models commonly used for constitutive behavior modelling of AA7075-T6. The most widely used models today, for industrial applications (manufacturing process) are the Johnson-Cook (JC), Khan-Huang-Liang (KHL), Zerilli-Armstrong (ZA) models, etc. The

parameters are experimentally determined in tests performed over a different strain rates and temperatures. By comparison with the experimental results, the suitability of the three models is evaluated by calculating the correlation coefficient and average absolute relative error.

Finally, the main conclusions are summarized in the last part of the manuscript: the original scientific contribution is highlighted and some perspectives for future work are proposed.

# CHAPTER 1 STATE OF THE ART

## 1.1 Introduction

The effectiveness and service life of a structural component depends on its material properties and mechanical state under working conditions. These states of a material are influenced by its underlying microstructure that develops during manufacturing processes and post-processing treatments. The mechanical state of a material is usually predicted by numerical calculations based on models describing the behaviour of the material. However, these models generally cannot predict very accurately the kinetic changes that occur in the microstructure during manufacturing processes. This results in an inaccuracy in the prediction of the mechanical state of the material, which can lead to the failure of the component in service. Therefore, it is very important to be able to predict their mechanical behaviour [1] and these predictions are based on the initial mechanical properties of the parts, which are inherited from their manufacturing.

The material experiences different loading conditions under different manufacturing processes including varied strain rates and temperatures. The manufacturing of metallic components often involves material deformation at medium to high strain rates and high temperatures, especially for the processes of forming, machining, friction stir welding (FSW) [1–3], etc. An overview of typical strains, strain rates, and temperatures found in manufacturing processes is given in Table 1.

**Table 1.1:** Typical strains, strain rates, and temperature ratio ( $T/T_m$ ) of some manufacturing processes [4]. ( $T$ =Temperature during the process,  $T_m$ = melting temperature of the material).

Manufacturing process	Strain	Strain rate ( $s^{-1}$ )	$T/T_m$
Extrusion	2 to 5	$10^{-1}$ to $10^2$	0.16-0.7
Metal Forging	0.1 to 0.5	$10^0$ to $10^3$	0.16-0.7
Machining	1 to 10	$10^3$ to $10^6$	0.16-0.9
Sheet metal forming	0.1 to 0.5	$10^0$ to $10^2$	0.16-0.7
Friction Stir Welding (FSW)	0.1 to 5	$<10^3$	0.16-0.9

The research has found that the deformation of metals and alloy during manufacturing processes can reach the strain rate ranging from  $10^{-1}$ - $10^6\text{s}^{-1}$  and the temperature of higher than  $0.6 \cdot T_m$  ( $T_m$ = melting temperature). Hence the research on the flow behaviour of material at low to high strain rates and elevated temperatures is vital important to understand the material dynamic properties during manufacturing processes. Hence, the predictability of any material model largely depends on the accuracy of the material parameters obtained for the constitutive model from experimental tests [5]. However, existing mechanical testing devices are not able to provide complete material behaviour history that occurred during manufacturing process in the range of strain rate and temperature. In addition, in manufacturing processes, the deformation within the material is generated by shear stress and not by tensile or compressive stresses. Hence, the understanding of the material behaviour under shear loading has great importance for a researcher to develop an accurate material model.

The state of the art consists of four parts: introducing the AA7075-T6 alloy most commonly used in the aerospace industry and the behaviour of the material in different manufacturing processes; constitutive modelling of metal alloys: phenomenological and physical based models; shear testing techniques: simple shear specimen and torsion specimen; intermediate strain rate test devices: existing test device, basic technical assumptions, and high temperature testing.

### **1.1.1 Material characterization of AA7075-T6**

Aluminium alloys (AA) have been the main component in the structural parts of the modern-day aircrafts due to their unique performance characteristics, fabrication costs, design experience, and manufacturing methods and facilities. They are more commonly used in fuselage, wings and supporting structures of commercial airplanes, military cargo and transport [6]. 7xxx series AA alloys find applications in the aerospace industry because of their high strength to weight ratio along with a combination of properties such as high fracture toughness and resistance to fatigue and fatigue crack growth. Furthermore, their relatively lower cost and heat treatability grant extra advantages over other Aluminium alloys. Figure 1.1 highlights the application of different AA7xxx series alloys in various parts of a commercial aircraft [7]. These alloys are mainly selected in the fabrication of upper wing skins, stringers and horizontal/vertical stabilisers [8].

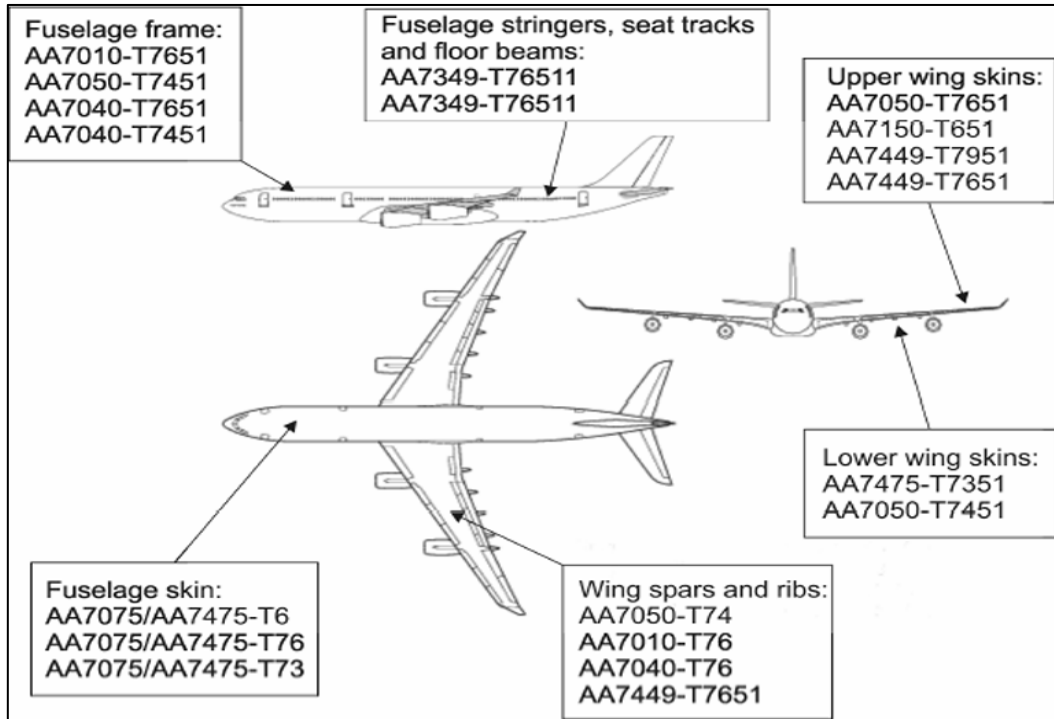


**Figure 1.1:**Application of Al alloys in commercial aircraft production

- **AA7075-T6: Composition, properties and applications**

AA7075 alloy belongs to the Al-Zn-Mg-Cu series with Zn constituting the highest of 5-6 % of the total weight. Table 1.2 shows the typical alloy composition of the material [9].

**Table 1.2:**Chemical composition of AA7075 in weight %

Element	Zn	Mg	Cu	Cr	Fe	Mn	Si	Ti	Al
Wt. %	5.6-6.1	2.1-2.5	1.2-1.6	0.18-0.28	Max 0.5	Max 0.3	Max.0.4	Max.0.2	bal

On account of the high mechanical strength, light weight, dimensional stability, machinability, good vibration-damping characteristics and stiffness in its T6 tempered condition [10], AA7075 is widely used in the structural applications in aerospace, military and automobile industries, such as in aircraft fittings, fuse parts, shafts and gears, missile parts, regulating valves, worm gears, sensor and guidance components for flight and satellite systems, etc. [9]. The typical mechanical properties exhibited by AA7075-T6 material are listed in Table 1.3. [9,11].

**Table 1.3:**Mechanical properties exhibited by AA7075-T6

Youngs Modulus (MPa)	70000
Poisson's Ratio	0.3
Tensile Strength, Ultimate (MPa)	572
Tensile Strength, Yield (MPa)	503
Shear strength (MPa)	331
Shear modulus (MPa)	26900
Melting Temp (°C)	520-635
Density (kg/mm3)	2.70E-06
Heat Capacity J/K/kg	960
Heat Conductivity, λ (W/m/K)	130
Taylor Quinney coefficient (β)	0.9

A comparative analysis of the strength, corrosion resistance, weldability and toughness of different Al alloys have been shown in Table 1.4 [12].

**Table 1.4:**Comparison of characteristics with typical wrought Aluminium

	By alloy and quality	Yield strength (MPa)					Corrosion resistance		Weld ability	Tough ness
		100	200	300	400	500	General corrosion	Stress corrosion		
Non-heat-treated alloy	1100-H14	100					A	A	A	—
	3003-H14	150					A	A	A	—
	3004-H34	180					A	A	B	—
	5005-H14	150					A	A	A	—
	5052-H34	215					A	A	A	—
	5083-H321	230					A	B	A	—
Heat-treated alloy	2017-T3	280					C	C	B	C
	2024-T3	350					C	C	B	B
	2024C-T3	310					A	C	B	B
	2219-Tx1	360					C	B	A	B
	0061-T6	270					B	A	A	C
	7050-T7451	473					C	B	C	A
	7075-T6	510					C	B	C	B
	7475-T6	480					C	B	C	A

AA7075-T6 exhibits the best combination of strength and fracture toughness compared to other Al alloys.

- **T6 heat treatment process**

Normally the heat treatment process for T6 temper of extruded AA7075 consists of the following two steps [9,11,13–16] shown in Figure 1.2:

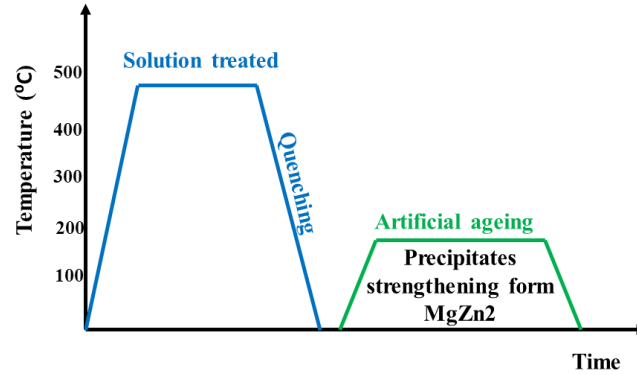


**Figure 1.2:** Schematic temperature profile of a T6 heat treatment.

**Solution heat treatment (SHT):** The material is heated up and held at a high temperature (around 460-480° C) for a suitable period of time causing the dissolution of the second phases in the Al matrix to form a single-phase alloy. After that when the material is quenched rapidly to the room temperature, it results in a supersaturated solid solution.

**Age-hardening:** Then the SHT material is aged at a temperature of around 110-120° C for a suitable period (minimum of 24 hours). During the ageing process, finely dispersed MgZn<sub>2</sub> precipitates are formed in the matrix which strengthens the material.

- **Microstructure of AA7075-T6**

For example, the grain size of the as-received AA7075-T6 alloy from the extruded round bar was characterized in directions both perpendicular and parallel to the bar axis [17]. The grains are elongated and have coarse inclusions. Figure 1.3 (a) shows microstructure perpendicular to the rod axis. The average grain diameter is  $85.5 \pm 13.4 \mu\text{m}$ . In the direction parallel to the rod axis, Figure. 1.3 (b) reveals elongated grains with lengths that increase as the distance from the centre of the rod increases from  $574 \pm 58$  to  $976 \pm 169 \mu\text{m}$ .

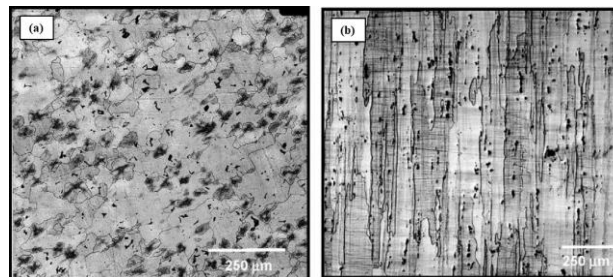


**Figure 1.3:** (a) Microstructure of as-received material in the direction perpendicular to the tensile (extrusion) direction. The average grain diameter is  $70 \mu\text{m}$ . (b) Microstructure of the as-received material in the direction parallel to the tensile direction near the centre of the rod. Black precipitates are coarse intermetallic [17].



AA7075-T6 is precipitation strengthened due to the T6 heat treatment process. During the age-hardening process, the usual sequence of the precipitation formation is given by [18]: Super saturated solid solution (SSSS), also known as a phase => Guinier-Preston (GP) zone => Metastable  $\text{MgZn}_2$  ( $\eta'$ ) phase => Stable  $\text{MgZn}_2$  ( $\eta$ ) phase. The GP zones are coherent fine clusters of solute atoms having a similar crystal structure as of the matrix.

The  $\eta'$  phase is the main strengthening factor of AA7075-T6 due to its existence in abundance and strong pinning effect on dislocations. This phase is formed within the grains and has a hexagonal crystal structure ( $a = 0.496 \text{ nm}$ ,  $c = 1.40 \text{ nm}$ ) with a plate like shape Figure 1.4 (a) and (b) [18]. It is a metastable phase and starts to coarsen and dissolve above  $210^\circ \text{C}$  and transforms into stable  $\eta$  phase at  $240^\circ \text{C}$  [19]. The equilibrium phase,  $\eta$ , is a much coarser, needle and laths shaped phase which is formed along the grain boundaries Figure 1.4 (a). This is less coherent with Al matrix as compared to  $\eta'$  phase and can be observed by Electron Back-Scattered Diffraction (EBSD). The hexagonal structure of  $\text{MgZn}_2$  Figure 1.4 (c) belonging to  $P6_3/mmc$  (194) space group with C14 structure type, hP12 Pearson sign [20] and lattice parameter of  $a = 0.5221 \text{ nm}$  and  $c = 0.8567 \text{ nm}$  [21],  $\eta$  phase starts to dissolve in the matrix above a temperature of  $300^\circ \text{C}$ .

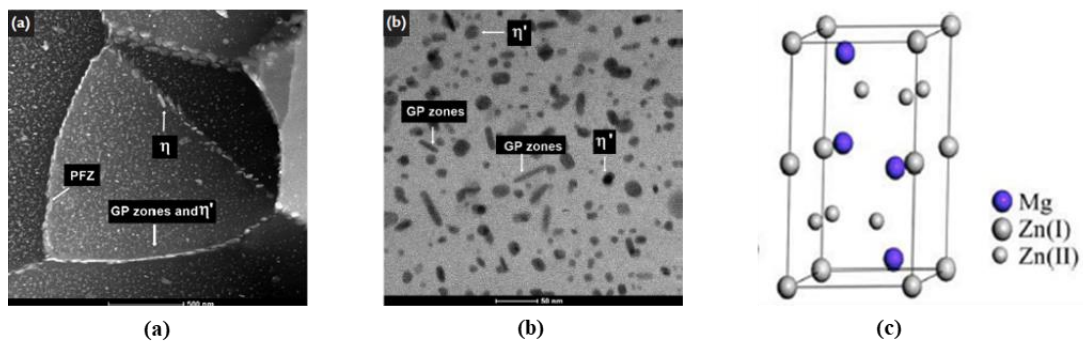


**Figure 1.4:** (a) TEM micrograph of AA7050-T6: Dark field (DF) showing the variation in grain size and nanometric precipitation at the grain boundaries and within the matrix, (b) TEM micrograph of AA7050-T6: Bright field (BF) showing fine distribution of precipitates and GP zones within the Al matrix, and (c) Crystal structure of  $\text{MgZn}_2$ [18]

AA7075-T6 material has also been reported to contain two types of irregular shaped intermetallic particles or inclusions [17]. The first one is a Fe-based intermetallic which also contains Al and Cu and appears brighter than the Al matrix. This type of inclusions typically takes up the form of  $\text{Al}_{23}\text{CuFe}_4$ ,  $\text{Al}_7\text{Cu}_2\text{Fe}$ , etc.[22]. The second type of intermetallic contains

Si and Mg as primary elements along with small amount of O and Al and appears darker than the Al matrix. A typical example of this type of inclusions is  $Mg_2Si$ . These intermetallic particles can be formed during the manufacturing process. They play an important role in the deformation behaviour of the material.

### 1.1.2 Material behaviour in manufacturing processes

The result of material behaviour during a manufacturing process depends on the thermomechanical phenomena determined by the processing parameters. These phenomena result from the tool-workpiece interaction and determine the characteristics in the final part (i.e., microstructure, mechanical properties, surface quality, etc.). Hence, it is essential to understand the impact of manufacturing processes on the final parts from a modelling point of view to develop reliable models to simulate and predict final desirable microstructures. Here we focus on the impact of two different processes (i.e., Machining and FSW). Figure 1.5 shows the microstructure evolution in two different manufacturing processes.

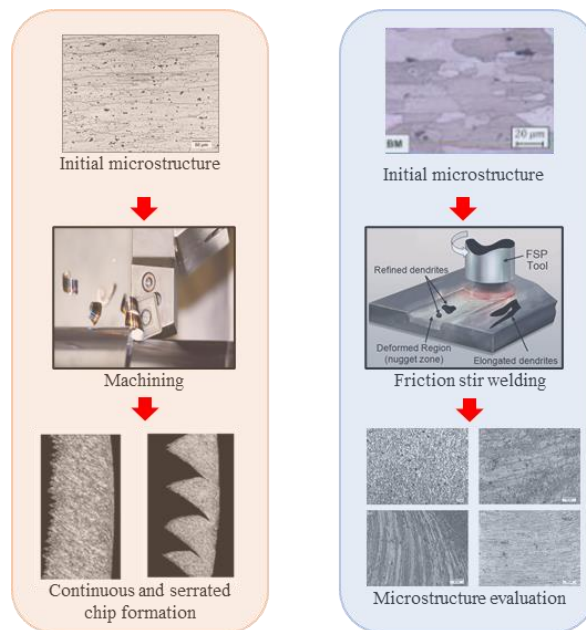


**Figure 1.5:** Schematic representation of two studied manufacturing processes

- **Machining processes**

Machining processes are frequently used in manufacturing industries. Metallic alloys including the aeronautical aluminium alloys and the Hard-to-Cut materials such as titanium and nickel-based alloys were one of the most used materials in the last years by aeronautic, spatial and automotive industries. Comparing to some metal forming processes, the

machining process induces high thermomechanical load. The impact of the machining process on the material microstructure changes, are usually influenced by different cutting conditions used in orthogonal cutting. Figure 1.6 (a) and (b) gives the major shear zones and the heat sources during orthogonal cutting.

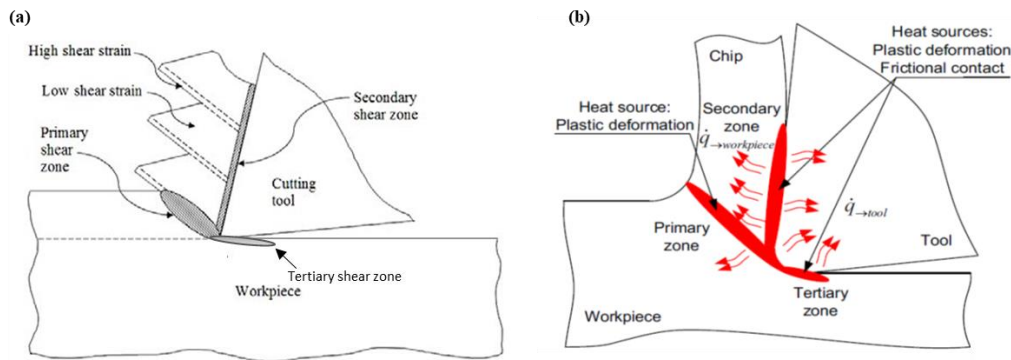


**Figure 1.6:** (a) major shear zones during orthogonal cutting, (b) heat sources and heat flux during orthogonal cutting[23,24].

The mechanisms of chip formation can be described through the amount of the thermomechanical load occurred within the shear zones:

- **The Primary Shear Zone (PSZ):** is subjected to shear. At this zone, the direction of the material flow changes under high strain ( $>0.8$ ) and high strain rate ( $> 10^2 \text{s}^{-1}$ ). The plastic deformation in this zone is the result of temperature rise. Both deformation and temperature rise induce microstructure change of the material in this zone. Shear zone in machine process is also called as adiabatic shear bands as there is no loss of heat during formation of shear localization.
- **The Secondary Shear Zone (SSZ)** is located at the tool-chip interface. This zone is subjected to intense friction which leads to plastic deformation of the material. The temperature rises in this zone.
- **The Tertiary Shear Zone (TSZ)** is located at the contact between the tool clearance face and the subsurface of the workpiece. The material flow speed at this zone is similar to the cutting speed. The surface integrity of the machined workpiece depends from the thermomechanical load at this zone. An elastic spring back of the material occurs after the tool has passed through. Determining the thermomechanical load in

this zone and its impact on the material microstructure help to improve the quality of the machined surface.

The cutting process induces change in grain orientation, grain size, phases, etc. This change in the material microstructure is the result of a certain level of thermomechanical load occurred within the major shear zones as given in Figure 1.6.

### Chip morphology

In general, chip morphologies obtained during material removal can be divided into three categories: Continuous chips which its profile properties remain approximately constant, the segmented or the serrated chips, the discontinuous chip which is obtained when the chip segmentation increase to the point where each segment breaks [25]. The cutting velocity has also a significant role on the onset of segmented chips. For the Hard-to-cut materials such as for Ti-6Al-4V and Inconel 718, segmented chips were found to be generated at low cutting velocities [26]. The Figure 1.7 shows the evolution of the chip morphologies according to different cutting velocities and for different materials.

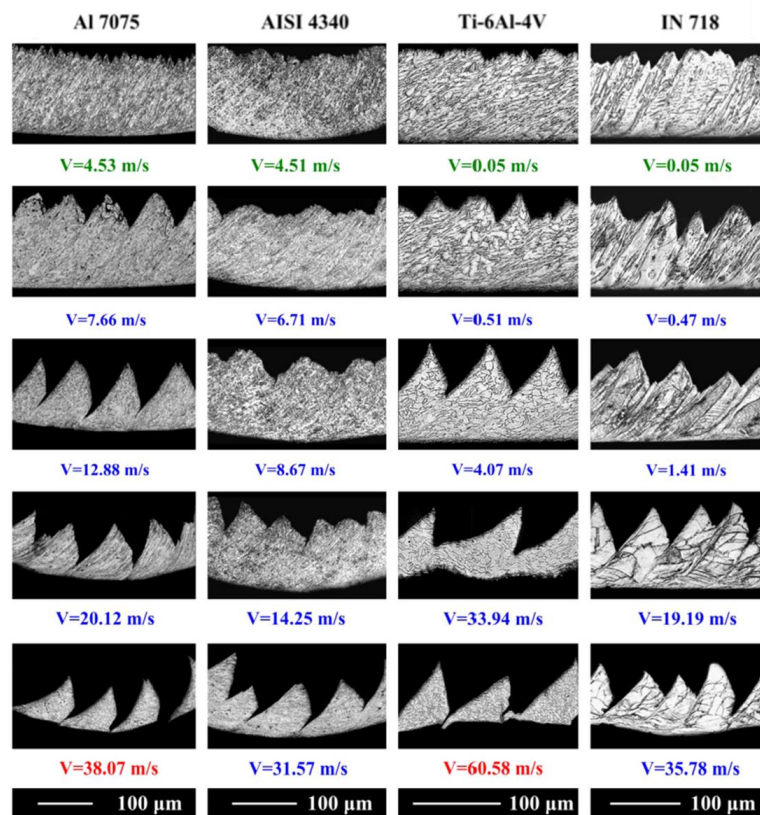
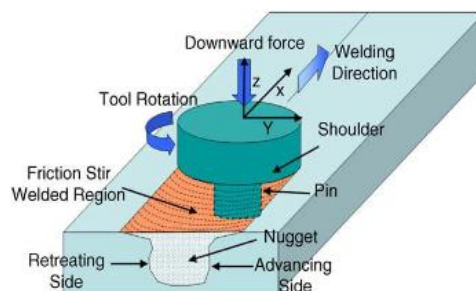


Figure 1.7: Chip flow patterns evolving with cutting speeds [26].

For example, in the chip of aluminium alloy studied by [17], the obtained morphology of chip can be traced back to the adiabatic shear band. It was characterized by a thin layer experienced a high local shear strain during the processes. For the aeronautic aluminium alloy, segmented chips were obtained at higher cutting speeds for the AA7075 in [26] and the A2024-T351 in [27]. On the other hand, researches on critical cutting speed for the onset of segmented chips were made by [26]. The orthogonal cutting tests were carried out on cylindrical tubes. Cutting speeds are between 3 m/s and 12m/s. The microstructure of Chip observations of AA7075 alloy showed a microstructural change: the size of the precipitates increased and recrystallized equiaxed grains were observed within the shear band. It means that the shear strains and shear strain rates present during machining were responsible for the formation of recrystallized grains within the shear bands

- **Friction stir welding (FSW)**

Friction stir welding is a solid-state joining process invented by TWI in 1991 [28]. This process involves a non-consumable cylindrical tool rotating at very high speed and plunging into adjacent edges of the alloy's pieces, thereby joining them. The basic principle of FSW is shown in Figure 1.8.



**Figure 1.8:** Schematic drawing of friction stir welding [29].

The two parts to be welded are brought together, positioned on the support plate and clamped. When the rotating cylindrical tool is inserted into the workpieces, frictional heating occurs, which brings both parts into the plasticized state. Due to the translation of the tool along the joint line, the material is stirred and forged behind the backside of the pin, where it consolidates and cools to form the solid-state weld.

In FSW, severe thermomechanical conditions are achieved due to the tool-workpiece interaction. As the tool moves, it generates heat due to friction and plastic deformation of the workpiece, which increases the temperature considerably. The maximum values reached

depend on the working conditions but never reach the melting temperature. At the same time, the workpiece is deformed at specific strain rates ( $1-10^3 \text{ s}^{-1}$ ) generating a fully modified microstructure at the end. The microstructure of the weld is significantly altered due to the high plastic deformation and the evaluation depends on the processing parameter chosen during welding.

- **Microstructure:**

Frictional heat causes the alloys to soften and allows the tool to transverse along joint line. As described by numerous authors, the welded joint from aluminium alloy is composed of four distinct zones [30–35]. The nugget zone (NZ), the thermomechanical-affected zone (TMAZ), the heat affected zone (HAZ) and the base material (BM). In Figure 1.9, the typical FSW cross-section is displayed for AA7075-T6.

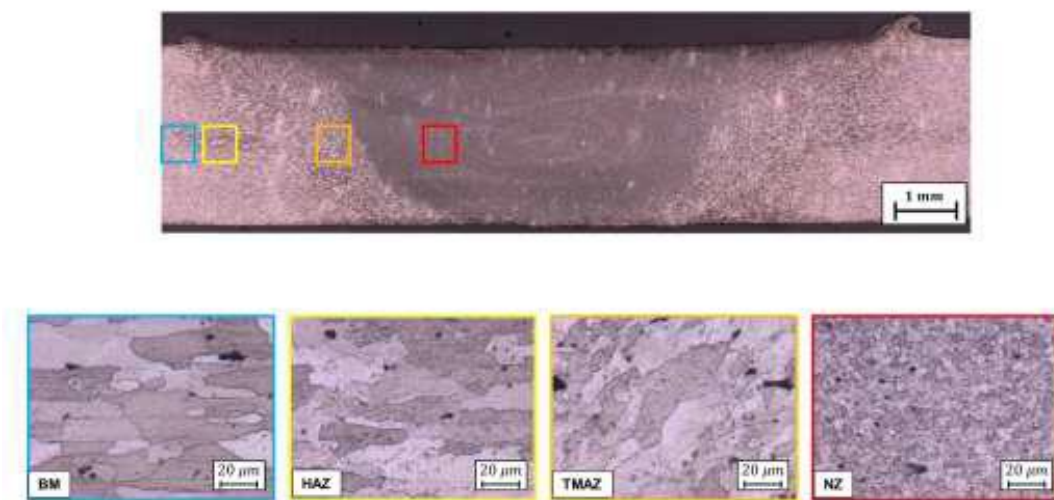


**Figure 1.9:** Cross-section and detail of the different parts that constitute FSW joint of AA7075-T6 material [36].

NZ is a region of heavily deformed material that corresponds to the location of the pin during welding. The grain within NZ are generally equiaxed and an order of magnitude smaller than the grains within BM. In the TMAZ region, which occurs on either side of the NZ, the strain and the temperature are lower than in NZ, the microstructure in TMAZ is similar to that of BM, although it is significantly deformed and rotated. The HAZ is common to all welding processes subjected to a thermal cycle, but it is not deformed during welding. The temperatures in HAZ are lower than those in the TMAZ. But they may still have a significant effect on the microstructure. The BM is unaffected by welding process.

The FSW weld joint centre (NZ) is the most complex part, where the most severe conditions both mechanically and thermally develop. This zone is distinguished from the others by a microstructure completely different from that of the starting base material, confirming how the severe process conditions involve substantial changes in the microstructure. Various subsequent phases that lead to the nugget zone are displayed in Figure 1.10. The ultimate result of these mechanisms is certain grain size and dislocation densities. In this region, the material interacting with the tool is severely heated at a temperature close or above the solidus temperature and deformed at medium-high strain rate.

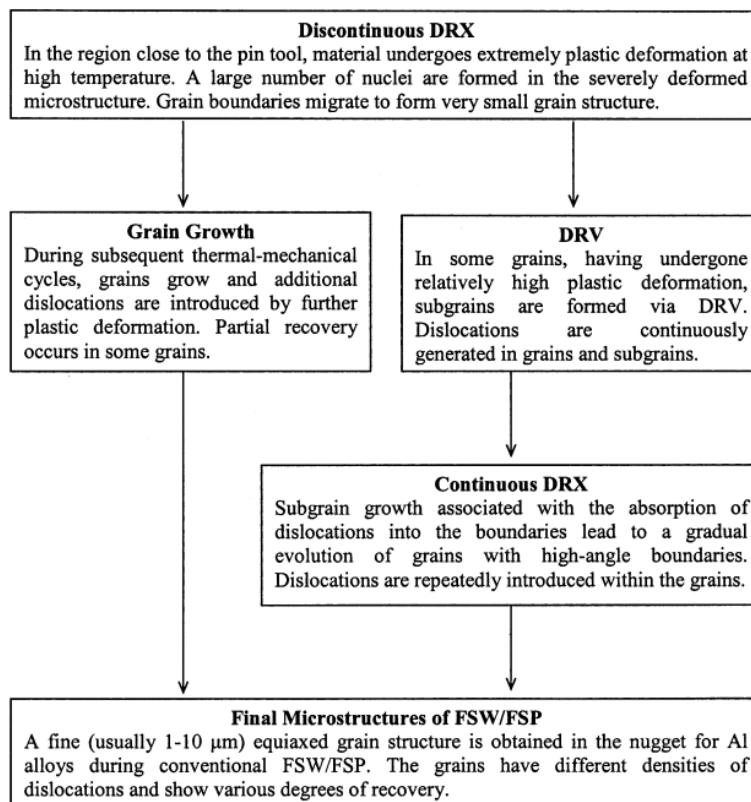


**Figure 1.10:** Schematic illustration of microstructure evolution during FSW for aluminium alloy [31]

The severe thermo-mechanical conditions start the dynamic recrystallization (DRX) process with a completely new grain shape and size compared to the BM. It means that the shear strains, strain rates and temperature induce during the FSW process were responsible for the formation of recrystallized grains and change in the microstructure of the workpiece. Hence to incorporate this kind of behaviour in the material modelling is very important for the designer to study FSW process during finite element simulation (FEM) simulation to optimize the accurate processing parameters.

## 1.2 Constitutive material models for metal alloys

Constitutive material models are often used to describe the plastic flow behaviour of metal alloys in a form that can be used in computer code to model the response of mechanical parts under loading conditions applied during manufacturing processes. They are essential for obtaining accurate results in finite element simulation. However, it should be emphasized that material constitutive models are mathematical descriptions of physical phenomena and therefore follow the different modelling approaches. Material constitutive models are generally divided into two categories:

- Phenomenological models: They provide a description of the flow stress based on empirical observations and usually consist of a mathematical function [37]. It is straightforward and have a finite number of material parameters. However, they are usually used under constrained deformation conditions (e.g., a limited range of strain rates, temperatures, and strains). These models are solely based on observed characteristics from stress-strain data without any underlying physical interpretations and theoretical basis.
- Physical based models: Physical based material models use a knowledge about the underlying physical process (dislocation & microstructure evolution), to formulate the constitutive equations. Compared to phenomenological models, they can give an accurate deformation behaviour description over a wide range of deformation conditions. Developing a true physical-based model requires more experiments tests to define material constants.

### 1.2.1 Phenomenological models

Phenomenological models, including Johnson–Cook (JC) model [38], Khan–Huang (KH) model [39], Khan–Huang–Liang (KHL) model [40–42], Khan–Liang–Farrokh (KLF) model [43], Fields–Backofen (FB) model [44], Molinari–Ravichandran (MR) model [45], Voce–Kocks (VK) model [46], Arrhenius equation [47,48], and some other phenomenological models [49]. The common features are that they can be expressed as the functions of the temperature, strain-rate and strain to consider the effects of these parameters on the flow behavior of metal alloy.

$$\sigma = \sigma(\varepsilon, \dot{\varepsilon}, T) \quad (1.1)$$



A phenomenological model is actually the classical approach for modelling the material behavior. Some of these models are explained below.

- **Johnson-Cook (J-C) model**

The Johnson-Cook (J-C) model is commonly used for many types of materials over a wide range of strain rates and temperatures. It is expressed as follows:

$$\sigma = \underbrace{(A + B\varepsilon^n)}_{\substack{\text{Hardening effect} \\ \text{(Power law)}}} \underbrace{\left(1 + C \ln\left(\frac{\dot{\varepsilon}}{\dot{\varepsilon}_0}\right)\right)}_{\text{Strain rate effect}} \underbrace{\left(1 - \left(\frac{T - T_0}{T_m - T_0}\right)^m\right)}_{\text{Temperature effect}} \quad (1.2)$$

where  $\sigma$  is the flow stress,  $\varepsilon$  is the equivalent plastic strain,  $A$  is the yield stress at reference strain rate ( $\dot{\varepsilon}_0$ ) and temperature ( $T_0$ ),  $B$  is the strain hardening coefficient,  $n$  is the strain hardening exponent,  $\frac{\dot{\varepsilon}}{\dot{\varepsilon}_0}$  is the dimensionless strain rate and  $\frac{T - T_0}{T_m - T_0}$  is the homologous temperature.  $T$  is the working temperature,  $T_m$  is the melting temperature and  $T_0$  is the room temperature. The three items in the equation describe the strain hardening effect, strain rate sensitivity and thermal softening effect due to temperature effect, respectively. In addition, the three effects are assumed to be independent of each other. The J-C model is used extensively because it is simple to implement and the parameters are easy to obtain with a limited number of tests. However, it considers the mechanical properties of materials as a simple multiplication of strain, strain rate and temperature and ignores the coupling effects between these elements. Therefore, some researchers made modifications to the original J-C model [50–52]

Wang et al. [53] proposed a modified JC's model for high strain rates and temperatures representative of those encountered during machining. They found that the strain rate softening parameter  $C$  is dependent on strain rate and temperature. Similarly, Chen et al. [54] proposed a modified JC's constitutive equation, where both the work hardening, and thermal softening terms are dependent on strain rate and temperature. Calamaz et al. [55] developed a material model based on modified JC's constitutive equation, in order to simulate segmented chip formation, without the need for material damage model. This model was used in several research work dealing with FEM simulation of machining of several materials from low to high strength of material such as titanium, aluminium, nickel-based alloys.

- **Khan-Huang (KH) model and Khan-Huang-Liang (KHL) model**

Khan and Huang [39] proposed a constitutive visco-plastic model (KH model) in 1992 to simulate the behaviour of coarse-grained aluminium alloys over a wide range of strain rates. They proposed the following constitutive equation:

$$\sigma = g_1(\varepsilon)g_2(\dot{\varepsilon}) \quad (1.3)$$

$$g_1(\varepsilon) = \sigma_0 + E_\infty \varepsilon - a e^{-\alpha \varepsilon} \quad (1.4)$$

$$g_2(\varepsilon)g_2(\dot{\varepsilon}) = \left[ 1 - \frac{\ln(\dot{\varepsilon})}{\ln(D_{max}^p)} \right]^n \quad (1.5)$$

where  $g_1(\varepsilon)$  characterizes the flow stress versus strain at reference strain rate, and  $g_2(\dot{\varepsilon})$  describes the strain rate hardening effect.  $\sigma$ ,  $\varepsilon$ ,  $\dot{\varepsilon}$  and  $D_{max}^p$  are the flow stress, the equivalent plastic strain, the strain rate and the maximum strain rate the material experienced during the testing process, respectively.  $n$ ,  $E_\infty$ ,  $\sigma_0$ ,  $a$  and  $\alpha$  are material constants that need to be determined.

It is evident that the KH model does not take into account the effect of temperature. In order to better predict the work hardening behaviour of materials, Khan, Huang and Liang added the thermal effect of coupling strain and strain rate to the original KH model and developed the Khan-Huang-Liang (KHL) model [40] :

$$\sigma = \left[ A + B \left( 1 - \frac{\ln(\dot{\varepsilon})}{\ln(D_{max}^p)} \right) \varepsilon^k \right] \left( 1 - \left( \frac{T - T_0}{T_m - T_0} \right)^m \right) e^{c \ln \dot{\varepsilon}} \quad (1.6)$$

where  $A$ ,  $B$ ,  $n$ ,  $k$ ,  $c$ , and  $m$  are material constants;  $\frac{T-T_0}{T_m-T_0}$  is the homologous temperature,  $T$  is the testing temperature,  $T_m$  is the melting temperature and  $T_0$  is the reference temperature. From the equation, it is obvious that the coupling effect between strain and strain rate on strain hardening behavior of materials is included in the model.

- **Arrhenius equation**

Arrhenius equation is widely used to describe flow stress's dependence on strain rate at elevated temperatures [47]. The effects of strain rate and temperature on the deformation behavior of materials can be described by the Zener-Hollomon parameter in an exponent-type equation [47,48].

$$\dot{\varepsilon} = AF(\sigma)\exp\left(-\frac{Q}{RT}\right) \quad (1.7)$$

$$z = \dot{\varepsilon}\exp\left(\frac{QR}{T}\right) \quad (1.8)$$

$$F(\sigma) = [\sinh(\alpha\sigma)]^n \quad (1.9)$$

where  $\dot{\varepsilon}$  is the strain rate,  $R$  is the universal gas constant,  $T$  is the absolute temperature,  $Q$  is the activation energy for deformation behaviors,  $\sigma$  is the flow stress,  $A$ ,  $\alpha$  and  $n$  are material constants. According to the three equations above, the flow stress can be written as,

$$\sigma = \frac{1}{\alpha} \ln \left[ \frac{z}{A} + \sqrt{\left(\frac{z}{A}\right)^2 + 1} \right] \quad (1.10)$$

It is clear that the effect of strain on the deformation behaviors of materials is not included in the Arrhenius equation. Therefore, Lin et al. [49] modified the model by considering strain rate and strain, then used it to describe flow stress of 42CrMo steel over a wide range of strain rates and temperatures. They expressed  $Q$ ,  $n$ ,  $A$  and  $\alpha$  as polynomial functions of strain:

$$Q = B_0 + B_1\varepsilon + B_2\varepsilon^2 + B_3\varepsilon^3 + B_4\varepsilon^4 + B_5\varepsilon^5 \quad (1.11)$$

$$n = C_0 + C_1\varepsilon + C_2\varepsilon^2 + C_3\varepsilon^3 + C_4\varepsilon^4 + C_5\varepsilon^5 \quad (1.12)$$

$$A = \exp(D_0 + D_1\varepsilon + D_2\varepsilon^2 + D_3\varepsilon^3 + D_4\varepsilon^4 + D_5\varepsilon^5) \quad (1.13)$$

$$\alpha = E_0 + E_1\varepsilon + E_2\varepsilon^2 + E_3\varepsilon^3 + E_4\varepsilon^4 + E_5\varepsilon^5 \quad (1.14)$$

### 1.2.2 Physical based models

An obvious drawback of phenomenological models is that they are obtained by fitting experimental data and do not include any deformation mechanism. It may work well under common conditions, but under extreme conditions (such as extremely high strain rates and temperatures), they are no longer able to give an accurate description. Therefore, physical models based on deformation mechanisms such as dislocation mechanics and thermal activation seem to be more reliable. So far, many physical models such as the Zerilli-Armstrong (Z-A) model [56], the Bonder-Partom (B-P) model [57], the Rusinek-Klepaczko (R-K) model [58], the Mechanical Threshold Stress model (MTS) [59,60] and the model considering dynamic recovery and dynamic recrystallization [61] have been developed.

- **Zerilli-Armstrong (Z-A) model**

Zerilli-Armstrong (Z-A) model is developed based on dislocation mechanism and often gives a good description of deformation behaviour under different loading conditions. It considers the effects of strain hardening, strain rate hardening and thermal softening on deformation behaviour of materials, and is made up of two parts, thermal component and athermal component,

$$\sigma = \sigma_{\alpha} + \sigma_{th} \quad (1.15)$$

where  $\sigma_{\alpha}$  is the athermal flow stress,  $\sigma_{th}$  is the thermal flow stress.

$$\sigma_{th} = \frac{M\Delta G_0 e^{-\beta T}}{Ab} \quad (1.16)$$

$$\beta = -C_3 + C_4 \ln \dot{\epsilon} \quad (1.17)$$

where  $M$  is the direction factor,  $\Delta G_0$  is the free energy of thermal activation at 0 K,  $b$  is the burger vector,  $\beta$  is a parameter related to strain and strain rate. For BCC metal,  $A$  is a material constant. But for FCC metal,  $A$  is regarded as  $\sqrt{\epsilon}$ . Therefore, the thermal flow stresses for BCC and FCC metal are written separately as

$$\sigma_{th} = C_1 \exp(-C_3 + C_4 \ln \dot{\epsilon}) \quad (1.18)$$

$$\sigma_{th} = C_2 \epsilon^{\frac{1}{2}} \exp(-C_3 + C_4 \ln \dot{\epsilon}) \quad (1.19)$$

Combining the athermal and thermal parts, the equations for BCC and FCC metals are

$$\sigma = C_0 + C_1 \exp(-C_3 + C_4 \ln \dot{\epsilon}) + C_5 \epsilon^n \quad (1.20)$$

$$\sigma = C_0 + C_2 \epsilon^{\frac{1}{2}} \exp(-C_3 + C_4 \ln \dot{\epsilon}) \quad (1.21)$$

where  $C_0$ ,  $C_1$ ,  $C_2$ ,  $C_3$ ,  $C_4$ ,  $C_5$  and  $n$  are material constants. It can be seen from the two equations that the strain hardening rate of BCC materials is not affected by strain rate or temperature; while for FCC materials, the strain hardening rate is strongly affected by the two parameters. In fact, the coupling effects between strain, strain rate and temperature should be considered in a more effective constitutive way. Therefore, some researchers made several modifications to the Z-A model [62,63].

- **Bodner-Parton (B-P) model**

In 1975, Bodner and Parton [57] proposed a model to describe the deformation behaviour of materials under large deformation and arbitrary loading histories. The model divides the

total deformation into elastic and plastic components, which are functions of strain state variables at all deformation stages. The model is given as

$$\dot{\varepsilon}^p = \frac{2\sigma}{\sqrt{3}|\sigma|} D_0 \exp \left[ - \left( \frac{n+1}{2n} \right) \left( \frac{Z}{\sigma} \right)^{2n} \right] \quad (1.22)$$

$$Z = Z_1 + (Z_0 - Z_1) \exp \left( - \frac{m \int \sigma d\varepsilon^p}{Z_0} \right) \quad (1.23)$$

where  $Z_0$ ,  $Z_1$ ,  $m$  and  $n$  are material constants needed to be determined.  $D_0$  is the maximum strain rate during tests.

- **Rusinek-Klepaczko (R-K) model**

Inspired by thermally activated dislocation motion theory [64], the RK model is given as a sum of two components, the internal stress  $\sigma_\mu(\bar{\varepsilon}^p, \dot{\varepsilon}^p, T)$  and the effective stress  $\sigma^*(\dot{\varepsilon}^p, T)$ , defining the strain hardening effect and the thermal activation process, respectively.

$$\bar{\sigma}(\bar{\varepsilon}^p, \dot{\varepsilon}^p, T) = \frac{E(T)}{E_0} (\sigma_\mu(\bar{\varepsilon}^p, \dot{\varepsilon}^p, T) + \sigma^*(\dot{\varepsilon}^p, T)) \quad (1.24)$$

The two components are multiplied by a parameter  $\frac{E(T)}{E_0}$  to represent the temperature dependent Young's modulus,

$$E(T) = E_0 \left\{ 1 - \frac{T}{T_m} \exp \left[ \theta^* \left( 1 - \frac{T}{T_m} \right) \right] \right\} \quad (1.25)$$

where  $E_0$ ,  $T_m$ ,  $\theta^*$  are Young's modulus at 0 K, the melting temperature and the characteristic homologous temperature of the tested material, respectively. A strain hardening equation similar to the Swift law is used to describe the internal stress  $\sigma_\mu(\bar{\varepsilon}^p, \dot{\varepsilon}^p, T)$ . The plasticity modulus  $B(\dot{\varepsilon}^p, T)$  and the strain hardening parameter  $n(\dot{\varepsilon}^p, T)$  are both strain rate and temperature dependent,

$$\sigma_\mu(\bar{\varepsilon}^p, \dot{\varepsilon}^p, T) = B(\dot{\varepsilon}^p, T) (\varepsilon_0 + \bar{\varepsilon}^p)^{n(\dot{\varepsilon}^p, T)} \quad (1.26)$$

$$B(\dot{\varepsilon}^p, T) = B_0 \left[ \left( \frac{T}{T_m} \right) \log \left( \frac{\dot{\varepsilon}_{max}}{\dot{\varepsilon}^p} \right) \right]^{-v} \quad (1.27)$$

$$n(\dot{\varepsilon}^p, T) = n_0 \left\langle 1 - D_2 \left( \frac{T}{T_m} \right) \log \left( \frac{\dot{\varepsilon}^p}{\dot{\varepsilon}_{min}} \right) \right\rangle \quad (1.28)$$

where  $\varepsilon_0$  refers to the value corresponding to the yield point during quasi-static tests;  $\dot{\varepsilon}_{max}$  and  $\dot{\varepsilon}_{min}$  are the maximum and minimum strain rate experienced by the tested material, respectively;  $B_0$  and  $D_2$  are material constants;  $v$  is the temperature sensitivity parameter and  $n_0$  is the strain hardening parameter at 0 K. The operator  $\langle x \rangle = x$  if  $x > 0$  otherwise  $\langle x \rangle = 0$

if  $x \leq 0$ . The effective stress  $\sigma^*(\dot{\epsilon}^p, T)$  defines the flow stress induced by thermal activation process using an Arrhenius equation:

$$\sigma^*(\dot{\epsilon}^p, T) = \sigma_0^* \left\langle 1 - D_1 \left( \frac{T}{T_m} \right) \log \left( \frac{\dot{\epsilon}_{\max}}{\dot{\epsilon}^p} \right) \right\rangle^{m^*} \quad (1.29)$$

where  $\sigma_0^*$  is the effective stress at 0 K,  $D_1$  and  $m^*$  are material constants. In order to describe the thermo-viscoplastic behavior of aluminium alloy more accurately, Rusinek et al. [22] developed two extensions of the R-K model. They define the negative strain rate sensitivity and the viscous drag phenomenon of aluminium alloys respectively. The first extension is expressed as

$$\sigma(\bar{\epsilon}^p, \dot{\epsilon}^p, T) = \frac{E(T)}{E_0} [\sigma_\mu + \sigma^* + \sigma_{ns}(\dot{\epsilon}^p, T)] \quad (1.30)$$

where  $\sigma_{ns}(\dot{\epsilon}^p, T)$  is the term defining the negative strain rate sensitivity. It is related to strain rate and temperature and is expressed as

$$\sigma_{ns}(\dot{\epsilon}^p, T) = \sigma_0^{ns} \log \left( \frac{\dot{\epsilon}_{\text{trans}}}{\dot{\epsilon}^p} \right) \left\langle 1 - D_3 \left( \frac{T}{T_m} \right) \log \left( \frac{\dot{\epsilon}^p}{\dot{\epsilon}_{\max}} \right) \right\rangle \quad (1.31)$$

where  $\sigma_0^{ns}$  defines the stress decrease due to dynamic strain aging,  $D_3$  is the material constant describing the reciprocity between strain-rate and temperature and  $\dot{\epsilon}_{\text{trans}}$  is the transition strain rate between positive and negative strain rate sensitivity. The second extension of the R-K model is developed to describe viscous drag effect in FCC metal during high strain rate deformation. It is given as

$$\sigma(\bar{\epsilon}^p, \dot{\epsilon}^p, T) = \frac{E(T)}{E_0} [\sigma_\mu + \sigma^* + \sigma_{ath}(\dot{\epsilon}^p)] \quad (1.32)$$

where  $\sigma_{ath}(\dot{\epsilon}^p)$  is the term accounting for the viscous drag effect. It depends on strain rate,

$$\sigma_{ath} = \sigma_{ath} \left( \left( \frac{M^2 B}{\rho_m b^2} \right), \dot{\epsilon}^p \right) \propto \dot{\epsilon}^p \quad (1.33)$$

$$\sigma_{ath}(\dot{\epsilon}^p) = \chi [1 - \exp(-\alpha \dot{\epsilon}^p)] \propto \dot{\epsilon}^p \quad (1.34)$$

$$\alpha = \frac{M^2 B}{\rho_m b^2 \tau_y} \quad (1.35)$$

where  $M$ ,  $B$ ,  $\rho_m$  and  $b$  are the Taylor factor, the drag coefficient, the mobile dislocation density and the magnitude of the burger vector, respectively.  $\chi$ ,  $\alpha$  and  $\tau_y$  are the material constant, an effective damping coefficient and the high temperature yield stress, respectively.

It is obvious that the viscous-drag term in the extended R-K model can compensate the underestimation of flow stress obtained by Arrhenius equation and correct deformation behaviour of materials at high strain rates, especially at elevated temperatures.

- **Mechanical Threshold Stress model (MTS)**

Nowadays, with the availability of powerful computing machines, it is possible to simulate processes such as high-speed machining, FSW, forming, vehicle impact, etc. In these processes, the strain rate is much higher ( $10^3 \text{ s}^{-1}$  to  $10^9 \text{ s}^{-1}$ ) and the temperatures involved are higher than  $0.6 T_m$ . Thus, an important component in numerical modelling of plastic deformation under these conditions is a model that describes the evolution of flow stress over a wide range of strain rates and temperatures [59]. The appropriate model for this purpose is the mechanical threshold stress.

The MTS model is based on two major assumptions: 1) Thermally activated dislocation motion are dominant and viscous drag effects on dislocation motion were small. 2) High temperature diffusion effects are absent. This assumption limits the range of applicability of the model to the temperatures less than around  $0.6 T_m$  [59]. The Mechanical Threshold Stress (MTS) model has the follow form:

$$\sigma_y(\varepsilon_p, \dot{\varepsilon}, T) = \sigma_a + (S_i \sigma_i + S_e \sigma_e) \frac{\mu(p, T)}{\mu_0} \quad (1.36)$$

Where  $\sigma_a$  is the athermal component,  $\sigma_i$  is the intrinsic component of the flow stress due to barriers to thermally activated dislocation motion,  $\sigma_e$  is the strain hardening component of the flow stress,  $(S_i \sigma_i + S_e \sigma_e)$  are strain-rate and temperature dependent scaling factors, and  $\mu_0$  is the shear modulus at 0 K and ambient pressure [60]. This model provides a more accurate representation of the deformation behaviour of the material over a wide range of temperatures and strain rates. However, this and other physics-based models are not always preferred by industries, as they often require more data from precisely controlled experiments. More importantly, these models involve many more constants and material properties than empirical models, which may not be readily available in the open literature.

- **Constitutive model considering dynamic recovery and dynamic recrystallization**

Several other physical-based models exist which are based on the microstructure changes take place during thermal deformation process at different loading conditions. Lin et al. [37]

divided the complete thermal deformation process of most metal material into four stages. Stage I (work hardening stage), Stage II (Transition stage), Stage III (Softening stage) and Stage IV (Steady stage), especially at relatively low strain-rate, which are clearly shown in Figure. 1.11.

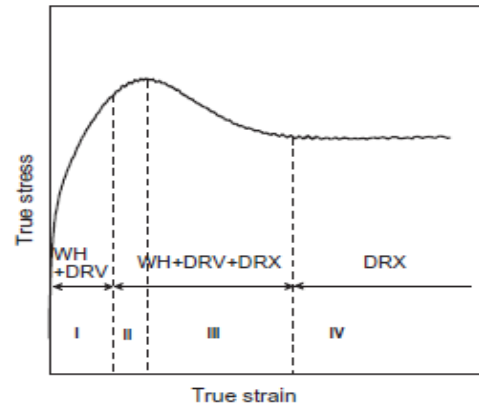


**Figure 1.11:** Typical flow stress curve [37]

In stage I (Work hardening stage), the work hardening (WH) rate is higher than the softening rate induced by dynamic recovery (DRV), and thus the stress rises steeply at micro-strain deformation then increases at a decreased rate, followed by stage II (Transition stage). In transition stage, the competition between the work hardening and the softening phenomenon induced by dynamic recovery, as well as the dynamic recrystallization (DRX), takes place. In addition, the flow stress still increases, but the increase rate continuously decreases. In stage III (Softening stage), the stress drops steeply, which is related with dynamic recovery, dynamic recrystallization, etc. Finally, stage IV (Steady stage): the stress becomes steady when a new balance between softening and hardening appears [6] especially at relatively low strain-rate.

The model developed on [65] dynamic recrystallization for aluminium alloy at low strain rate, it consists of three main components: 1) internal variables that constitute the microstructure, 2) evolution of these internal variables, and 3) constitutive equations. The microstructure was described as an aggregate of sub-grains delimited by low angle grain boundaries (LAGBs) and high angle grain boundaries (HAGBs). Three internal variables were used: the density of dislocations inside the sub-grains ( $\rho_i$ ), sub-grain size ( $D$ ), and the fraction of LAGBs ( $f_{LAGB}$ ). During a strain increment ( $d\varepsilon$ ) dislocation density increases by



$hd\varepsilon$  and  $r\rho_i d\varepsilon$  annihilate or are incorporated in LAGBs by dynamic recovery. A part  $\rho_i dV$  is consumed by the migration of HAGBs.

$$d\rho_i = hd\varepsilon - r\rho_i d\varepsilon - \rho_i S_v f_{HAGB} v_M d\varepsilon / \dot{\varepsilon} \quad (1.37)$$

$f_{HAGB}$  = fraction of HAGBs,  $v_M$  = average velocity of grain boundaries,  $S_v$  is the surface of boundaries, and  $h$  and  $r$  are the hardening and recovery coefficients, respectively. Among the recovery part, a fraction  $\beta$  is annihilated, a fraction  $(1 - \beta)\alpha$  is consumed by the formation of new LAGB, and the rest  $(1 - \beta)(1 - \alpha)$  is absorbed by the existent LAGBs and HAGBs. The incorporation of dislocations in LAGBs induces a misorientation increase ( $d\theta$ ):

$$d\theta = (1 - \beta)(1 - \alpha) \frac{b}{2n} D(r\rho_i) d\varepsilon \quad (1.38)$$

$n$  = constant,  $b$  is the Burger's vector, . The evolution in total area of boundary per unit volume is given by  $dSV = dSV^+ - dSV^-$ , where  $dSV^+$  corresponds to the area of LAGBs created during straining and  $dSV^-$  corresponds to the area of boundary eliminated by the HAGBs migration:

$$dS_v^+ = (1 - \beta)\alpha \frac{b}{n\theta_0} (r\rho_i) d\varepsilon \quad (1.39)$$

$$dS_v^- = S_v dV = \frac{S_v^2 f_{HAGB} v_M d\varepsilon}{\dot{\varepsilon}} \quad (1.40)$$

The fraction of LAGBs and the density of dislocations forming the LAGBs,  $\rho_w$  were calculated using the distribution function of the misorientations ( $\varphi(\theta)$ ).

$$f_{HAGB} = \int_{\theta_0}^{\theta_c} \varphi(\bar{\theta}, \varepsilon) d\theta \quad \& \quad \rho_w = \left( \frac{2n}{bd} \right) \int_{\theta_0}^{\theta_c} \varphi(\bar{\theta}, \varepsilon) \bar{\theta} d\theta \quad (1.41)$$

$\theta_0$  = minimum misorientation angle of new created LAGB,  $\bar{\theta}$  = mean misorientation, and  $\bar{\theta}$  = critical angle for the transformation of LAGB into HAGB. The flow was calculated using the Taylor factor  $M$ , the shear modulus  $G$ , and material constants  $\alpha_1$ ,  $A_1$  and  $A_2$ .

$$\sigma = M\alpha_1 Gb(A_1 \sqrt{\rho_i} + A_2 \sqrt{\rho_w}) \quad (1.42)$$

Meyers et al [66] presented a review of physically based models for plasticity due to dislocation glide as well as twinning. They also discussed high strain rates phenomena. Lindgren et. al. [67] developed a flow stress-based model on a coupled set of evolution equations for dislocation density and vacancy concentration. This model takes for dynamic strain aging through diffusing solutes parameter. Kalhori et al [68] improved the Lindgren and coworkers' model and later modified for various materials. It provides more accurate

representation for the deformation behaviour of the material over a wide range of temperatures and strain rates. However, it contains large number of material parameters and are not readily available. The determination of material parameters requires some special apparatuses which considers all the thermomechanical constraints. Therefore, physical-based models are often very difficult for many investigators without precision testing apparatuses.

### **1.3 Shear testing of metallic alloys**

The use of uniaxial tensile and compression tests to characterize the mechanical behaviour of materials is widespread, including at dynamic strain rates. The evaluation of the deformation and strength of components is based on material parameter. These parameters can be derived from tensile or compression test data in a simple way. In addition, most constitutive material models rely heavily on tensile testing. Although widely used, tensile and compression tests have some inherent shortcomings. These shortcomings are even more pronounced at high strain rates. In compression tests at high strain rates, material characterization is hampered by both radial inertia and sample barrelling. In high strain rate tensile testing, the higher yield stress level that is often observed for metal alloys promotes early necking of the specimen. As soon as necking develops, the heterogeneous strain distribution across the gauge section and non-axial stresses in the neck complicate the interpretation of the experimental results. The measured load and corresponding strain can no longer be directly translated into a stress-strain response of the material. This is especially a problem for metals with low strain hardening capabilities, such as some titanium and aluminium alloys.

Shear tests, on the other hand, do not suffer from the disadvantages mentioned above. No thinning or other changes of the gauge cross section occur in a well-designed shear specimen. As a consequence, diffuse and localised necking is avoided. Moreover, shear tests provide valuable data on material fracture parameters. Unlike uniaxial tensile tests, where ductile metal failure results from highly localized deformations after necking, fracture during a shear test can be attributed to material failure instead of geometric instability. In a shear test, damage growth is retarded thanks to the lower stress triaxiality and generally larger strains including stage IV hardening strains are obtained in a shear test, which enables more accurate material modelling [58,69].

In a lot of manufacturing processes, the deformation within the material is generated by shear stress and not by tensile or compressive stresses: Turning, milling, drilling, and friction stir welding. In addition, under dynamic loads, in particular, such as forging, metal forming, collisions, and ballistic impacts, materials are more susceptible to shear failure. Hence, the understanding of the material behaviour under shear loading has great importance for a researcher to develop an accurate material model. For such material behaviour analysis, shear tests provide a useful means to investigate the mechanisms leading to shear localization such as adiabatic shear band and evolution of the microstructure at a wide range of temperature, strain, and strain rates. It is therefore essential to test the material under stress conditions similar to those it will undergo during the manufacturing process. Shear tests can be carried out by a simple shear test (e.g., using a suitable sample geometry to convert tensile or compressive loading to shear) or by direct shear loading (e.g., a torsion test on thin-walled tubular specimens).

### **1.3.1 Simple shear test specimen**

Simple shear test can be performed by appropriate specimen geometry by using traditional tensile and compression apparatus in static and dynamic loading. It is also called a combined loading technique with dominate shear deformation. It has a several advantages such as the necking or barrelling in the specimen can be eliminated, without the Poisson-ratio effect and large strain and strain rate can be obtained easily [69]. However, the design of specimen is very important.

In the last decade, many researches have shown the different specimen geometries used to characterize the behaviour of materials in shear. The first simple shear specimen was developed by Hundy and Green [70] under tensile loading to study the shear properties of the material. Meyer and Manwaring [71] designed the “Hat specimen” to study shear localization behaviour under compression loading, and later this specimen was modified and used by many other researchers. Another group of a specimen such as double shear specimen [72], single or double edge [64], step or dumbbell [73], compact forced simple- shear (CFSS)[74], truncated conic [75], indentation [76], and inclined flyer were designed to study the shear behaviour of the various metals and alloys. Dodd, and Bai [77] gave a detailed critical review on different kinds of shear specimens with their advantages and disadvantages.

Following are some of the shear specimens used by many researchers to study the material behaviour under shear testing.

- **Double notch shear specimen**

The double shear specimen, as shown in Figure 1.12, was originally used by Campbell and Ferguson [72] to study the sensitivity of mild steel under dynamic strain rate and temperature. The centre portion of the specimens is in contact with the input bar while the two edge supports are attached to an output tube. With the relative displacement between the centre part and the two edge supports, the area between the two parts undergoes shearing.

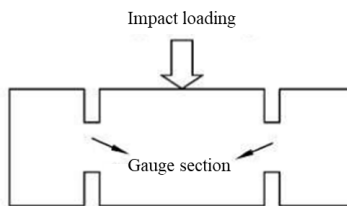


**Figure 1.12:**Double-shear specimen [72]

While testing the specimens in double shear, the edge supports of the specimens bend significantly. As a result, the strain uniformity in the shear zones is quite low and the corresponding stress state also clearly deviates from pure shear. In order to solve this problem, a lot of work has been done regarding the optimization of specimen geometry [48,78–80]. Among them, Shi and Merle [80] designed a modified double shear specimen and a clamping device to limit the lateral movement of the specimen, Figure 1.13. As a result, a much more uniform stress state in the shear zones is achieved.

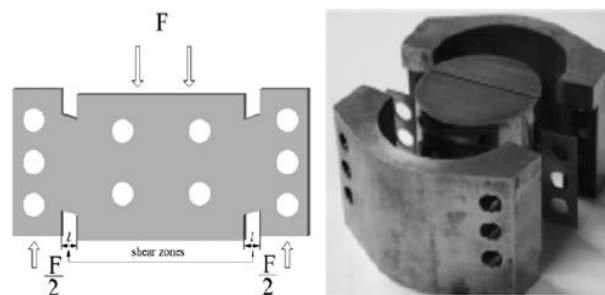


**Figure 1.13:**Modified double-shear specimen and the clamping system [80].

Double shear specimens can be used for characterization of shear behaviour, and the visible shear zone makes in situ observation of strain and temperature possible. A

disadvantage of this specimen is that the initiation of failure is caused by stress concentration at the corners of the gauge rather than the material itself [81].

- **Hat shape specimen**

One other interesting shear specimen design is the hat-shaped specimen, invented by Meyer et al [71] in 1986. This is an axisymmetric specimen consisting of a hat-shaped upper part and a brim-shaped lower part. When a compressive force is applied to its surface, the shear zone between the two parts is deformed. In general, the diameter of the hat portion is larger than that of the brim portion and by changing the relative diameters of the two portions, a shear-compression stress state in the shear zone is generated.

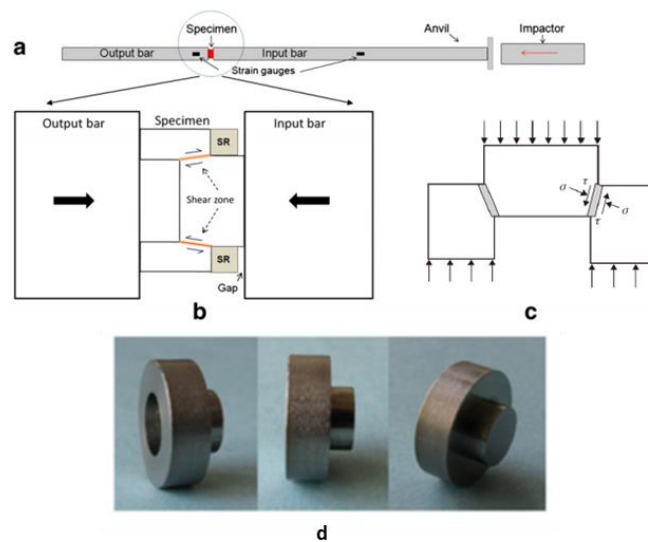


**Figure 1.14:** a) Split Hopkinson pressure bar b) stop ring c) Schematic diagram of the hat-shaped specimen, representation of the shear zone d) Hat shaped specimens[75].

Hat-shaped specimens are commonly used to study the formation of shear bands in metallic materials [82,83]. By loading the specimens on a conventional Split Hopkinson Pressure Bar (SHPB) and using a stop ring [83], Figure 1.14, the evolution of shear localization over a wide range of strain rates and temperatures can be studied. In addition, the width of the shear zone in the hat-shaped specimens can be designed to be very small, less than 1 mm. Therefore, very high strains and strain rates can be achieved. Although hat-shaped specimens are widely used for shear band characterization, it turns out that the distribution of stresses and strains within the shear zone is inhomogeneous and the measured shear stress-shear strain curves are unreliable. Therefore, hat-shaped specimens should be used with great caution when quantitative material stress-strain data are sought.

- **Eccentric Notch shaped Shear Specimen**

Peirs et al [84] presented the specimen geometry shown in Figure 1.15. The specimen was designed for sheet metal shear testing over a wide range of strain rates. The specimen is intended to be tested using existing tensile testing equipment. For dynamic testing, the specimen is glued into Kolsky bar in tension. The eccentric notches in the specimen are the result of numerical studies performed in order to optimize the strain state in the specimen section intended for the gauge. Optimal notches result in a nearly uniform shear strain state in the gauge section. Also, the grating pattern is used to study the strain in shear region.

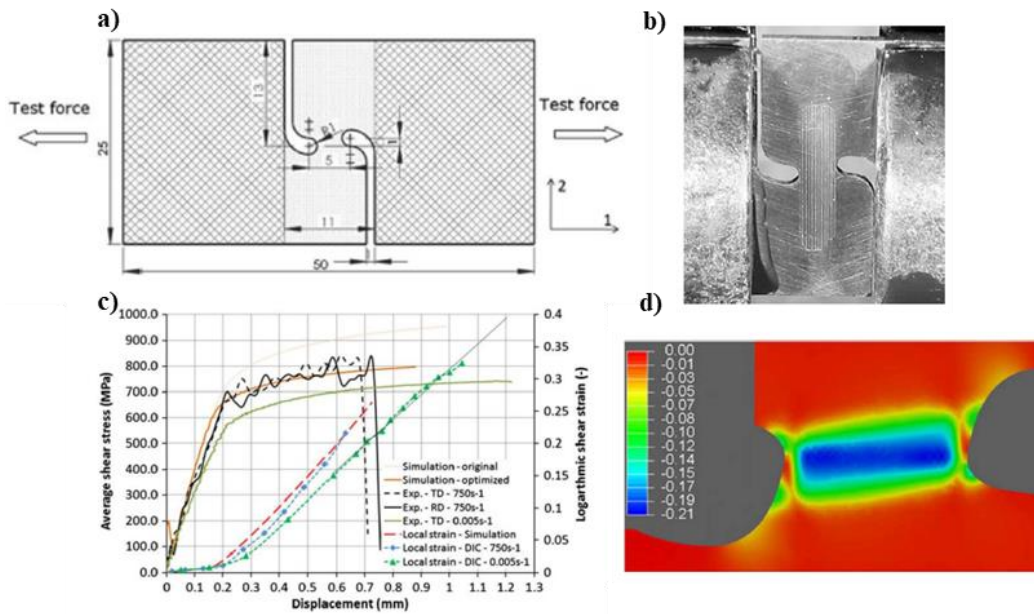


**Figure 1.15:** a) Eccentric notch shape shear specimen (dimensions in mm) b) Sample glued between Hopkinson bars before testing. c) Simulated and experimental data using the eccentric notch specimen d) DIC data Measured on the surface of the eccentric notch specimen[84].

Static and dynamic shear tests were performed on Ti-6Al-4V sheet using this specimen geometry. During a test, the deformation of a grating of lines attached to the sample is recorded by a high-speed camera. This grating is used to obtain the local deformation in the section of the gauge as shown in Figure 1.15 b). Digital Image was used to measure the strains directly on the surface of the specimens during the tests. Figure 1.15 d) shows the typical contour plot of  $\epsilon_{12}$  during a test indicating that much of the deformation is limited to within the intended gauge section and a nearly uniform state of shear strain has been achieved with the proposed geometry. Experimental and simulated shows some promising data. However, the deformation obtained with this specimen is not very high.

There are several other specimen geometries are developed but despite the fact that the majority of these combined loading specimens are failed to produce pure shear stress-strain. A pure shear stress state is particularly important for shear deformation, failure and microstructure behaviour study. However, it is limited by specimen dimensions, a shear-compression or shear tension stress state is often obtained [84–86]. Moreover, it is also very difficult to determine shear stress-shear strain relationship of materials accurately. For example, in the hat shape specimen, the quantitative assessment of the specimen's stress-strain response is very difficult. If the stress state inside specimen shear zones is not pure shear or the stress components distribution is inhomogeneous [87], it is difficult to extract the real shear stress-shear strain behaviour of materials from globally obtained force-displacement data.

### 1.3.2 Torsion test specimen

For several materials, a most straightforward way of shear testing consists of imposing a torsional deformation onto a thin-walled tubular specimen as shown in Figure 1.16 [88]. Dynamic loading conditions are generally achieved in a split Hopkinson bar torsion setup. A well-designed specimen ensures homogeneous shear stresses and strains prior to strain localisation in the gauge section of the specimen with a small (or even non-existent) hydrostatic stress[89]. Furthermore, the shear zone is accessible for high speed camera observation.

Dynamic torsion test, by a modified Split Hopkinson Bar (SHB) was first introduced by Duffy and Campbell [59] to study strain rate sensitivity of aluminium alloys. During torsion tests, the specimen gauge geometry remains unchanged, shear stress-shear strain curves can be measured directly. However, restricted by the maximum torque that can be stored in the incident bar, the maximum strain rate during torsion testing is limited, even for specimens with small shear zones [64].

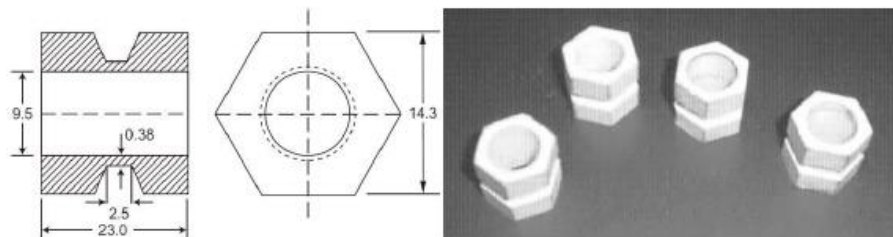


**Figure 1.16:** Thin wall tubular specimen [88]

The experimental work produced by Marchand and Duffy [90] widely used for material modelling in which they studied adiabatic shear band (ASB) by subjecting HY-100 steel specimen to high strain rate torsion. Split Hopkinson Torsion Bar shown in Figure 1.17.

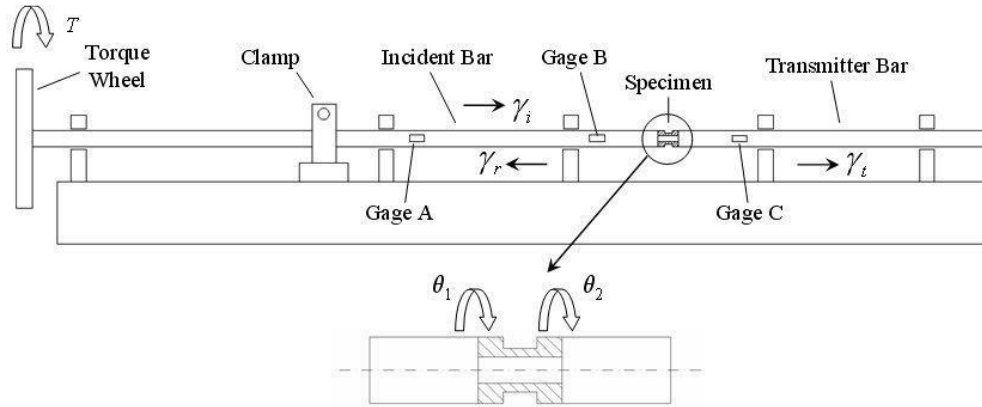


**Figure 1.17:**Schematic diagram of a torsion split Hopkinson bar apparatus

The average stress and strains and the deformation are measured from the applied grid lines. The stages of deformation distinguished from the inclination of the grid lines in the different frames shown in Figure 1.18. From Homogenous strain (Frames 1,2,3) to heterogeneous deformation (Frame 4) until the ASB initiates (Frame 5) and propagates and causes a progressive drop in strength and crack appear within the shear band (Frame 6).

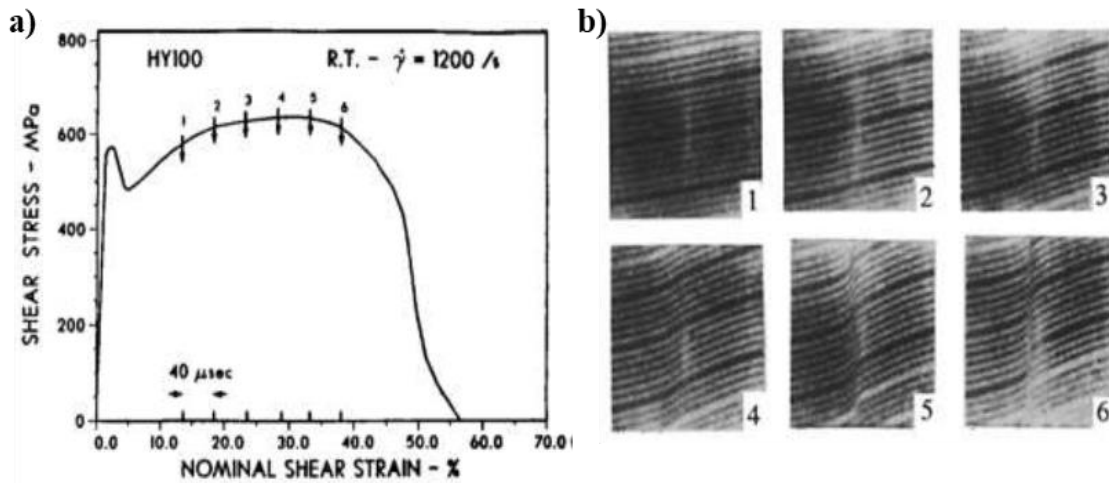


**Figure 1.18:**a) Stress-Strain behavior of HY-100 steel in dynamic shear. b) Photographs of the grid lines showing deformation pattern at instants of the numbered arrows in (a) [90]

This experiment demonstrates the significant consequence in the material of the presence of ASB and the subsequent crack supposedly formed by the coalescence of micro



void. There are various other experiments evidencing that the premature material failure caused by the ASB is preceded by the formation, growth and coalescence of micro-voids. For example, the microscopic observation by Liu et al. [91] in Figure. 1.19 of the crushed Ti-6Al-4V bars showed ASBs containing voids and coalesced voids (cracks).

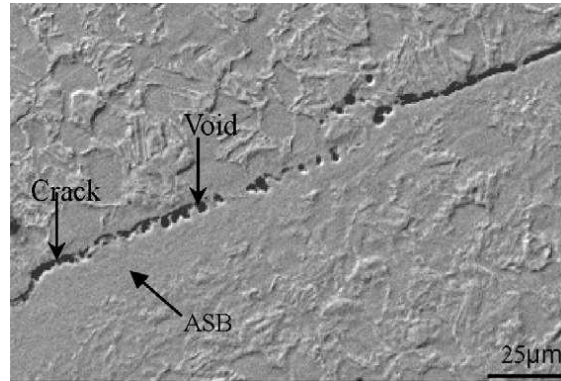


**Figure 1.19:**Micro-voids and coalesced voids (cracks) seen in the wake of ASB in Ti-6Al-4V alloy. After [91].

Despite the fact that torsion of thin-walled tubes is generally accepted as an accurate and reliable test technique to study shear localization behaviour of material, torsion tests are not that widely used. Obviously, testing of thin-walled tubes requires a torsion setup, which is not that common. In addition to all the benefits inherent to simple shear testing (section 3.1), dynamic torsion tests have some additional advantages: A stress state close to pure shear is obtained in the torsion sample, regardless of the material under investigation. As opposed to the simple shear tests samples discussed in section 3.1, the geometry of a torsion sample does not need to be optimized for each material individually to obtain the desired stress state. Unlike the simple shear test specimen, the torsion specimen does not have notches or free edges which disturb the stress and strain fields. Thus, obtained material test data provides valuable information.

#### 1.4 Intermediate Strain Rate Testing Devices

The existing commercial and traditional test devices used to determine material parameters for constitutive models are mainly divided according to the loading rate (or at different strain rates), from low to high. Table 1.5 provides a representation of the range of applicable strain rates covered by existing test machines, including types of loading, such as tension, compression, and shear.

**Table 1.5:**Characterization of the machines based on the strain rate and type of loading.

Testing technique	Applied strain rate ( $s^{-1}$ )		
	Low strain rate ( $\leq 10^1$ )	Intermediate strain rate ( $10^1 - 10^3$ )	High strain rate ( $> 10^3$ )
Compression Tests	Conventional load frame and servo-hydraulic machine	Commercial machines like MTS, Shimadzu, Instron, etc., Special Servo hydraulic load frames, drop tower, Flywheel device	Split Hopkinson pressure bar, Gas gun, Taylor impact test
Tensile Tests			Split Hopkinson bar in tension, Flyer plate, expanding ring
Shear tests	Conventional shear test, special servo-hydraulic frames, Torsion test	-	Compressive/tensile shear apparatus, Hopkinson Klosky bar in torsion

Among the three strain rate divisions in Table 1.5, conventional load frame and standard servo hydraulic testing machines [77,92–94] are generally used for quasi-static strain rates in the range of  $\leq 10^1 s^{-1}$  with different load conditions. These tests are called quasi-static because the specimen and the test machine are in static equilibrium during the test. For high strain rate testing  $> 10^3 s^{-1}$ , the split Hopkinson pressure bar (SHPB) method [95] is often used. In the last decade, many proven experimental techniques have been developed for high strain rate testing, e.g., compression loading, drop weight [96], SHPB [97], and gas guns [98] are regularly used. For tensile loading, the split Hopkinson tension bar (SHTB) [99–101], flyer plate impact test [102], and the expansion ring [103] are used. For torsion experiments, the torsional split Hopkinson bar (TSHB) with different loading mechanisms such as pre-stored energy loading [104], explosive loading [89], direct impact loading [105], and electromagnetic loading [106] are generally used. However, tests at an intermediate strain rate in the range of  $10^1$  to  $10^3 s^{-1}$  are not very common, and neither servo-hydraulic machines nor SHB techniques are suitable for testing with an intermediate strain rate regime.

Numerous methods have been introduced to bridge the gap between quasi-static and high strain rate testing in order to provide experimental data for engineering materials. Servo-hydraulic machines were considered as a solution to perform tests with an intermediate strain rate regime. The results of such tests, however, are not very accurate. The problem is that during the experiment, stress–strain data are influenced by the effect of high inertia, and

records obtained from such machines are often noisy with large oscillations. As a result, servo-hydraulic machines only give reliable measurements at strain rates below  $10 \text{ s}^{-1}$ .

After the development of the split Hopkinson bar technique [95] in 1949, a few researchers tried to modify classical dynamic split Hopkinson pressure bar device to achieve a deformation rate in the intermediate rate regime by increasing the loading time [107]. However, the main drawback of the modified device is that the duration of the test is limited to the length of the bars [108]. Such a duration does not allow the significant strain to be accumulated in the specimen at medium strain rates. Therefore, an alternative loading technique is required. Over the last decade, some researchers have developed specialized test machines capable of performing intermediate strain rate tests to study material characterization, such as special commercial machines designed by Instron, Shimadzu, etc.[109,110]; elastic-bar-type systems (ISO 26203-1: 2018) [111], modified servo-hydraulic load frames (ISO 26203-2:2011) [112], hybrid testing apparatus [113], drop tower [114], flywheel device [115], and flywheel wedge[116].

The material response at intermediate strain rates is of great interest to the automotive industry and producers of electronic packaging [117]. Additionally, intermediate strain rates have been recognized as being important in the transitioning of material response and changing of the material deformation mechanism from low to high strain rates [118,119]. Therefore, in the past decade, the material response at intermediate strain rates has attracted more attention. In addition, material properties at intermediate strain rates are rarely characterized due to experimental difficulties leaving a significant gap in the experimental data between low and high strain rates for high-fidelity strain rate dependent material model development.

### **1.4.1 Existing Intermediate Strain Rate Testing Devices**

#### **1.4.1.1 High Speed Servo-hydraulic Machines**

Over the past decade, the experts from various industries such as Instron, MTS, Shimadzu, and Zwick/Roell have developed a new family of high-speed servo hydraulic testing machines specifically designed to cope with the dynamics of intermediate strain rate testing [109,110,120], and after these devices are used in a number of applications to predict material behaviour, for instance; in the landing gear on aircraft or the crash impact of a road

vehicle, all of these examples involve one or more components of a product that are subjected to intermediate strain rate impact  $<10^3 \text{ s}^{-1}$ . For example, in Figure 1.20, the strain rate distribution of passenger car is shown during the sudden dynamic load impact

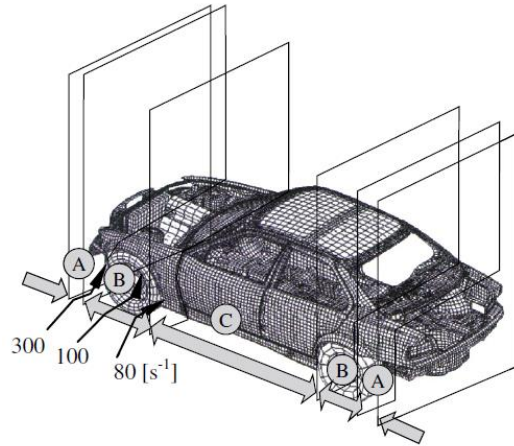


**Figure 1.20:** Design zones for car body structures [2] A = Deformation zone at lower impact speed B = Deformation zone at higher impact speed C = Stiff and stable compartment [120].

High-speed servo hydraulic machines are used for all kinds of impact loadings like dynamic tension, compression, bending, and shear loading. The most important high-speed test mode is the tension test. For example, Figure 1.21 shows the schematic diagram of the high-speed testing machine [121]. The stroke speed is controlled by the opening and closing of the servo-valve of hydraulic supply. The test machine can deliver a speed range from 1 mm/s to 20 m/s.

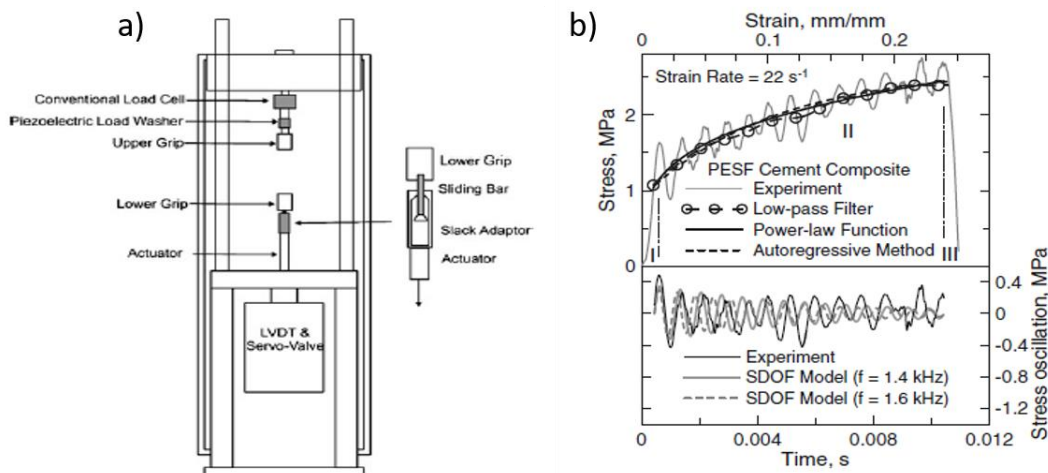


**Figure 1.21:** a) Schematic diagram of the high-speed testing machine, b) Typical response of cement composite and comparison of the stress oscillation between the SDOF (single degree of freedom) model and the experiment at a nominal strain rate of  $22 \text{ s}^{-1}$  [121].

The strain rate data obtained from this machine is from quasi-static to intermediate strain rates. Dynamic load is introduced to the lower grip through a slack adaptor that consists of a hollow tube and a sliding bar with a conical tip. When the machine is actuated, the hollow tube travels freely with the actuator over a distance to reach a specified velocity before making contact with the cone-shaped end of the sliding bar that is connected to the lower grip. The slack adaptor eliminates the inertia effect of the lower grip and actuator in its acceleration stage. However, the sudden engagement with the upper portion of the setup generates a high amplitude stress wave, causing oscillations at the system's natural frequency, i.e., system ringing [122]. A conventional piezoelectric load cell installed in the machine shows the vibration and oscillating signals. At strain rates above  $50 \text{ s}^{-1}$  these systems become unreasonably difficult to acquire load data. Therefore, experimentalists are forced to use smoothing or filtering the load test data by using low-pass filters, averaging or other algorithms (e.g., power-law function) [123], or the spring mass damping mode. However, the accuracy of such filtering procedures, to a great extent, depends on the user's choice of the filtering algorithm. It also includes a risk of losing some important characteristics with respect to the hardening behaviour of the tested material.

### **1.4.1.2 Hybrid Testing Apparatus**

In 1996, LeBlanc et al. [113] designed and introduced a unique hybrid testing apparatus to perform intermediate strain rate tests in order to improve the load measuring data that observed in the high-speed servo hydraulic machines. This device was developed by combining a servo-hydraulic machine with the split Hopkinson bar technique. The apparatus combines the loading capabilities of a servo-hydraulic testing machine and the load measuring technique of a Hopkinson bar. The bar is freely suspended against the specimen. When the specimen is compressed or elongated against the bar, the loading of the specimen is transmitted to the bar at the elastic wave velocity. The load in the bar is determined from strain gauges located close to the loading end; the measurement is free of disturbance until the reflected wave reaches the gage and interferes with the loading wave. The stress in the test specimen is assumed to be uniaxial and can be calculated using the elastic wave analysis of the Hopkinson bar.

The experimental test was carried out by Othman [124], using a standard servo-hydraulic machine MTS 819 with a maximum speed of 16 m/s, and the sample was loaded

in tension as shown in Figure 1.22 (a). A long steel bar with a length of 820 mm is attached to the upper crosshead of the machine. The strain gages are connected to the bar. These gage positions allow a good deconvolution of the signals. The specimen is attached to the bar and to the lower crosshead. The high-speed video camera is fixed in order to capture the displacement field using the digital image correlation (DIC) technique [124,125].

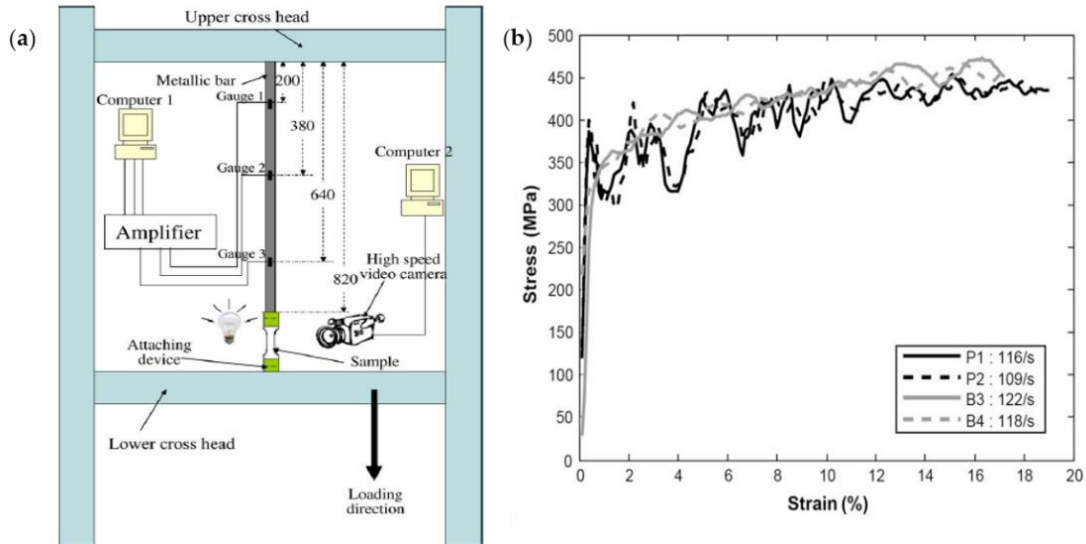


**Figure 1.22:**(a) modified hybrid machine and (b) stress–strain relation for aluminum obtained by the piezoelectric load sensor method (P1 and P2) and by the Hopkinson bar technique (B3 and B4) [124].

The load records are captured by using piezoelectric load sensor and Hopkinson bar technique and the stress–strain curves are compared from both techniques shown in Figure 2b. The stress curve recorded by using a piezoelectric load sensor shows large oscillations compared to the Hopkinson bar technique. The oscillations are caused by stress waves propagating through the piezoelectric load sensor including reflected waves. The stress waves also impinge upon the test specimen, as evidenced by the very small magnitude oscillations in the Hopkinson bar output shown in Figure 1.22(b). Therefore, it is apparent from these tests that the hybrid test technique significantly improves the quality of stress–strain test data in comparison with the traditional piezoelectric load cell. This new Hopkinson bar technique to measure the load shows a less oscillating behaviour at an intermediate strain rate around  $10^2 \text{ s}^{-1}$ .

The advantage of a hybrid testing apparatus is that it applies a continuous loading during the test, which gives more reliable stress–strain data. The load is directly derived from using the strain gage attached to the bar. However, the loading time of the test was only 1ms due

to the specific length of the bar, and this time duration does not allow enough strain in specimen. Furthermore, Othman et al. [124] modified the hybrid testing apparatus to improve the load measuring technique, by increasing longer time duration and to perform test at various strain rate regime by using the “wave separation method” [126,127].

### 1.4.1.3 Drop Tower

A drop tower apparatus [128,129] is typically used to study the crushing and collapsing behaviour of the material by dropping a mass on a structural component. It is mainly used to perform the test at medium strain rates. In recent years, very little effort has been made to develop special apparatus and devices that will allow drop towers to perform tests under various loads using accurate load measurement techniques such as the special piezoelectric load cell and Hopkinson bar technique [130]. In 2018, a new tensile testing device, the "Dropkinson" bar, inspired by the drop tower, was developed by Bo Song and his collaborators [114], which is capable of testing at an intermediate strain rate shown in Figure 1.23. Unlike the other devices explained above, the Dropkinson bar system is the same hybrid test rig.

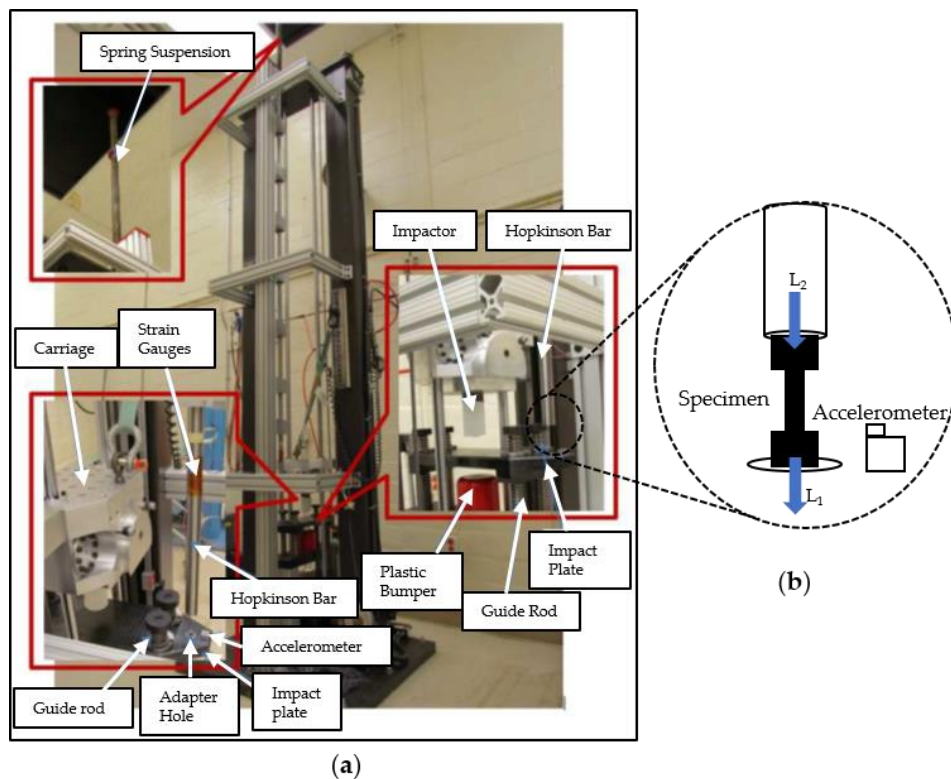


**Figure 1.23:**(a) overall view of Dropkinson bar test and (b) illustration of specimen displacement measurements [114].

The loading mechanism of the Dropkinson bar combines a drop table and a Hopkinson bar; it generates stable and durable impact velocity and facilitates deformation in the specimen at a constant strain rate. A long Hopkinson bar system was used to measure the load history to reduce the effect of inertia in the system. The Hopkinson bar is fixed parallel to the drop table. The drop table is used to generate a free fall impact of the trolley, as shown in Figure 1.23. A cylindrical steel impactor attached to the bottom of a carriage strikes the centre of the impact plate during the test.

The guided rods are situated in the impact plate to ensure uniaxial travel of the drop table. A plastic bumper is installed on the bottom of the impact plate to absorb the momentum. One end of the specimen is fixed to the impact plate adapter, and the other to the Hopkinson bar, as shown in Figure 1.23. Two strain gauges are attached to the bar to measure the load history. After the free fall of the carriage, the impactor attached to the bottom of the carriage hits the impact plate at the centre. The impact plate transfers the impact load to the tensile specimen in dynamic tension. The tensile stress wave transmits into the vertical bar through the specimen and bar end. The strain gauges attached to the bar, record the load history of the specimen. Furthermore, a custom laser extensometer is used to calculate the specimen strain. The strain rate obtained using the Dropkinson bar is up to  $600 \text{ s}^{-1}$  with a loading time of 0.5 ms, producing a strain of 0.27. A newly developed Dropkinson bar has shown reliable results. However, there is a significant amount of ringing noise; it may alter the force and strain signals due to the impact between the impactor and the moving metallic carriage.

#### **1.4.1.4 Flywheel Device**

The flywheel device is a dynamic testing apparatus designed by researchers to perform the test at intermediate and higher strain rates. In this rotary type of testing machine, the kinetic energy of the rotating flywheel is used to fracture specimens at different strain rates. The loading speed (mean strain rate) depends on the speed of the flywheel. The machine uses the kinetic energy stored in the flywheel to deform the specimen rapidly.

M. Manjoine et. al. [131] and M. F. Quinlan et al. [132] carried out dynamic tensile tests on various metallic materials using a flywheel device at strain rates up to  $1000 \text{ s}^{-1}$ . Load and deformation were measured using optical technologies, incorporating a piezoelectric load sensor. This apparatus is designed to perform tests at elevated temperatures. A new



flywheel tensile testing device was developed at the Institute of Mechanics and Engineering, Bordeaux, derived from the Charpy pendulum system; its working principle was well described by Froustey [115]. This dynamic device allows the test to be performed at medium strain rates in the range of  $\dot{\epsilon} \in [10^2, 10^3] \text{ s}^{-1}$ , which lies between the values obtained with servo-hydraulic machines and SHPB. The flywheel is a shock generator machine. The wheel has a large dimension (1 m diameter) and mass (620 kg) and is equipped with a hammer on its circumference, as shown in Figure 1.24.

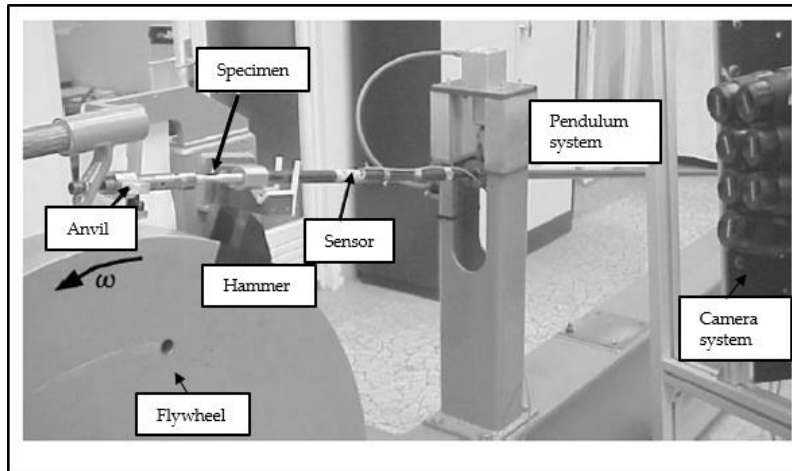


**Figure 1.24:** Flywheel and its long pendulum system (load sensor) [115]

The flywheel rotates freely until it reaches the selected speed, ranging from 1 to 40 m/s. The specimen is connected to the long Hopkinson bar pendulum system with an anvil fixed to one end. Once the required speed of the flywheel device is reached, the pendulum system is lowered. The hammer comes to strike the anvil, and the specimen is then strained, as shown in Figure 1.25.

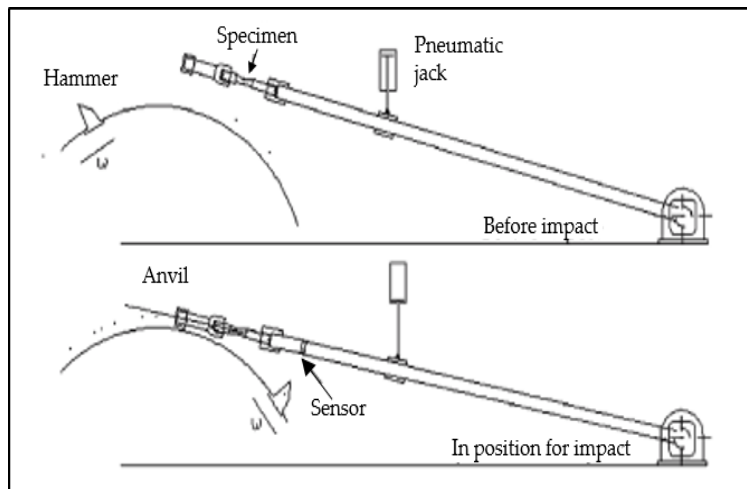


**Figure 1.25:** Schematic diagram of pendulum device before and after setting in position [115]

The load is measured by using Hopkinson bar techniques with eight strain gauges attached to the bar and mounted in a full Wheatstone bridge. The impact wave is completely transmitted from the specimen to the bar without any reflected pulse reloading. The time duration of the test is less than 1.3 ms. A high-speed camera is also attached to the flywheel device to measure the displacement field of the specimen. The strain rate achieved in this testing is around  $300 \text{ s}^{-1}$ . This technique is very reliable in that the loading mechanism is able to perform a constant rate of deformation.

In 2007, P. Viot [133,134] designed a new compression module on the same flywheel device as explained above in order to provide mechanical data under compression loading. The compression setup is shown in Figure 1.26. This device was specially designed to perform tests on foam material. The working principle is explained in [134]. When the required flywheel velocity is reached, the pneumatic jack is triggered, which pushes the anvil against the wheel. The anvil is then struck by the hammer (see point A, Figure 6). The impact rotates the lever and moves the bar BC (length of buckling bar); hence, the lower punch, moving upward vertically, compresses the specimen.

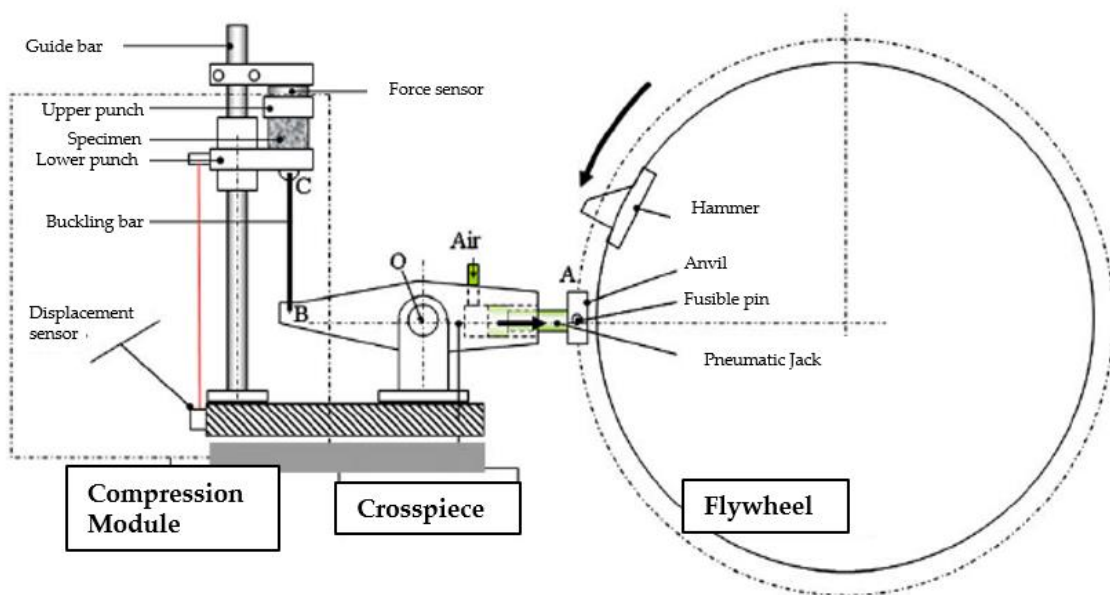


**Figure 1.26:** Scheme of compression module on flywheel [134].

The force sensor is placed above the upper punch to measure the compressive force. The deformation of the specimen is derived from a laser displacement sensor. This compressive module is designed to perform tests up to  $10^2 \text{ s}^{-1}$ . However, the flywheel compressive apparatus has some disadvantages. The loading method used in this setup generates a shock

wave, which has a significant effect on the load measurements. In addition, the compression module is not suitable for high-strength metals and alloys.

#### 1.4.2 Load measuring technique

Load measurement is always the main concern with an intermediate strain rate device due to the effects of inertia and high vibration on the load signals. Traditionally there are two types of load measurement techniques: Piezoelectric sensor (load cell) and Hopkinson bar (by strain gauging the bar).

Very few dynamic testing devices are equipped with the piezoelectric load cell. Although load cells have an adequate dynamic range [135], the load measurements are still problematic. Oscillation and vibration noise occur due to high inertia effects in the output signals of the load cell, and in addition, the impedance change (due to joints with different mechanical connections) between the components in the load train generates a wave reflection that causes further degradation of the load measurement.

Various techniques have been developed to improve the quality of load cell data. Xia et al. [136] performed the tests by customizing the existing load cell to investigate the vibration and oscillation effect, the tests were conducted by using a high speed servo hydraulic machine under three different strain-rates, 10, 100, and 200  $s^{-1}$  plotted in Figure 1.27, clearly supportive to the advantage of the customized sensor. Neither the customized sensor nor the commercial built-in load cell suffers from oscillation under 10  $s^{-1}$ . Moreover, their test results superimpose upon each other very well, indicating the good reliability of the two sensor systems under this strain-rate. However, when the strain-rate increases to 100  $s^{-1}$ , oscillation effect becomes evident for the commercial load cell. On the contrary, the customized load sensor is much more robust in the load measurement, which verifies the methodology and design procedure proposed in previous sections. As the strain-rate increases to 200  $s^{-1}$ , even the customized load sensor undergoes a small degree of system oscillation see Figure 1.27 (c). The authors are still working on how to improve the situation, but it seems that the current level of data quality is already acceptable for characterization use [112].

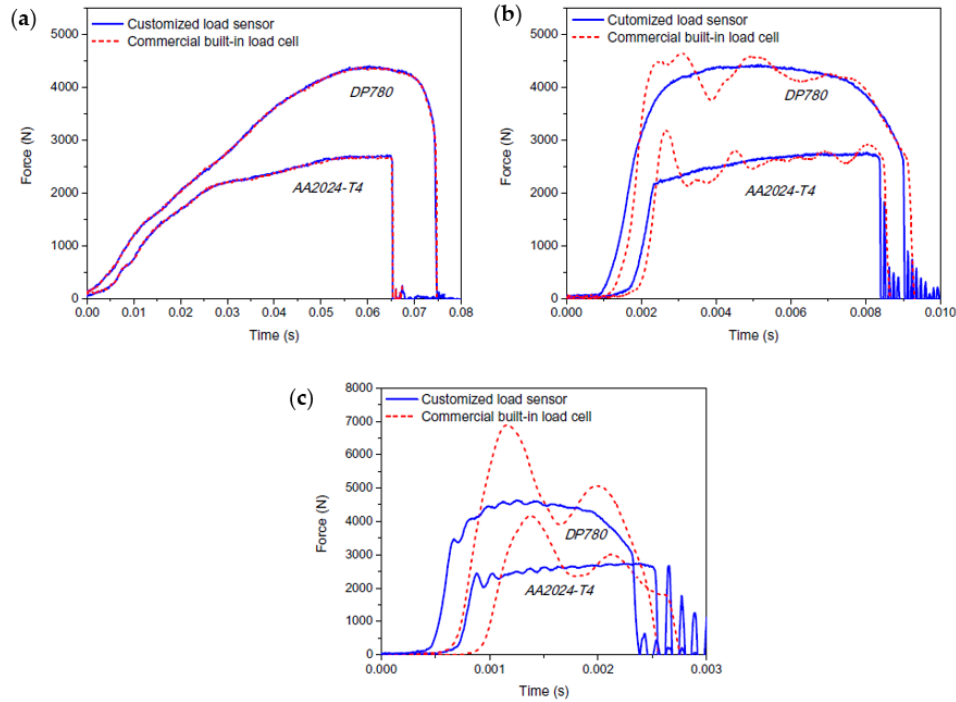


**Figure 1.27:** Load signals measured by the two different load sensors under (a) 10 s<sup>-1</sup>; (b) 100 s<sup>-1</sup>; and (c) 200 s<sup>-1</sup> (DP780: An advanced high strength steel and 2024-T4 an aluminium alloy) [136].

Several other techniques were also used to improve the load measurement data. For example, Groves et al. [137] used a laminate of impedance-mismatched materials to damp wave reflections on a drop-tower base, Kussmaul et al. [138] used plastic deformation of an aluminium damper to reduce load oscillations, and Follansbee' [139] used a ring of soft solder to lessen the shock (i.e., increase the loading wave rise time) of a hydraulic actuator contacting a compression fixture. The addition of damping material in the load train can lessen the strain rate, however, and may make sample deformation measurement more difficult. The influence of damping materials on the load cells is investigated at different strain rate levels. The experimental results show that different damping levels show unacceptable oscillations from measured force signals at intermediate strain rates in comparison to undamped testing. However, it is still difficult to draw conclusions about which types of damping materials are the most effective.

The conventional split Hopkinson bar (SHB) technique is an attractive alternative to the load sensor; it measures only the load transmitted through the specimen. The theory of stress wave propagation in a Hopkinson bar is well documented in the literature [97]. The

Hopkinson bar is defined as a perfectly elastic, homogeneous bar with a constant cross-section. A stress wave propagates in a Hopkinson bar as a one-dimensional elastic wave without attenuation or distortion. The specimen is attached to the bar on one end, and another end of the bar is free/fixed. The Hopkinson bar configuration is shown in Figure 1.28. When the specimen is loaded; the inertia of the bar provides a reaction to the specimen. When the specimen is compressed or elongated against the bar, the loading of the specimen is transmitted down the bar at the elastic wave velocity. At the other end of the bar, the elastic wave reflects back toward the loading end. The load in the bar is determined from a strain gage located close to the loading end. The strain gage is attached in the Wheatstone bridge, which leads to the separation of different stress waves (incident, reflected, and bending) [140]. The strain can then be translated into stress by Hooke's uniaxial law and thanks to the strain gauge calibration.

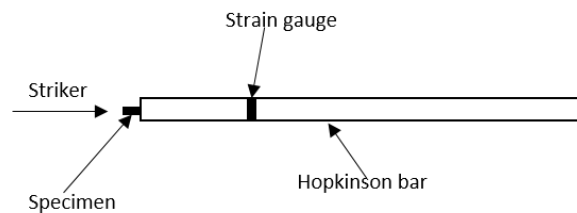


**Figure 1.28:** Configuration of split Hopkinson bar technique.

### 1.4.3 General Description of Intermediate Strain Rate Testing Device

There is no universal standard for the design of an intermediate strain rate device; researchers have designed and developed test devices based on necessity. In this section, the general requirements for an intermediate strain rate testing device are given.

- **Components and Basic Technical Assumption of Intermediate Strain Rate Testing Device**
  - The loading system must be capable of generating a dynamic load in traction, compression, and shear (e.g., high-speed servo-hydraulic actuator, drop weight tower, and flywheel device, as explained in Section 1.4.1).
  - The components of the testing machine, such as clamps, fasteners, fixtures, handles, adapters, and bar alignment system, are designed and assembled in such a way that the effect of inertia is minimised.

- The load applied to the specimen is usually measured by using a Hopkinson bar, which acts as a load sensor. The working principle of the load sensor is explained in Section 1.4.2. It is one of the most widely used load sensors in dynamic testing. The load is measured based on wave propagation theory. Hence, the dimension and selection of the material for the bar are very important.
- To measure the strain of the specimen, noncontact techniques are often used for dynamic measurement. There is a wide range of methods for displacement measurement, e.g., DIC, laser displacement sensor, and customized extensometer.
- A strain amplifier and an oscilloscope are necessary to magnify, transfer, and record the strain history of the bar.

The design of an intermediate strain rate testing apparatus must meet some basic assumptions to provide the expected experimental results:

- The loading system must generate constant intermediate impact speed without any vibration, noise, or oscillation.
- To obtain accurate load data, a different load measuring technique must be adopted, such as Hopkinson bar using wave separation, serpentine bar, long Hopkinson bar, and wave trap system. These techniques help to avoid reloading of the specimen and the inertial effect in the load measurement.
- The strain gauges are attached to the surface of the Hopkinson bar to measure the stress wave history; the position of the strain gauges must be defined properly. In many research articles, the strain gauges are usually connected in a Wheatstone bridge pattern. This pattern helps to eliminate unnecessary bending wave signals during load measurement.

#### **1.4.4 Experimental Test at High-temperature**

In recent years, there has been increasing interest in characterizing materials at low to high strain rates while varying temperature. Consequently, studying and modelling of the behaviour of materials under such conditions has been encouraged. In many applications, such as metal forming, machining, FSW, high-speed impact or high-energy metal deposition, and car accidents, materials are deformed at medium to high strain rates. This produces self-heating at high temperatures due to adiabatic processes. The stress–strain response in this case will be a balance between the effects of hardening (due to strain and strain rate) and

thermal relaxation. In other cases, the working temperature may be different from the ambient temperature. Therefore, the mechanical response of the material and the effect of strain rate must be investigated in the area of interest. At high temperatures, materials generally become much more ductile and can also exhibit microstructural changes due to recrystallization phenomena [141–143]. At low temperatures, however, the strength of the material generally increases, and the mechanical behaviour changes from ductile to less ductile. Figure 1.29 shows the flow stress–strain curves are influenced by the strain rate and temperature. From these considerations, it can be seen that temperature and strain rate are variables of fundamental importance in predicting the mechanical response of materials and, play an important role in many deformation processes. The development of a temperature experiment has allowed researchers to study the combined effects of strain rate and temperature on the mechanical and microstructure behaviour of materials.

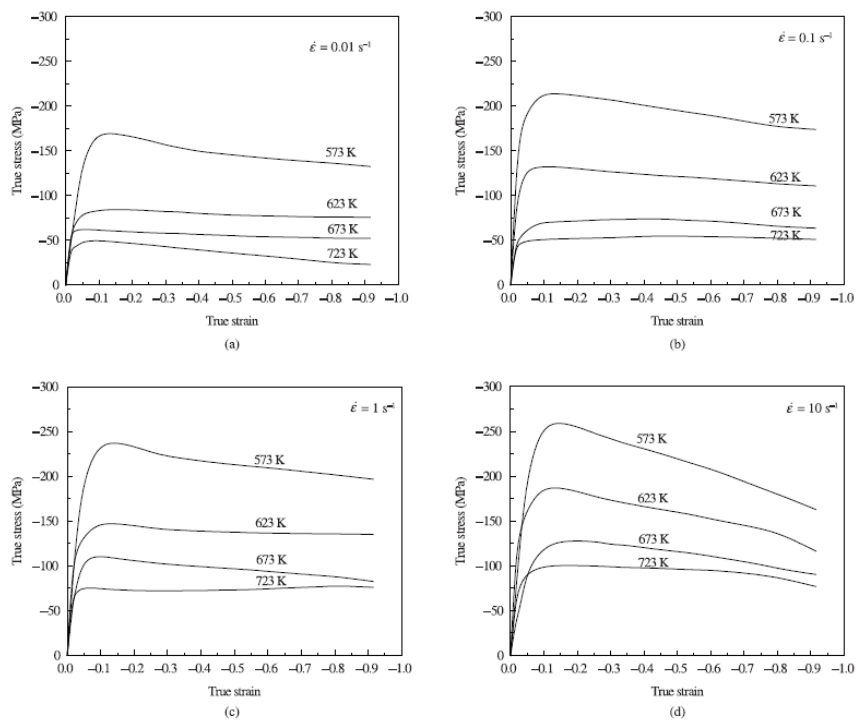


**Figure 1.29:** True stress–strain curves of 7075 aluminium alloy at different strain rates and temperatures (a)  $0.01 \text{ s}^{-1}$ , (b)  $0.1 \text{ s}^{-1}$ , (c)  $1 \text{ s}^{-1}$ , (d)  $10 \text{ s}^{-1}$ . [142]

The experimental data for high-temperature tests are mainly available for low strain rate and high strain rate testing devices. High-temperature intermediate strain rate experiments are not very popular. Some conventional test devices can provide high temperature test data,

but at a very limited temperature. Besides, it has been found that measuring the dynamic mechanical properties of materials at low temperatures using dynamic tests is not as difficult as that involving heating the specimen at high temperatures.

## 1.5 Conclusion

The understanding of the behaviour of materials in manufacturing processes is important for the researchers to develop a material model. For such material behaviour analysis, experimental tests provide a useful means to investigate the material behaviour in a realistic manner. In this chapter, at first, the material behaviour of AA7075-T6 alloy in different manufacturing processes, especially in machining and FSW, is discussed in detail. It is found that the evolution of the material microstructure occurs mainly due to shear deformation at the medium strain rate at high temperature. Second, existing classical models that are commonly used to simulate the manufacturing processes are discussed. This is followed by a discussion of shear testing techniques. Several representative shear specimens and the corresponding testing techniques were introduced. The advantages and disadvantages of each design were discussed. Finally, a review of the intermediate test setup is given.

The existing testing devices are mainly divided in terms of strain rate, ranging from low to high. They focus generally on the tensile and compressive behaviour of the material. However, for intermediate strain rate testing, very few testing devices are available. Moreover, there is no intermediate strain rate testing device available to study the pure shear behaviour. Shear test can reproduce the same response of the material behaviours encountered in processes such as machining and friction stir welding. Therefore, there is an increasing need to develop reliable techniques to determine the shear characteristics of materials at intermediate strain rates and to provide experimental data to improve material model. Moreover, there is not enough work done on high-temperature experimental testing. The development of a temperature experiment allowed researchers to study the combined effects of strain rate and temperature on the mechanical and microstructural behaviour of materials. Therefore, in the following chapters, the design and development of a new experimental test rig is discussed, including the validation of the device and preliminary tests are studied. Then, high temperature tests are performed at different strain rates to study the effect of temperature and strain rate on the material behaviour of AA7075-T6 alloy. Several



mechanical and microstructural investigations will be performed in order to clearly identify the mechanisms governing the evolution for plastic response covering a wide range of temperature strain and strain rates. Finally, the flow stress-strain curves obtained from experimental tests are compare and fitted with existing classical material behaviour models to generate baseline data to microstructural models.

Capítulos 2 y 3 sujetos a confidencialidad por el  
autor

# CHAPTER 4 ANALYZING AND MODELLING OF THE OUTPUTS

## 4.1 Introduction

It is now well established, that most materials show a significant change in mechanical response under different temperatures and strain rate. Material characterization involves not only the stress-strain response, but also the microstructural changes which materials undergo. The mathematical description of the relationship between the stresses, strains and temperature is referred to as the constitutive law or relationship. The basic problem is how to determine the constitutive relationship that best describes a particular material or class of materials. The most general form of a material constitutive equations should cover the description of material behavior under the wide range of strain rates that may be encountered. However, this can be extremely difficult, thus constitutive equations often cover only low to high strain rates, but nobody verifies these equations with the intermediate strain rate regime. It has been observed that for a number of materials different physical mechanisms are dominant at different strain rates. The importance of the effect of strain rate on metal material properties depends on the specific application conditions. In manufacturing processes such as machining and FSW where strain rate is in the range of  $10^2$ - $10^3$ s<sup>-1</sup>, it has been shown that this effect cannot be neglected. After development of the new intermediate strain rate torsion testing device, we are able to extract the stress strain curve at different strain rates and at different temperatures as explained in previous chapter. It allows us to study the material behavior in same conditions that the manufacturing process.

The most complex rate dependent models define the yield stress as a function of strain, strain rate, and temperature. These models are usually classified as phenomenological or physically based, depending on their basic assumptions. There are many constitutive equations that have been proposed by different investigators as explained in Chapter 1. These equations are very important because they are actually used in the computer codes to represent material behavior. In this chapter, we compared the experimental results obtained from new torsion test bench to the classic existing material models commonly used for constitutive behavior modelling of AA7075-T6 [62,171,172].The most widely used models today, for industrial applications (manufacturing process) are the Johnson-Cook (JC)[173], Khan–Huang–Liang (KHL)[40], Zerilli-Armstrong (ZA) models[56], etc. Detailed

descriptions of the Johnson Cook (JC), KHL model, Zerilli Armstrong (ZA) material models, are given in the chapter 1. The main advantage of choosing these models is that these constitutive equations mentioned above have a lesser number of parameters defining material properties. These parameters are differed based on the experimental conditions used to test the materials. The Johnson-Cook model has five parameters, the Zerilli-Armstrong has seven parameters and the KHL model can be used with six to seven parameters. The parameters are experimentally determined in tests performed over a different strain rates and temperatures. The procedures for obtaining parameters for different material models are presented in detail here. By comparison with the experimental results, the suitability of the three models is evaluated by calculating the correlation coefficient and average absolute relative error.

## 4.2 Material modelling (thermomechanical behaviour)

In this work, three constitutive models, such as JC, KHL and ZA, models are employed to predict the flow stress behavior of AA7075-T6 alloy. The work material flow stress relations in this study are obtained using hot torsion test using standard material evaluation procedure at two different strain rates and four different temperatures.

### 4.2.1 Johnson-Cook (JC) model

In the Johnson-Cook constitutive model as given in Equation. 4.1, the model describes the flow stress as the product of strain, strain rate and temperature effects, i.e. work hardening, strain-rate hardening, and thermal softening.

$$\sigma = (A + B\varepsilon^n) \left( 1 + C \ln\left(\frac{\dot{\varepsilon}}{\dot{\varepsilon}_0}\right) \right) \left( 1 - \left(\frac{T - T_0}{T_m - T_0}\right)^m \right) \quad (4.1)$$

The Johnson-Cook (JC) model assumes that the slope of the flow stress curve is independently affected by strain hardening, strain rate sensitivity and thermal softening behaviors. Each of these sets is represented by the brackets in the constitutive equation.

Various researchers have conducted slow to high speed tensile and compression tests to obtain the parameters A, B, C, n and m of the constitutive equation by fitting the experimental data. In this chapter we will obtain the parameters from hot torsion tests. Procedures to obtain the parameters are given in following section.

- **Procedures for obtaining parameters for J-C material model**

The JC model represents the flow stress with an Equation 4.2 of the form:

$$\sigma = (A + B\varepsilon^n) \left(1 + C \ln\left(\frac{\dot{\varepsilon}}{\dot{\varepsilon}_0}\right)\right) \left(1 - \left(\frac{T - T_0}{T_m - T_0}\right)^m\right) \quad (4.2)$$

where  $T_m$  is melting temperature and taken as the solidus temperature for an alloy and  $T_0$  is the initial room temperature. The values of A, B, C, n and m are determined from an empirical fit of flow stress data (as a function of strain, strain rate and temperature) to flow stress equation. The parameters in the J-C material model are sensitive to the computational algorithm used to calculate these parameters. In this chapter, procedures to obtain constants for JC model are proposed. The first step in this process is to determine the constants in the first set of brackets. A is yield stress and B and n represent the effects of strain hardening. At room temperature and for the strain rate of interest, the JC equation can be written as:

$$\sigma = (A + B\varepsilon^n) \quad (4.3)$$

$$\ln(\sigma - A) = \ln B + n * \ln \varepsilon \quad (4.4)$$

Then by substituting the flow stress and strain values at the reference deformation conditions into Equation 4.3, linear relation plot can be drawn between  $\ln(\sigma - A)$  and  $\ln(\varepsilon)$  and the first order regression model was used to fit the data points. The data distribution along the regression line helps us to predict the most suitable regression line equation. Which allows us to determine the constants B and n

Material constant C is calculated at the reference condition of temperature  $T_0$ , and for constant strain, constitutive equation can be written as equation 4.5:

$$\frac{\sigma}{(A + B\varepsilon^n)} - 1 = C * \ln\left(\frac{\dot{\varepsilon}}{\dot{\varepsilon}_0}\right) \quad (4.5)$$

The values of material constants A, B and n are implemented in the Equation 4.5 and then considering the flow stress values at different strain rates the plot has been drawn between  $\frac{\sigma}{(A+B\varepsilon^n)} \sim \ln\left(\frac{\dot{\varepsilon}}{\dot{\varepsilon}_0}\right)$ . Linear fitting is carried out using the first order regression model.

Determining the temperature sensitivity parameter m. By substituting the values of A, B and n into Equation 6 and fitting the data points using the first order regression model,

material constant  $m$  is determined. Same as constant  $C$  the optimize value of constant  $m$  is evaluated at a number of temperature values to fit in the best regression model. The parameter  $m$  can be determined at constant strain rate, constitutive equation can be written as:

$$\ln \left[ 1 - \frac{\sigma}{(A + B\varepsilon^n)} \right] = m * \ln \left( \frac{T - T_0}{T_m - T_0} \right) \quad (4.6)$$

After applying the least squares fit of the data, value of parameter  $m$  can be established.

#### 4.2.2 Khan–Huang–Liang (KHL) model

Khan, Huang and Liang (KHL model) developed model to study the thermal effect of coupling strain and strain rate. The equation to predict the flow stress using KHL model is given by equation 4.7

$$\sigma = \left[ A + B \left( 1 - \frac{\ln(\dot{\varepsilon}^*)}{\ln(D_{\max}^p)} \right)^{n_1} \varepsilon^{n_0} \right] \left( 1 - \left( \frac{T - T_0}{T_m - T_0} \right)^m \right) e^{C \ln \dot{\varepsilon}^*} \quad (4.7)$$

where  $\sigma$  is the true stress and  $\varepsilon$  is the true plastic strain.  $A$  is true stress as reference temperature. The melting, current and the reference temperatures are represented by  $T_m$ ,  $T$ ,  $T_0$  respectively and  $\frac{T-T_0}{T_m-T_0}$  is a homologues temperature.  $D_{\max}^p=10^6s^{-1}$  known as deformation rate (a constant used to non-dimensionalize the strain rate term).  $\dot{\varepsilon}^*$  is a dimensionless strain rate factor and it is equal to  $\frac{\dot{\varepsilon}}{\dot{\varepsilon}_0}$ ,  $\dot{\varepsilon}$  strain rate and  $\dot{\varepsilon}_0$  is reference strain rate.  $B$ ,  $C$ ,  $n_0$ ,  $n_1$  and  $m$  are material constants. The procedure to obtain those parameters are given below.

- **Procedures for obtaining parameters for KHL material model**

At reference temperature  $T_0$  and reference strain rate, the homologous temperature becomes zero and the  $\frac{\dot{\varepsilon}}{\dot{\varepsilon}_0} = 1$ . Therefore, the equation 4.7 reduces to the equation 4.8.

$$\sigma = (A + B\varepsilon^{n_0}) \quad (4.8)$$

$$\ln(\sigma - A) = \ln B + n_0 * \ln \varepsilon \quad (4.9)$$

$A$  is defined as yield stress at this condition.  $n_0$  is the slope of the line and  $B$  is obtained from intercept to the vertical axis.

In order to determine the value of C, it is considered that the strain at yield point is relatively small, so equation 4.7, at reference temperature, can be approximated as

$$\sigma \approx Ae^{C \ln \dot{\epsilon}^*} \quad (4.10)$$

$$\ln \frac{\sigma}{A} = C \ln(\dot{\epsilon}^*) \quad (4.11)$$

Therefore, C is determined from the slope of the line corresponding to equation. 4.11.

At reference temperature material constant  $n_1$  in equation 4.7 can be expressed as 4.12

$$n_1 = \frac{\ln \left( \frac{\frac{\sigma}{e^{C \ln \dot{\epsilon}^*}} - A}{B \dot{\epsilon}^{n_0}} \right)}{\ln \left( 1 - \frac{\ln(\dot{\epsilon}^*)}{\ln(D_{\max}^p)} \right)} \quad (4.12)$$

The value of  $n_1$  is calculated for different strain rates and temperatures. Similarly, m can be determined from equation 4.13

$$m = \frac{\ln \left( 1 - \frac{\sigma}{K} \right)}{\ln \left( \frac{T - T_0}{T_m - T_0} \right)} \quad (4.13)$$

where.

$$K = [A + B \left( 1 - \frac{\ln(\dot{\epsilon}^*)}{\ln(D_{\max}^p)} \right)^{n_1} \dot{\epsilon}^{n_0}] e^{C \ln \dot{\epsilon}^*} \quad (4.14)$$

The value of m is also obtained through constrained optimization.  $n_1$  and m was supposed to be taken as average values calculated from given by equations 4.12 and 4.13 but it affected the correlation. Hence to obtain better set of material constants  $n_1$  and m are calculated using unconstrained nonlinear optimization procedure for minimization of error.

### 4.2.3 Zerilli-Armstrong (ZA) model

This model is based on the framework of thermally activated dislocation motion. Zerilli and Armstrong proposed two microstructurally based constitutive equations that show a very good match with the experimental results. They analyzed the temperature and strain rate response of typical FCC and BCC metals and noticed the difference between these materials. The BCC metals are much higher temperature and strain rate sensitive than FCC metals. The detailed explanation of this material model is given in chapter 1 and followings are the expressions given for the BCC and FCC metals.

$$\sigma = C_0 + C_1 \exp(-C_3 + C_4 \ln \dot{\epsilon}) \text{ for BCC} \quad (4.15)$$

$$\sigma = C_0 + C_2 \epsilon^{\frac{1}{2}} \exp(-C_3 + C_4 \ln \dot{\epsilon}) \text{ for FCC} \quad (4.16)$$

In addition to thermal part of the equation, athermal component  $\sigma_G$  of flow stress is added and term which describes the flow stress dependent on grain size. Yield stress increases as the grain size decreases, and this dependence can be described by the Hall-Petch equation:

$$\sigma = \frac{k}{\sqrt{d}} \quad (4.17)$$

where  $d$  is grain diameter and  $k$  is constant. The overall expression now may be written as:

$$\sigma = \sigma_G + \sigma_{th} + \frac{k}{\sqrt{d}} \quad (4.18)$$

The separate plastic strain-hardening contribution to the flow stress of BCC metals may be evaluated from an assumed power law dependence on strain given by:

$$\sigma_G = C_5 \epsilon^n \quad (4.19)$$

Integral expressions now have following form:

$$\sigma = C_0 + C_1 \exp(-C_3 + C_4 \ln \dot{\epsilon}) + \frac{k}{\sqrt{d}} + \sigma_G \text{ for BCC} \quad (4.20)$$

$$\sigma = C_0 + C_2 \epsilon^{\frac{1}{2}} \exp(-C_3 + C_4 \ln \dot{\epsilon}) + \frac{k}{\sqrt{d}} + \sigma_G \text{ for FCC} \quad (4.21)$$

### Modified Zerilli – Armstrong model

The modified ZA constitutive model has been applied to estimate the flow stress behavior of the materials under high temperatures, which are listed as following equation 4.22. This material model is a strain, strain rate and temperature sensitive plasticity model [174,175], which is sometimes preferred in ordnance design calculations. Flow stress is expressed as follows:



$$\sigma = (C_1 + C_2 \varepsilon^n) \exp[-(C_3 + C_4 \varepsilon) T^* + (C_5 + C_6 T^*) \ln \dot{\varepsilon}^*] \quad (4.22)$$

- **Procedures for obtaining parameters for Zerilli-Armstrong material model**

For ZA constitutive material model have Integral expressions given in the equation 4.20 and 4.21. One can see that the plastic strain is uncoupled from strain rate and temperature for BCC metals. This is the main difference in constitutive equations for BCC and FCC metals.

The procedure for fitting constants, which are involved in constitutive relation for FCC metals, is described here in brief. However, in this study we selected the modified ZA model given in equation 4.22. First two terms are independent of temperature, strain rate and strain. The first is attributed to the effect of the initial dislocation density and the second is due to hardening effect of grain boundaries. In this work they are combined in one athermal material constant, so that in total six material constant need to be determined  $C_1$ ,  $C_2$ ,  $C_3$ ,  $C_4$ ,  $C_5$ ,  $C_6$ , and  $n$ .

By considering the variation of yield stress with strain rate at zero plastic strain the final term can be omitted, leaving an equation for yield stress:

$$\sigma_y = C_1 + C_1 \exp(-C_3 + C_4 \ln \dot{\varepsilon}) \quad (4.23)$$

Now involving the four constants,  $C_0$ ,  $C_1$ ,  $C_3$ ,  $C_4$ . By fitting the above equation to the experimental data for yield stress over a wide range of strain rate and for different temperature, optimum values for these constants can be obtained. Plotting value of yield stress versus strain rate on semi log plot for different temperatures, one can find values for above constants.

The remaining two material constants  $C_5$  and  $n$ , can be derived by assuming isothermal conditions during test at different strain rates and by fitting the relation

$$\sigma = \sigma_y + C_5 \varepsilon^n \quad (4.24)$$

A similar procedure can be applied for determination of constants which are involved in the constitutive formulation for FCC metals.

### 4.3 Results and discussion

#### 4.3.1 Experimental data

Figure 4.1 shows the classical stress-strain curves at different temperature and strain rates for AA7075-T6. The effect of strain rate and temperature are clearly observed and commented in chapter 3. The flow stress between the strain rate and temperature are distinct and significant. This set of data has been used for derivation of parameter for temperature and strain rate dependent material model. In this section, the parameters for J-C model, KHL model, Z-A model, etc have been derived for this experimental set of data.

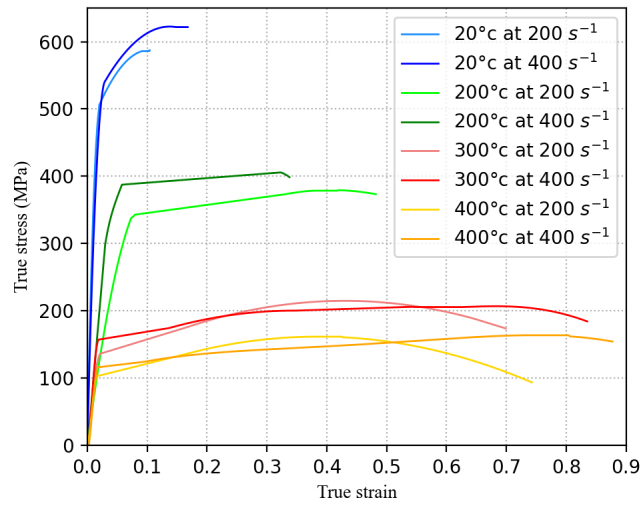


**Figure 4.1:** True stress vs true strain curves from hot torsion tests at different temperatures and strain rates

#### 4.3.2 Derivation of JC model parameters for AA7075-T6

On the basis of procedure described in 4.2.1.1 for determination of J-C material model parameters, the following form of J-C model was chosen to fit the experimental data.

$$\sigma = (A + B\varepsilon^n) \left( 1 + C \ln\left(\frac{\dot{\varepsilon}}{\dot{\varepsilon}_0}\right) \right) \left( 1 - \left( \frac{T - T_0}{T_m - T_0} \right)^m \right) \quad (4.25)$$

At reference temperature  $T_0=493\text{K}$  ( $200^\circ\text{C}$ ) and at given temperature  $T=493\text{K}$ . for reference strain rate  $\dot{\varepsilon}_0=200\text{s}^{-1}$ , the above equation can be written as:

$$\sigma = (A + B\varepsilon^n) \quad (4.26)$$

$$\ln(\sigma - A) = \ln B + n * \ln \varepsilon \quad (4.27)$$

The stress at zero plastic strain was obtained from the experimental data and found to be  $A=341.43\text{ MPa}$ . The quantity  $\ln(\sigma - A)$  was calculated and plotted versus plastic strain  $\ln$

( $\epsilon$ ) as shown in Figure 4.2. B and n were obtained using least squares fit of data to a  $B=106.43\text{MPa}$  and  $n= 0.64$ .

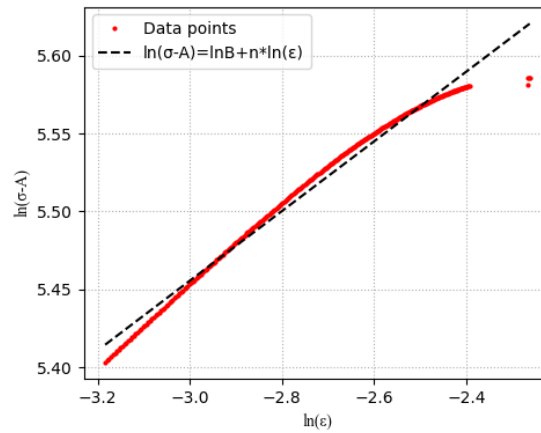


**Figure 4.2:**Plot shows the relation between  $\ln(\sigma - A)$  and  $\ln(\epsilon)$  under reference conditions. B and n values are determined

The parameter C was obtained from  $\sigma$ -  $\dot{\epsilon}$  data. At reference temperature and for constant strain, constitutive equation can be written as:

$$\frac{\sigma}{(A + B\epsilon^n)} - 1 = C * \ln\left(\frac{\dot{\epsilon}}{\dot{\epsilon}_0}\right) \quad (4.28)$$

where  $(A + B\epsilon^n)$  is the stress at strain rate of interest  $\dot{\epsilon}^* = \frac{\dot{\epsilon}}{\dot{\epsilon}_0} = 1$ . For constant strain, value of a  $(A + B\epsilon^n)$  can be calculated, and  $\frac{\sigma}{(A + B\epsilon^n)} - 1$  be plotted versus  $\ln\left(\frac{\dot{\epsilon}}{\dot{\epsilon}_0}\right)$  (Fig. 4.3). A least square fit to the data gives, as an average value,  $C=0.008$

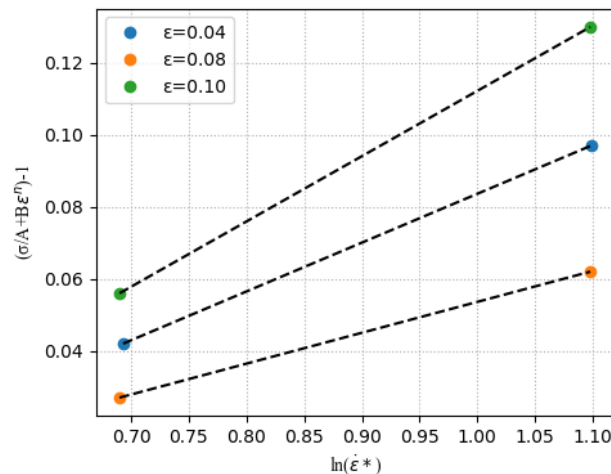


**Figure 4.3:**Shows the regression line fits for different strain rate values which determines the constant C

The parameter  $m$  was determined from the stress-temperature  $T^* = \frac{T-T_0}{T_m-T_0}$  response of the alloy. At constant strain and strain rate, constitutive equation can be written as:

$$\ln \left[ 1 - \frac{\sigma}{(A + B\varepsilon^n)} \right] = m * \ln \left( \frac{T - T_0}{T_m - T_0} \right) \quad (4.29)$$

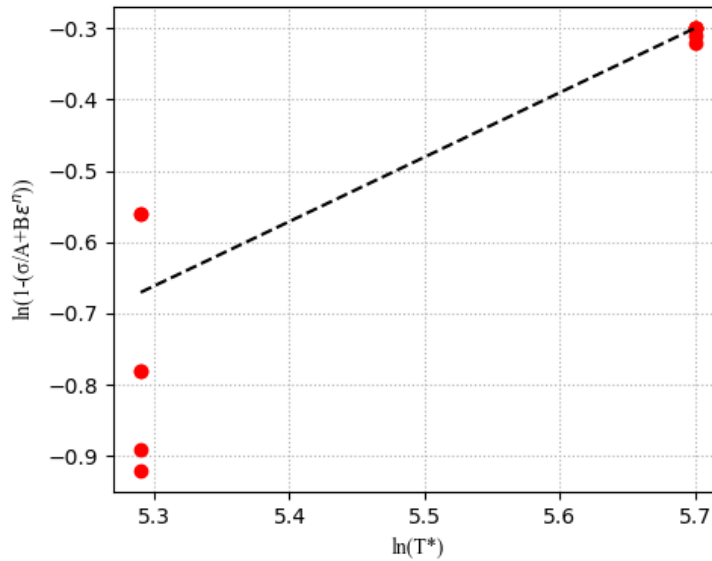


**Figure 4.4:**Plot shows the regression line fitted to calculate the constant  $m$  at only 2 temperature values

For constant strain and constant strain rate, value of  $\frac{\sigma}{(A+B\varepsilon^n)}$  can be calculated, and data plotted two different temperatures (300°C and 400°C) Figure.4.4. After applying least squares fit of the data, average value of parameter  $m$  was found as  $m = 0.68-0.903$ . Final material constants obtained for the JC model are listed in Table 4.1.

**Table 4.1:**Material constants obtained for the JC model

Parameter	A	B	C	n	m
Values	341.43	106.16	0.008	0.64	0.903

Comparisons of experimental stress-strain curves and Johnson-Cook model fit are given on the following graphs. It is noticed that though JC model gives a good estimate of linear dependence of fit between experimental and predicted flow stresses. However, in Figure 4.5, it is observed that predicted flow stress slightly attains the steady stress at a strain of 0.15 above 300°C. whereas experimental flow stress curve shows the broad peak at strain of 0.35 and the decrease in nature.

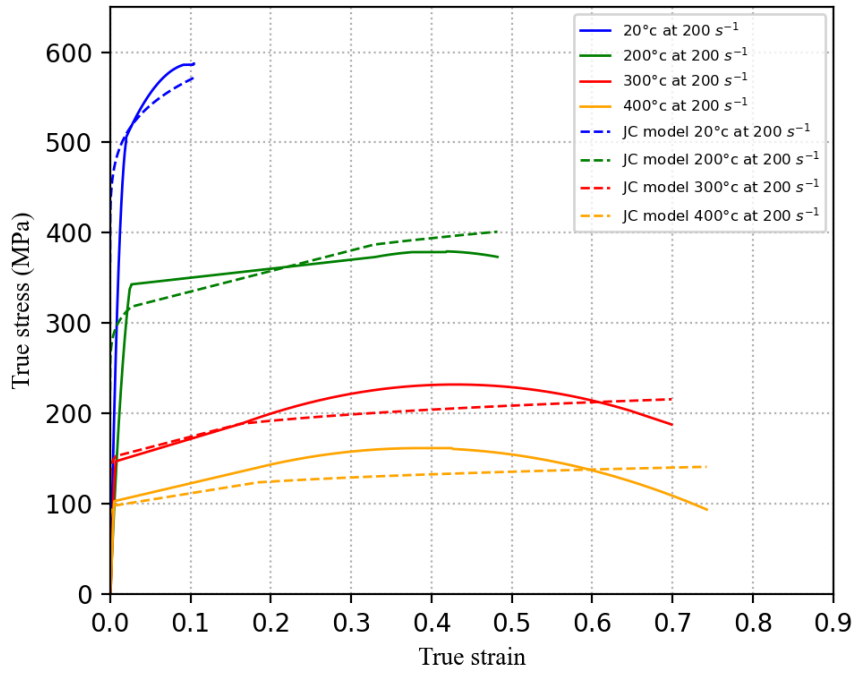


**Figure 4.5:**Constitutive model (JC model) prediction comparison at different temperatures and strain rate of  $200s^{-1}$

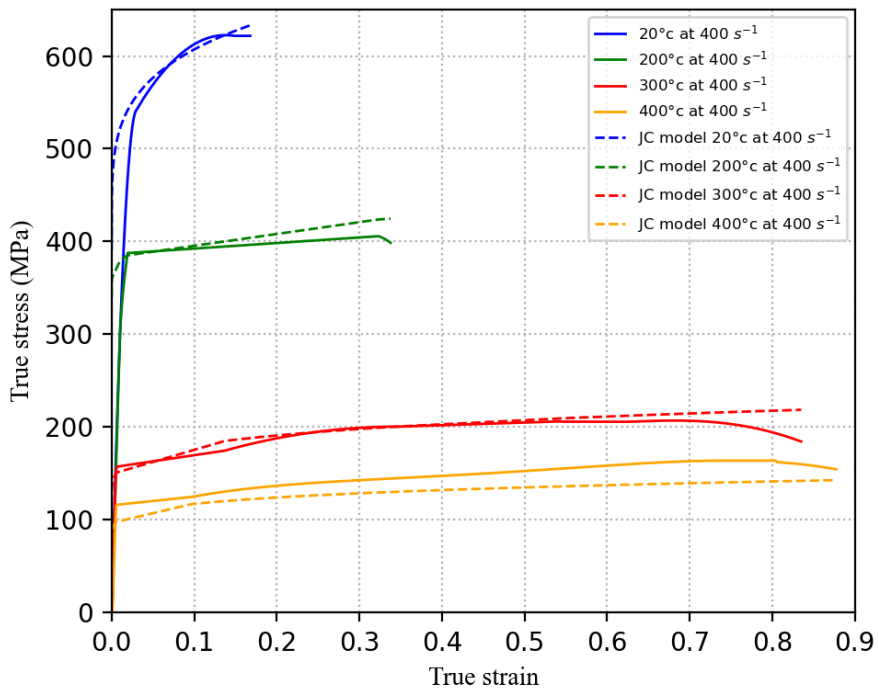


**Figure 4.6:**Constitutive model (JC model) prediction comparison at different temperatures and strain rate of  $400s^{-1}$

However, at strain rate of  $400\text{s}^{-1}$  (see Figure 4.6), the predicated stress level seems to be lower at higher temperature ( $400^\circ\text{C}$ ). It is generally accepted that at large strains most metallic material tends to approach a finite saturation stress or approach a small hardening rate at large strain and we observed that such behavior is lacking in the JC model. However, the main advantage of JC model over other physical based model is in the number of materials for which parameters are known. As the same time the advantages of the physical based model over JC model is in the fact that it is based on physical processes taking place in deforming material and therefore can more accurately represent the behavior. Hence in next section we discussed about the physical based models.

### 4.3.3 Derivation of KHL model parameters for AA7075-T6

It is found from the experimental results that the initial yield stresses of AA7075-T6 are only dependent on temperature but not much on strain-rate, which is commonly verified for aluminum alloys. The KHL model takes into account the effect of temperature and strain rate given by Equation 4.30.

$$\sigma = \left[ A + B \left( 1 - \frac{\ln(\dot{\epsilon}^*)}{\ln(D_{\max}^p)} \right)^{n_1} \epsilon^{n_0} \right] \left( 1 - \left( \frac{T - T_0}{T_m - T_0} \right)^m \right) e^{C \ln \dot{\epsilon}^*} \quad (4.30)$$

Where  $T_0 = 473\text{K}$  the reference temperature,  $B$ ,  $n_1$ ,  $n_0$ ,  $m$ ,  $C$  are fitting material constants. At  $T = 473\text{K}$  and  $\dot{\epsilon} = 200 \text{ s}^{-1}$  and  $D_{\max}^p$  is the maximum strain rate (fixed to  $10^6 \text{ s}^{-1}$ ).

$$\sigma = (A + B\epsilon^{n_0}) \quad (4.31)$$

$$\ln(\sigma - A) = \ln B + n_0 * \ln \epsilon \quad (4.32)$$

Similar to the JC model, the stress at zero plastic strain was obtained from the experimental data and found to be  $A=341.43 \text{ MPa}$  at reference temperature and reference strain rate of  $200\text{s}^{-1}$ . The quantity  $\ln(\sigma-A)$  was calculated and plotted versus plastic strain  $\ln(\epsilon)$  as shown in figure 4.7.  $B$  and  $n$  were obtained using least squares fit of data where  $B=106.\text{MPa}$  as a intercept and  $n_0= 0.8$  as a slope of the line.

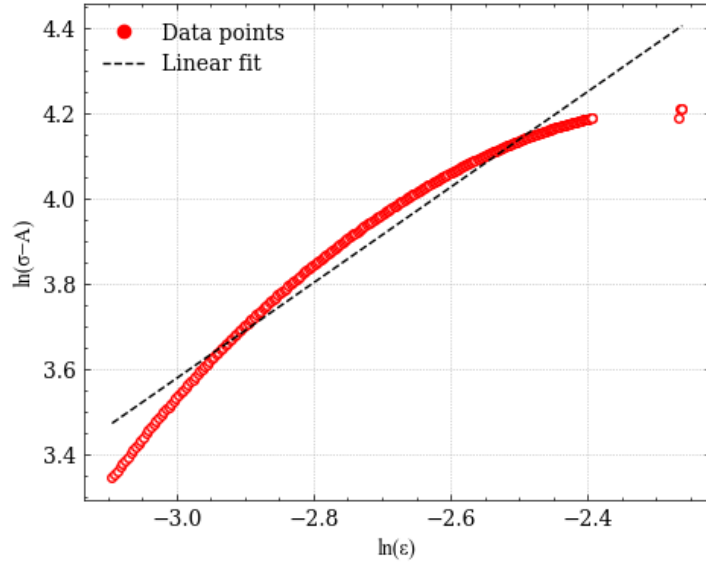


**Figure 4.7:**Plot shows the relation between  $\ln(\sigma - A)$  and  $\ln(\epsilon)$  under reference conditions.  $B$  and  $n_0$  values are determined

Now, at very small strain value, the  $C$  can be defined by using following equation 4.34. The slope of the line  $\ln\frac{\sigma}{A}$  and  $\ln(\dot{\epsilon}^*)$  is the value of  $C$  and it is defined at different strain rate and reference temperature of  $T=473K$ .

$$\sigma \approx Ae^{C \ln \dot{\epsilon}^*} \tag{4.34}$$

$$\ln \frac{\sigma}{A} = C \ln(\dot{\epsilon}^*) \tag{4.35}$$

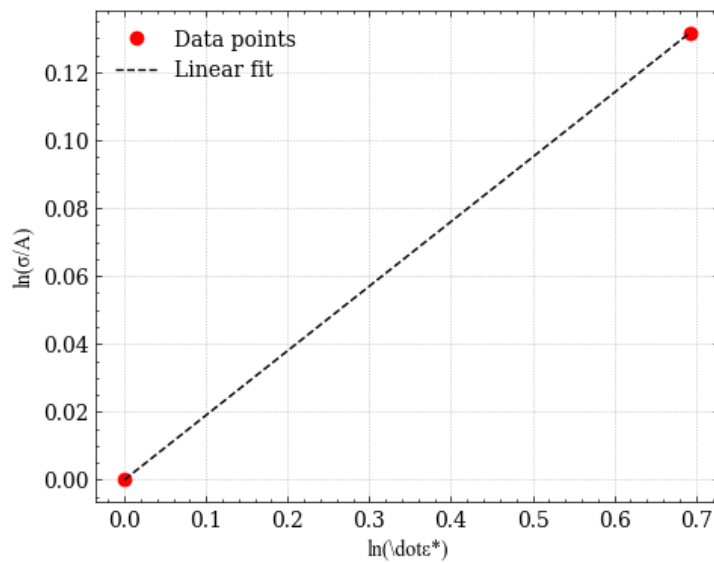


**Figure 4.8:**Shows the regression line fits for two different strain rate values which determines the constant  $C$

As shown in figure 4.8 the slope of the line is defined as the C and is determined to be 0.18. Similarly, constant  $n_1$  is evaluated at reference temperature. The equation 4.30 can be expressed as equation 4.36.

$$n_1 = \frac{\ln\left(\frac{\frac{\sigma}{e^{C \ln \varepsilon^*}} - A}{B \varepsilon^{n_0}}\right)}{\ln\left(1 - \frac{\ln(\varepsilon^*)}{\ln(D_{\max}^p)}\right)} \quad (4.36)$$

$n_1$  is the slope of the equation 4.36 and it is defined as  $n_1 = 2.52$ . Whereas m value is determined by substituting all the constants which is determined previously and by taking the slope of the line from the equation 4.37 at different temperature, the m value is determined. Whereas k is determined by equation 4.38.

$$m = \frac{\ln\left(1 - \frac{\sigma}{K}\right)}{\ln\left(\frac{T - T_0}{T_m - T_0}\right)} \quad (4.37)$$

$$K = \left[A + B \left(1 - \frac{\ln(\varepsilon^*)}{\ln(D_{\max}^p)}\right)^{n_1} \varepsilon^{n_0}\right] e^{C \ln \varepsilon^*} \quad (4.38)$$

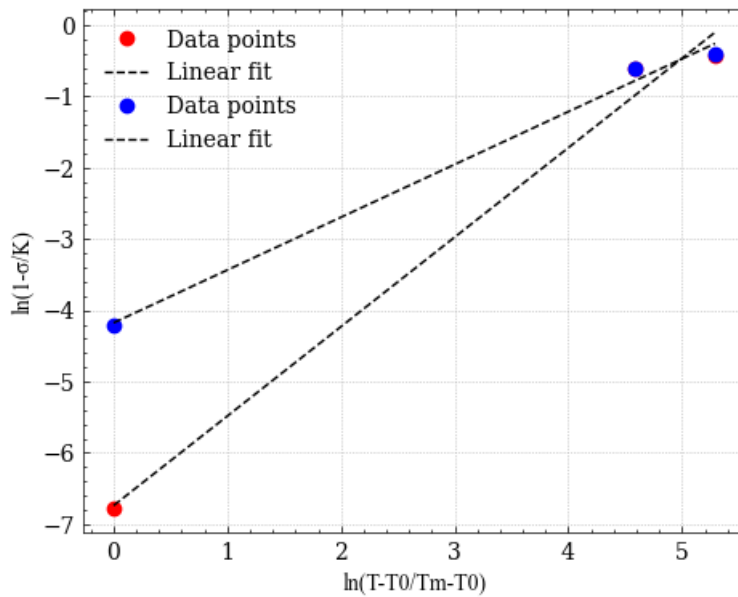


**Figure 4.9:** Plot show the relation between  $\ln\left(1 - \frac{\sigma}{K}\right)$  vs  $\ln\left(1 - \frac{\sigma}{K}\right)$  under reference condition and m value is determined

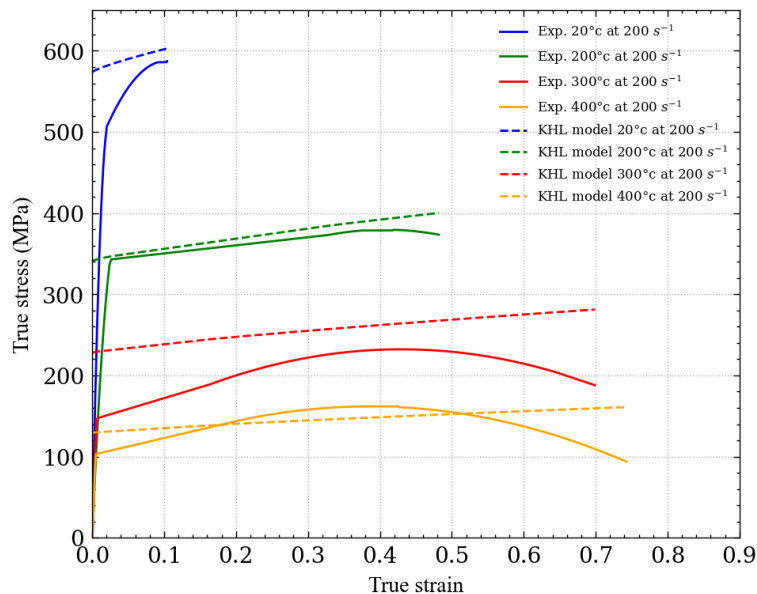


Figure 4.9 is drawn at different temperature for two different strain rates the average slope of the lines is nothing but the value of  $m$ , and it is  $m= 1.2$ . Finally, all the material constant for KHL model are listed in Table 4.2.

**Table 4.2:** Constants for KHL model

Parameter	A	B	$n_0$	$n_1$	C	$m$
Values	341.43	106.3	0.58	2.52	0.18	1.2

Comparisons of the experimental stress-strain curves and the KHL model fit are given in Figures 4.10 and 4.11. The experimental data are not tracked by the predicted flow stress value of the constitutive equation. It can be seen that the predicted flow curve has a slight divergence from the experimental curve. Also, the level of flow stress at each temperature is not the same. For example, at 300°C, the predicted flow stress curve is completely offset from the experimental curve. Furthermore, the linear behaviour of the flow stress curve is observed without evidence of any softening effect and thermal behaviour of material. Therefore, an improvement of the KHL model is needed to study the accurate thermomechanical behaviour of the material.



**Figure 4.10:** Constitutive model (KHL model) prediction comparison at different temperatures and strain rate of  $200\text{s}^{-1}$

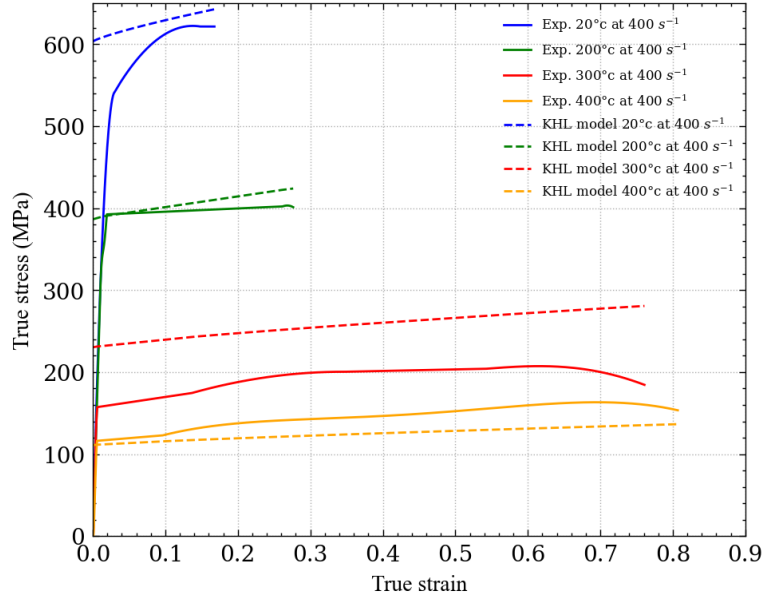


**Figure 4.11:** Constitutive model (KHL model) prediction comparison at different temperatures and strain rate of  $400\text{s}^{-1}$

#### 4.3.4 Derivation of modified ZA model parameters for AA7075-T6

As mentioned before, to consider the interaction between the effect of the strain rate and temperature, a modified ZA model is selected, it is a physical base model, which is expressed below.

$$\sigma = (C_1 + C_2 \varepsilon^n) \exp[-(C_3 + C_4 \varepsilon) T^* + (C_5 + C_6 T^*) \ln \dot{\varepsilon}^*] \quad (4.39)$$

The meanings of  $\sigma$ ,  $\varepsilon$ , and  $\dot{\varepsilon}^*$  are the same as those in the JC model. The difference is that the expression of  $T^*$  is  $T^* = T - T_0$  in this model. In this case, reference temperature and strain rates are  $T_0 = 493\text{K}$  and  $\dot{\varepsilon}_0 = 200\text{s}^{-1}$  respectively.

Meanwhile,  $C_1$ ,  $C_2$ ,  $C_3$ ,  $C_4$ ,  $C_5$ ,  $C_6$ , and  $n$  are material constants.  $C_1$  means the yield stress at the reference strain rate and reference temperature, which equals to 341.43. MPa, as obtained in the JC model. Like the JC model, the data under specific conditions was chosen to eliminate terms in the model and the constants could be obtained from the fitting curve, respectively.

First, taking the natural logarithm on both sides of Equation 39 into account, the equation could be represented below.

$$\ln\sigma = \ln(C_1+C_2\varepsilon^n) - (C_3 + C_4\varepsilon)T^* + (C_5 + C_6T^*)\ln\varepsilon^* \quad (4.40)$$

When the strain rate equals the reference strain rate, means  $\varepsilon^*=1$  Equation 4.40 is simplified below.

$$\ln\sigma = \ln(C_1+C_2\varepsilon^n) - (C_3 + C_4\varepsilon)T^* \quad (4.41)$$

At different temperatures level (200,300 and 400°C) and at different strains (0.05, 0.1, 0.15, 0.2, 0.25, 0.3, 0.35 and 0.4), the corresponding stress values were chosen to describe the relation between  $\ln\sigma$  and  $T^*$ .

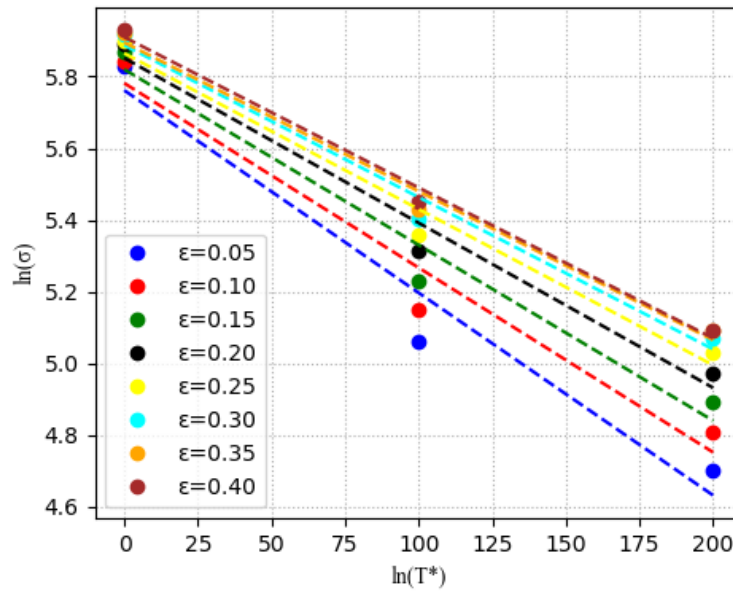


**Figure 4.12:**The relations between  $\ln\sigma$  and  $T^*$  for different strains.

As shown in Figure 4.12, the slope  $S_1$  and intercept  $I_1$  at different strains could be obtained, which are  $-(C_3 + C_4\varepsilon)$  and  $\ln(C_1 + C_2\varepsilon^n)$ , respectively. Equations 4.42 and Equation 4.43 are shown below.

$$I_1 = \ln(C_1+C_2\varepsilon^n) \quad (4.42)$$

$$S_1 = (C_3 + C_4\varepsilon) \quad (4.43)$$

According to the two equations above, 8 couples of  $S_1$  and  $I_1$  are calculated from Figure 4.12, as shown in Table 4.3.

Table 4.3: The value of  $S_1$  and  $I_1$  for 15 strains.

Strain	$I_1$	$S_1$
0.05	5.76167	-0.0057
0.1	5.78167	-0.0052
0.15	5.82	-0.0049
0.2	5.85167	-0.0046
0.25	5.865	-0.0044
0.3	5.88733	-0.0042
0.35	5.895	-0.0042
0.4	5.91	-0.0042

By rearranging Equation 4.42, Equation 4.44 can be obtained. Afterward, the relation between  $\ln(\exp I_1 - C_1)$  and  $\ln \epsilon$  could be established, according to the values of  $I_1$  under different strains.

$$\ln(\exp I_1 - C_1) = \ln C_2 + n \ln \epsilon \tag{4.44}$$

As shown in Figure 4.13,  $\ln C_2$  is the slope of the curve and  $n$  is the intercept. By calculation, the values of  $C_2$  and  $n$  are 174.30 MPa and 0.90, respectively.

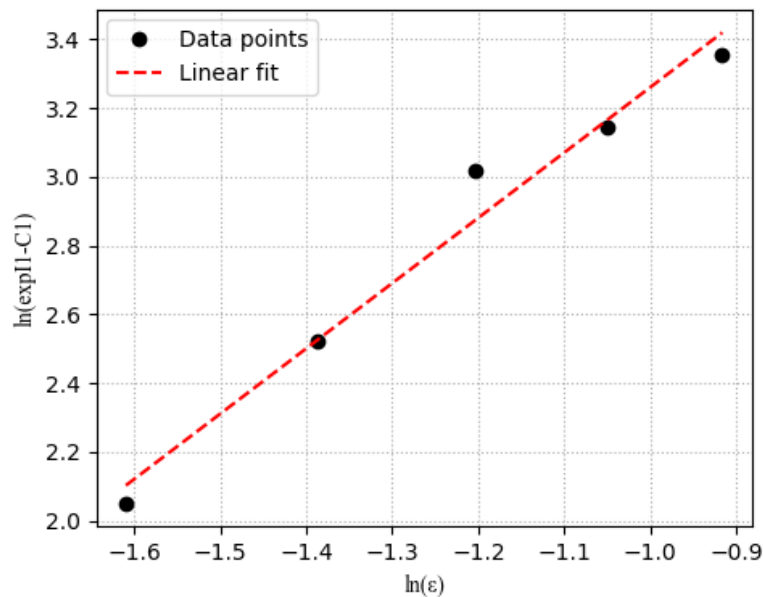
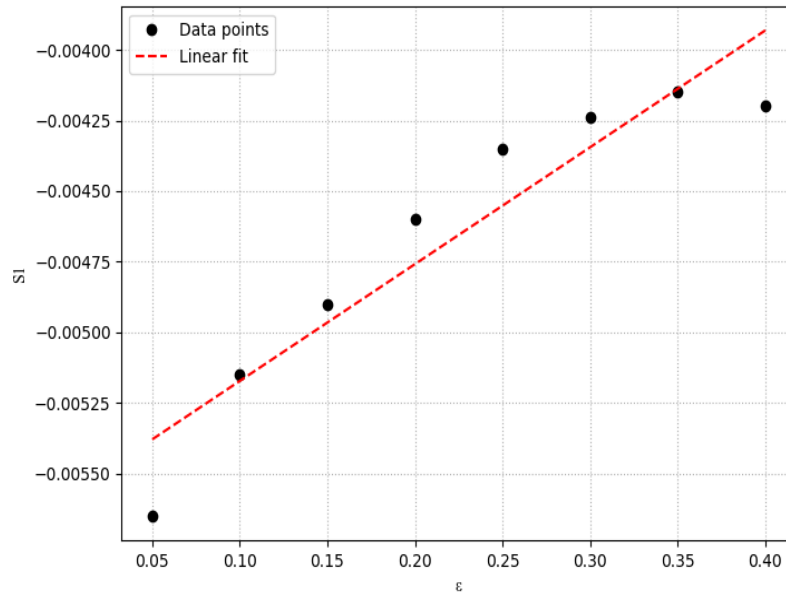


Figure 4.13: The relation between  $\ln(\exp I_1 - C_1)$  and  $\ln \epsilon$ .

Moreover, the curve of  $S_1$  vs.  $\epsilon$  is also plotted (shown in Figure 4.14).  $C_3$  and  $C_4$  are the values of intercept and slope in the fitting line separately, whose values are 0.005 and -0.0041, respectively.



**Figure 4.14:** The relation between  $S_1$  and  $\epsilon$ .

As it can be seen from equation 4.45, the slope  $S_2$  of the  $\ln\sigma$ - $\ln \epsilon^*$  curve plot is the value of  $(C_5 + C_6 T^*) \ln \epsilon^*$ . Therefore, a group of slope values under different strains and different temperatures were generated. There are different values of  $S_2$  which can be obtained under specific strain while the slope  $S_2$  can be expressed as:

$$S_2 = C_5 + C_6 T^* \tag{4.45}$$

Thus,  $C_5$  and  $C_6$  can be generated easily from the slope and intercept of the plot of  $S_2$  and  $T^*$ , which can be observed from Figure 4.15. Therefore, from the figure 4.15 the optimized values of  $C_5$  and  $C_6$  are 0.098 and -0.00108, respectively.

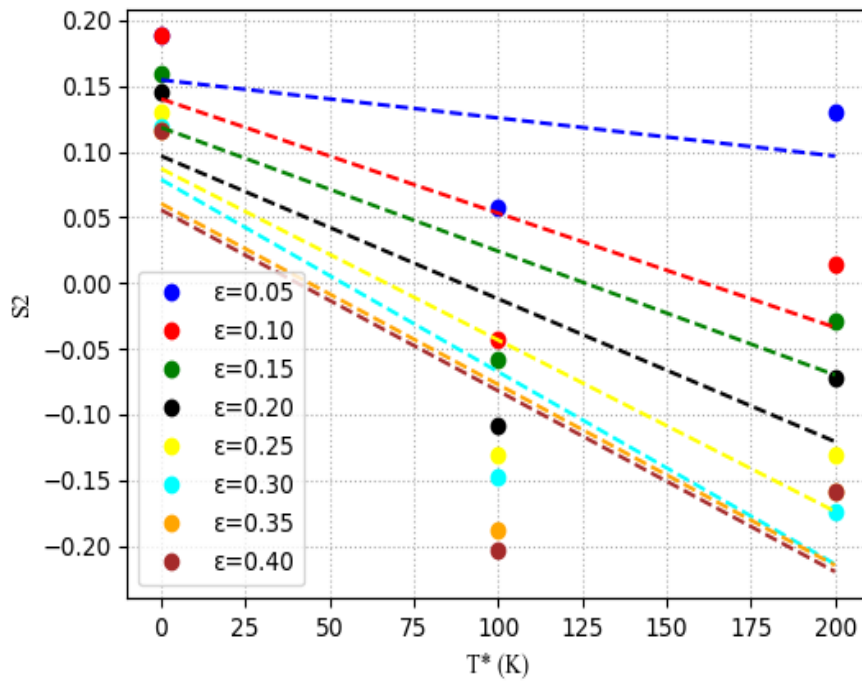


**Figure 4.15:** Relationship between S2 and T\* at different strains.

All of the constants of the modified ZA model could be obtained as shown in Table 4.4.

**Table 4.4:** Material constants for modified ZA constitutive model.

Parameter	C <sub>1</sub>	C <sub>2</sub>	C <sub>3</sub>	C <sub>4</sub>	C <sub>5</sub>	C <sub>6</sub>	n
Values	341.43	174.3	0.005	-0.0041	0.098	-0.0011	0.90

Comparisons of experimental stress-strain curves and modified ZA model fit are given on the following graphs. The experimental data shows the good agreement with the predicted flow stress value of the constitutive equation (ZA model). However, at higher temperature the experimental flow has higher values than in predicted curves as shown in Figure 4.16 and 4.17. The predicted flow stress curves show increasing linear trend while in the experimental flow stress curve, at a certain strain level, the stress values increase and there is a sudden drop and undergo softening. Therefore, it is concluded that for the given experimental results, the ZA model needs to be improved to investigate the softening mechanism that occurred during the tests.

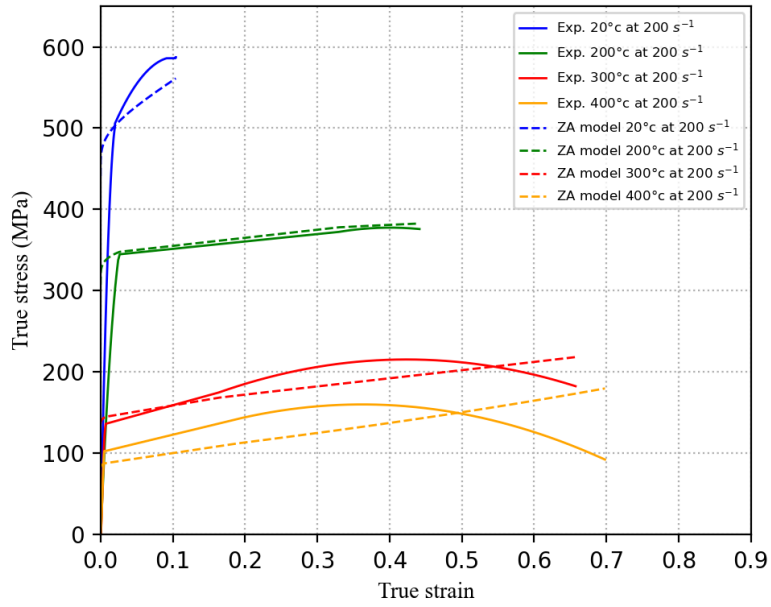


**Figure 4.16:** Constitutive model (modified ZA model) prediction comparison at different temperatures and strain rate of  $200s^{-1}$

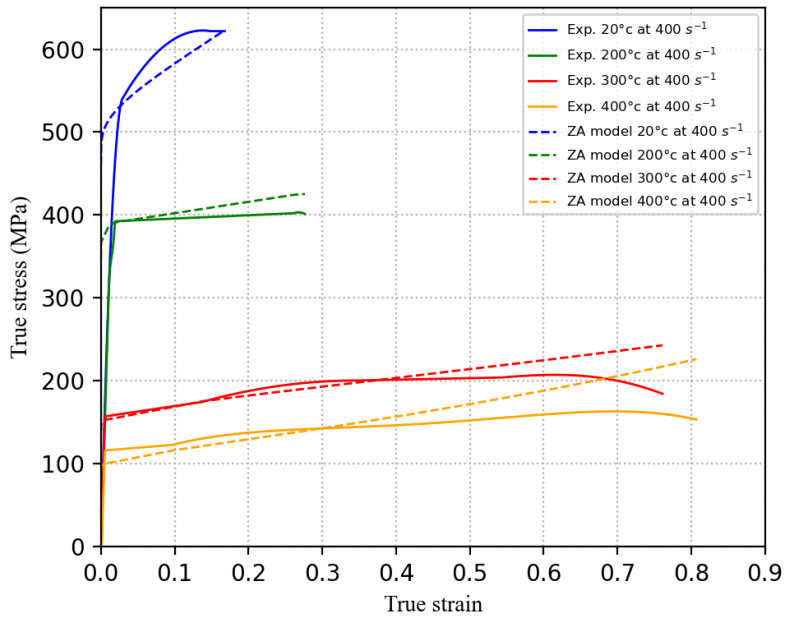


**Figure 4.17:** Constitutive model (modified ZA model) prediction comparison at different temperatures and strain rate of  $400s^{-1}$

#### 4.4 Accuracy Analysis

The flow stress prediction capability of formulated constitutive models was compared in terms of correlation coefficient (R) and average absolute relative (AARE) error between experimental and predicted flow stress results. The mathematical forms formulated for this purpose are presented in equation 4.46 (JC model), equation 4.47 (KHL model), equation 4.48 (ZA model).

$$\sigma = (341.43 + 106.30\varepsilon^{0.64}) \left( 1 + 0.008 * \ln\left(\frac{\dot{\varepsilon}}{\dot{\varepsilon}_0}\right) \right) \left( 1 - \left(\frac{T - T_0}{T_m - T_0}\right)^{0.903} \right) \quad (4.46)$$

$$\sigma = \left[ 341.43 + 106.30 \left( 1 - \frac{\ln(\dot{\varepsilon}^*)}{\ln(D_{max}^p)} \right)^{2.52} \varepsilon^{0.58} \right] \left( 1 - \left(\frac{T - T_0}{T_m - T_0}\right)^{1.2} \right) e^{0.18 * \ln \dot{\varepsilon}^*} \quad (4.47)$$

$$\sigma = (341.43 + 174.3\varepsilon^{0.9}) \exp[-(0.005 - 0.0041\varepsilon)T * +(0.098 - 0.0011T * \ln \dot{\varepsilon}^*)] \quad (4.48)$$

Information about the strength of linear relationship between the predicted values and experimental values is provided by the correlation coefficient (R) and AARE. AARE and R can be expressed as the following:

$$AARE(\%) = \frac{1}{N} \sum_{i=1}^N \left| \frac{E_i - P_i}{E_i} \right| * 100 \quad (4.49)$$

$$R = \frac{\sum_{i=1}^N (E_i - \bar{E})(P_i - \bar{P})}{\sqrt{\sum_{i=1}^N (E_i - \bar{E})^2 \sum_{i=1}^N (P_i - \bar{P})^2}} \quad (4.50)$$

where E and P are the experimental and predicted flow stresses (MPa), respectively.  $\bar{E}$  and  $\bar{P}$  are the mean values of E and P, respectively. N is the total number of data used. The comparisons between the predicted data and the experimental flow stresses by the three developed models are presented in Figure 4.18.



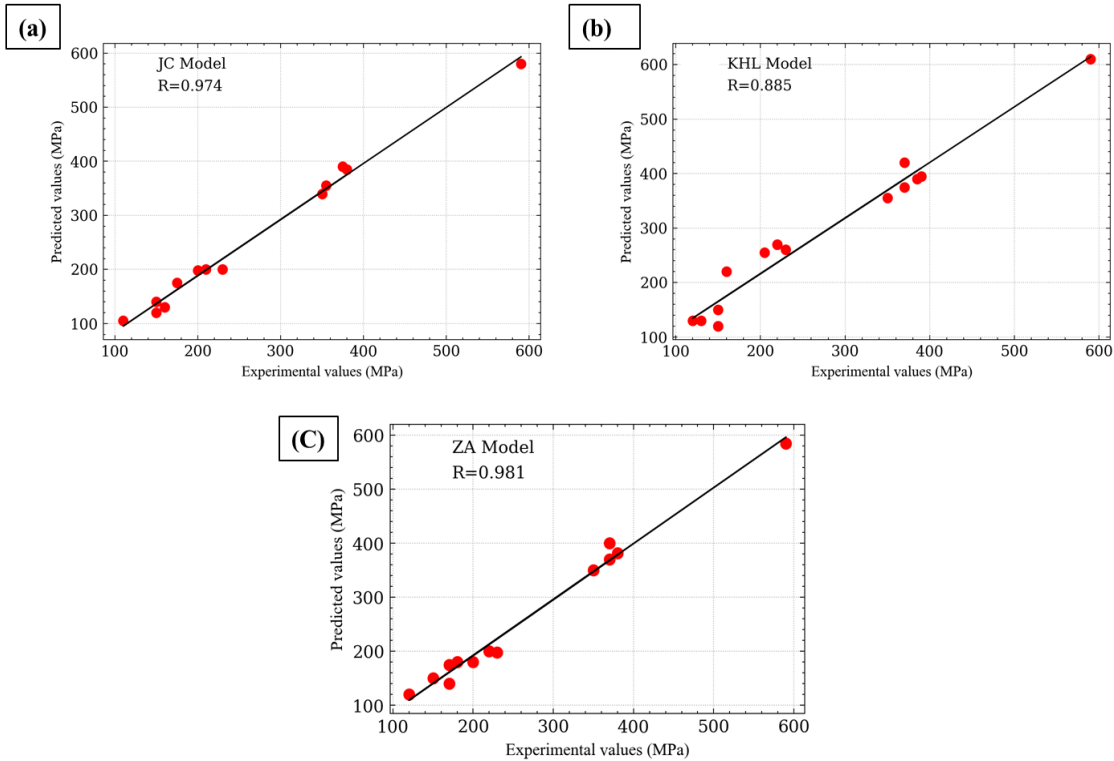


**Figure 4.18:** Correlation coefficient between the experimental and predicted stress values for: (a) JC model; (b)KHL model; (c) ZA model

Based on the statistics above, the majority of the data points are located around the fitting line. Under the three constitutive models' conditions (KHL model, the modified ZA model, the JC model), the values of R are 0.974, 0.885 and 0.981 respectively, while the values of AARE are 4.85%, 8.92% and 5.23% respectively as shown in table 4.5.

**Table 4.5:** Correlation coefficient and average absolute relative error between experimental and predicted flow data for different formulated constitutive models.

Parameter	Material model		
	JC model	KHL model	Modified ZA model
Correlation coefficient, R	0.974	0.885	0.981
Average absolute relative error, AARE (%)	4.85	8.932	5.23

It can be observed from the combined results of AARE and R that the JC model and ZA models demonstrates a better correlation between the experimental data and predicted results compared with others.

Normally, a perfect fit gives a correlation coefficient of 1, which means the higher the correlation coefficient, the stronger the linear relationship between experimental and predicted data. However, this does not mean that the performance of the model is high, because the model might have a tendency to be biased towards higher or lower values of the sample data [174]. However, this correlation only studies the fitting values doesn't give the relation between the nonlinear effect due to the temperature, strain and strain rate.

Hence to explain the nonlinear degree of effect of the three factors (strain, strain rate, and temperature) for the flow stress on the fitting results in different models, the absolute residual values for the factors are drawn in Figure 4.19.

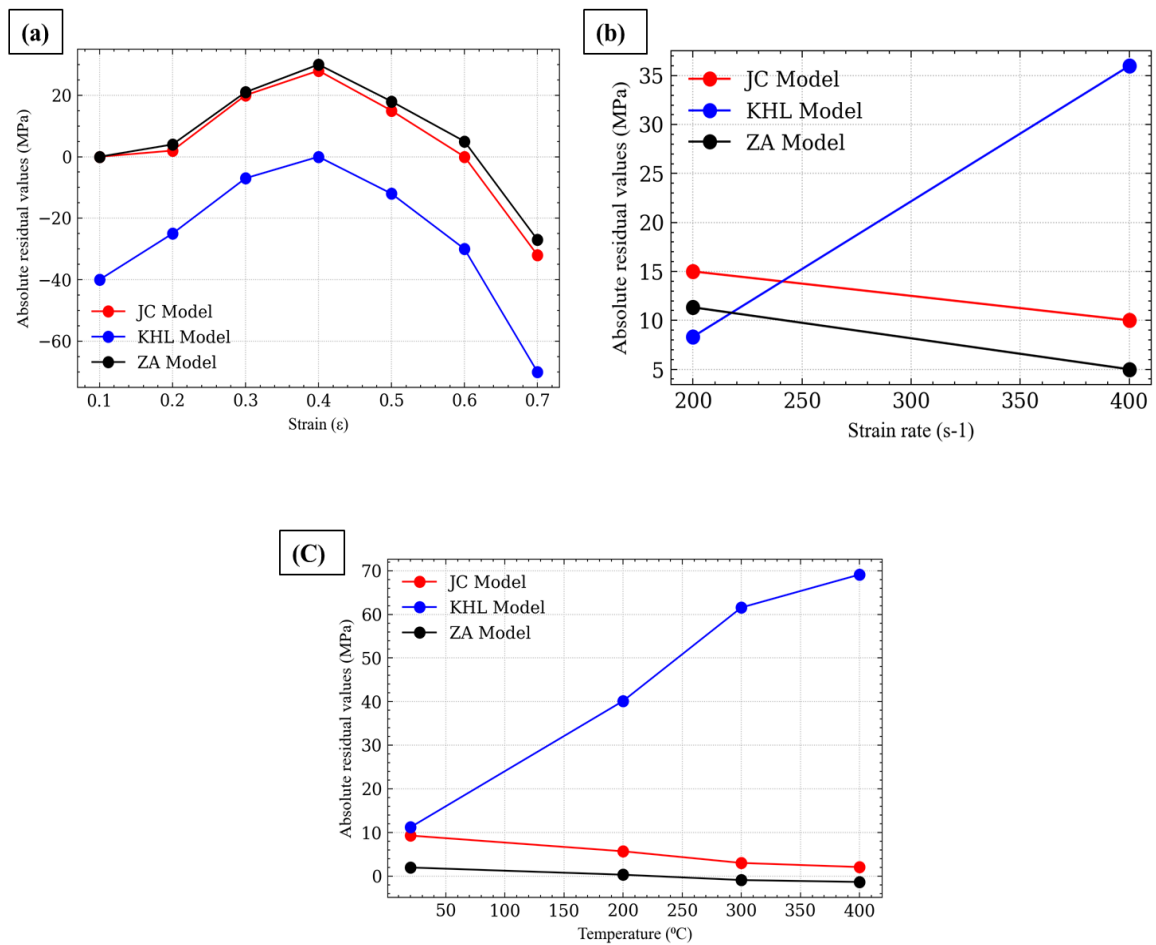


**Figure 4.19:** Absolute residual values from three models of (a) strain, (b) strain rate, and (c) temperature.

As shown in Figure 4.19a, it is clear that the residual values increase with the raise of strain and then decreases for the JC model and the modified ZA model, they also fluctuate at about zero values at the initial strain. Whereas at KHL model, there is a negative absolute

residual value, it shows that the predicted curve is under the experimental flow stress. Regarding the strain rate (Figure 4.19b) similarly, the absolute residual value for the JC and ZA model is the smallest and the values for the KHL model vary more at the strain rate from  $200\text{s}^{-1}$  to  $400\text{s}^{-1}$ . According to Figure 4.19 c), the value obtained from the KHL model changes largely from  $20^\circ\text{C}$  to  $400^\circ\text{C}$ . Whereas, the trends of the other two model are similar and fluctuates near zero values as the temperature increase, it means that the model shows good agreement with temperature effect. It means that both models can predict more accurately the material behaviour of AA7075-T6 alloy.

Several researchers have evaluated the different parameters for given material models based on their experimental condition. For example, Brar et al. [51] evaluated the JC parameters for the AA7075-T6 by performing the quasi static test and split Hopkinson pressure bar test at various strain rate and temperatures given in Table 4.6. Reference strain rate and temperature are  $1\text{s}^{-1}$  and  $25^\circ\text{C}$  respectively.

**Table 4.6:** JC parameters based on Brar et al [51]

J-C Model	Initial Conditions		J-C Parameters				
	Strain Rate $\text{s}^{-1}$	Temperature $^\circ\text{C}$	A(MPa)	B (MPa)	n	C	m
Brar et al	1-1700	25°-250°	546	678	0.71	0.024	1.56

Similarly, Ma et al. evaluated the modified ZA model parameters for the AA7075-T6 by performing the gleeble test at various strain rate and temperatures given in Table 4.7.

**Table 4.7:** Modified ZA model parameters based on Ma et al

Modified ZA Model	Initial Conditions		Parameters						
	Strain rate $\text{s}^{-1}$	Temperature $^\circ\text{C}$	C <sub>1</sub>	C <sub>2</sub>	C <sub>3</sub>	C <sub>4</sub>	C <sub>5</sub>	C <sub>6</sub>	n
Ma et al.	$0.01\text{s}^{-1}$	$350^\circ$	68.55	18.36	0.008	-0.0006	0.12	0.00059	0.025

We used these parameters to fit our experimental stress-strain curves, but it appears that the parameter obtained from the literature does not show a good agreement with the experimental curves as shown in Figure 4.20 a,b). However, for JC model, at room temperature, the curves show a good fit. But with the increase of temperature, the both model parameters are no longer good enough to fit the thermal effect.

We tried to compare several other parameters existing in the literature with our experimental results, but they do not provide satisfactory results. It means that the models' parameters are different for each set of experiments and not one single set of parameters can predict the complete range of strain rate and temperature depended flow stress curve. This is one of the major drawbacks of the existing model, hence there is a need to significantly improve the existing material model or develop an accurate new material behaviour model, which can cover material behaviour at all range of strain rate, strain and temperature.

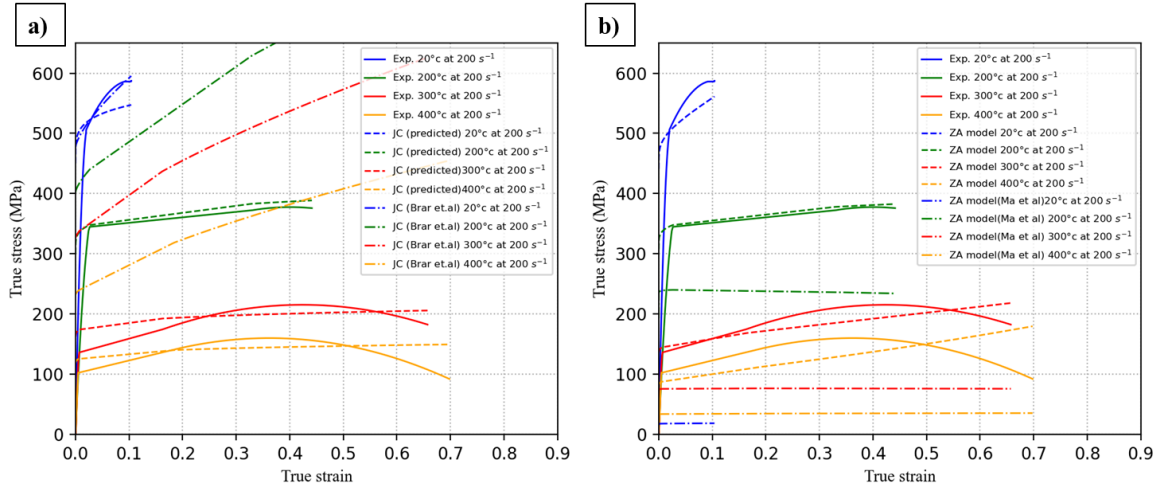


**Figure 4.20:** Constitutive model (a) JC model (b) modified ZA model predicted and from the literature (Brar et al.) at different temperatures and strain rate of  $200\text{s}^{-1}$

It is also noticed that AA7075-T6 alloy is not strain rate dependent in the intermediate strain rate range and also from the experimental results, it is found that the flow stress curves do not show exceptional change due to the large strain and at high temperature. Therefore, it is possible that several existing material models can predict the accurate behaviour of AA7075-T6 with correct modelling parameters.

## 4.5 Conclusion

The purpose of this work is to formulate the flow behaviour of the aerospace aluminium alloy AA7075-T6 by performing torsion tests over a practical range of deformation temperatures and intermediate strain rates, in order to validate the existing conventional constitutive models normally used in the industry to simulate the manufacturing processes of AA7075-T6. A comparison is made to understand the predictive capabilities of the formulated models based on statistical parameters, such as correlation coefficient and

absolute error between experimental and predicted flow data. The results show that although the ZA and JC models give a good estimate of the linear dependence of the fit (correlation coefficient:  $R > 0.95$ ) between the experimental and predicted flow stresses.

However, there are some potential shortcomings in the given models, where the experimental flow stress results are not well predicted, especially at relatively high strain and temperature conditions. For example, it is observed that at high temperature, the experimental flow stress decreases and reaches the saturation level at a certain strain due to the softening mechanism. These softening behaviours doesn't study by the given models. In addition, during hot and dynamic deformation process, the internal microstructure of material changes extensively, and the given material models are not able to give an accurate interpretation. Which includes working hardening due to dislocation interactions, dynamic softening ascribes to thermal activation, formation of dynamic recrystallization and adiabatic shear bands, etc. The study of this microstructural evolution in the constitutive equation is very important in order to obtain accurate FEM simulation analysis to predict the complete material behaviour during the manufacturing processes. However, several investigations show that there is some existing material model which studies the microstructural behaviour. But these models are very complex and there are many material parameters in the constitutive models, and the determination of these material parameters are not very easy, it requires some precision apparatuses. After development of new torsion test bench, we will be able to predict and determine all parameters required for developing new microstructural based material model in near future.

## CONCLUSION AND PERSPECTIVES

The material behaviour in manufacturing processes is important to understand for the research society in order to develop an accurate material model. For such material behaviour analysis, experimental tests provide a useful means to investigate the material behaviour in a realistic manner. However, the existing experimental testing devices do not cover the complete material behaviour that occurs during manufacturing processes. For example, during machining and FSW processes, the material is subjected to high temperature, intermediate/high strain rate with large deformation, and most of the thermomechanical stresses applied during these processes are shear stresses, in addition to that, the microstructural changes occurring during these processes have not been well studied to develop a good material model. So, in order to understand the deficiency of the accurate experimental testing device, a literature review is carried out.

The material chosen for this research work is AA7075-T6 alloy widely used in aerospace industries. The behaviour of AA7075-T6 alloy in different manufacturing processes, especially in machining and FSW, is discussed in detail. It is found that the microstructure evolution of the material is mainly due to shear deformation at medium strain rate and high temperature. Existing material models used for manufacturing processes are also studied, including their applications, advantages, and disadvantages. Some existing shear test devices are reviewed. Several representative shear specimens and corresponding test techniques were presented. Finally, a review of the intermediate test setup is given. It is found out that there is no intermediate strain rate testing available to perform a shear test. Moreover, there is not enough work done on high-temperature experimental testing in shear.

Therefore, in this work, a new experimental torsion test bench is designed and developed to perform a shear test at an intermediate strain rate based on the flywheel principle. Some essential theories and techniques, such as the torsional loading mechanism, technical features, e.g. the guiding the specimen in rotation, the position of the contact between the hammer and the anvil, the coupling pin design, measuring techniques, high temperature device, and its working principles, etc. are explained in detail. After the manufacturing of the test device, the calibration of the different measuring components is carried out in order to obtain accurate torque and deformation results. Finally, the preliminary tests are performed. Most of the validation tests and test results were presented. The torque and shear strain results

show good repeatability and post-processing of the data is very straightforward. Note that for the presented tests, the plastic strain rate reaches in the range of intermediate strain rate. It is important to notice that reaching such values with a classical split Hopkinson configuration would have implied a very large length of the bar. Thanks to this loading system, we are not limited. The design of this torsion device allows for a wide variety of materials (metallic and non-metallic). With a given range of flywheel speeds from 1 to 40 m/s and torque measurement capability (Hopkinson bar torque sensor, 1-1000Nm), a wide range of applications is possible.

After the development of the new torsion test device, the experimental tests at room temperature and elevated temperature are carried out for AA7075-T6 alloy. At room temperature, the tests are performed for different lengths of the specimens (short and long specimens) and it shows that the stress level obtained for short and long specimens is almost similar. It is also observed that at different loading speeds, the stress level seems to be similar, which means that AA7075-T6 is not a strain rate sensitive alloy. Adiabatic shear bands (ASBs) are clearly observed for short specimens and all short specimens are fractured. It is also observed that the width of the ASBs decreases with increasing flywheel speed and the temperature inside the specimen increases with increasing flywheel speed. The level of strain decreases as the loading speed decreases. For long specimens, there is no formation of ASB for the lower speed of flywheel (except at a speed of 12m/s), where the level of strain was not enough to fracture the specimens. This means that the torque transmitted along the entire length of the specimen did not act long time enough for long specimens at lower speeds. Because of this phenomenon, it is possible to perform an interrupted test by simply changing the flywheel speed using our torsion test bench. We also note that for long specimens, an inhomogeneous distribution of shear strain is observed along the length of the specimen.

At high temperature tests, all the tests are performed on the long specimen. The set of experiments are design based on Doehlert's matrix, which provides a better analysis of preliminary experimental results based on the input parameters of loading speed and temperature. Then the mechanical and microstructural behavior of AA7075-T6 alloy during deformation with different strain rates at different temperatures have been studied and analyzed. It is observed that the flow stress decreases with temperature as expected. The material experiences a greater extent of softening for higher strain rate at elevated

temperatures of 300°C and above, whereas at 200°C the extent of softening is more in case of lower strain rate. Temperatures above 300°C and also increase with strain rate, new recrystallized grains are formed in the grain boundary. And as the temperature rises, more and more fine grains are accumulated. Microstructure evolution refers to the mechanism of continuous dynamic recrystallization (CDRX) with discontinuous and geometric features.

DRX observed in this research is fully and partially takes place in local areas of the transverse direction (TD) surface and longitudinal direction (LD) surface of the specimen. Furthermore, the degree of DRX is found to increase in case of deformation with higher temperature and higher strain rate. Depending on the location of the specimen, different material points experience different degrees of local plastic strain and thereby corresponding degree of DRX (TD surface). The microstructure analysis on LD surfaces shows that the grains near fracture surfaces are elongated and rotated extensively due to large shear deformation. The macro and micro images show that the grains are uniformly deformed along the direction of the shear load. The formation of DRX near the fracture surface where the shear localization occurred has many similarities with the behavior of the microstructure during machining (shear localization zone in the chip morphology) and FSW processes (NZ and TMAZ zone). In short, the new torsion tests provide a new way to study the plastic deformation at room and high temperatures. Thus, this type of experimental test can be used as a tool to develop a material's constitutive equation.

After extensive study of the flow stress behaviour of the aerospace aluminium alloy AA7075-T6 by performing torsion tests over a practical range of deformation temperatures and at intermediate strain rates. It is important to validate the experimental flow stress strain curves with the existing conventional constitutive models normally used in the industry to simulate the manufacturing processes of AA7075-T6. Hence the comparison is made using three different material models such as Johnson cook (JC), Khan–Huang–Liang (KHL) and Zerilli-Armstrong (ZA) model. A comparison is made to understand the predictive capabilities of the formulated models based on statistical parameters. And the results show that although the ZA and JC models give a good estimate of the linear dependence of the fit (correlation coefficient:  $R > 0.95$ ) between the experimental and predicted flow stresses compared to the KHL model. However, there are some potential shortcomings in the given models, where the experimental flow stress results are not well predicted, especially at



relatively high strain and temperature conditions. In addition, during the hot and dynamic deformation process, the internal microstructure of material changes extensively, and the given material models are not able to give an accurate interpretation. This includes working hardening due to dislocation and dislocation interactions, dynamic softening ascribes to thermal activation, formation of dynamic recrystallization and adiabatic shear bands, etc. The study of this microstructural evolution in the constitutive equation is very important in order to obtain accurate FEM simulation analysis to predict the complete material behaviour during the manufacturing processes. Therefore, it is necessary to develop a new material model based on microstructure using the new torsion test by analysing the mechanical and microstructure changes obtained after the experimental tests. In addition, the existing material modelling parameters from the literature are different for each set of experiments and not one single set of parameters can predict the complete range of strain rate and temperature dependent flow stress behaviour. This is one of the major drawbacks of the existing model and which has to be improved, which can cover material behaviour at all range of strain rate, strain and temperature.

## **FUTURE WORK**

Project deadlines and due to the effect of the pandemic, we were restricted by the limited time. However, there is still some work remaining to be done.

First, as already discussed in chapter 4, the existing material model is not able to predict the exact flow stress behaviour and does not account for the microstructural changes that occur at different intermediate strain rates and high temperatures. Hence, in order to develop an accurate microstructural-based model, further investigation is required in terms of microstructural point of view. For example, statistical analysis of grain size, orientation, dislocation density, change in precipitation hardening at different temperature, strain rates, strains, etc.

Second, it was seen that by using a long specimen, it is possible to observe inhomogeneous strain distribution along the length of the specimen. So, in order to further investigate the strain distribution over the length of the specimen. Several experimental tests need to perform for different lengths of the specimen.

Third, the strain measuring technique is always the big problem in dynamic high temperature testing. In this work, we designed a simple system to directly measure the global

deformation by measuring the torsion angle of the specimen during the test by fixing the angular protractor on the loading side of the torsion module. The needle pointer is fixed to the clamp (specimen and anvil cylinder), after the hammer-anvil impact, needle pointer rotates with the anvil cylinder and the movement of the pointer is captured by using high speed camera and using image processing, the angle of twist on the specimen is depicted. However, this system still needs some improvements in the angle protractor part, as it was only a prototype. Thus, the permanent part of this protractor must be fixed. Similarly, it will be interesting to fix the angular protractor on both sides of the specimen in order to measure the relative angular motion of the loading end of the specimen and the bar.

Fourth, for very low loading speed, the time of impact between the hammer-anvil is larger and during this time period there will be the reflection of the torsion waves in the bar and it might influence the load measurement of the specimen. So, in order to prevent the reflection of torsion waves from the free end, the wave trap or dynamic recovery system will be introduced in the torsion device. This system will allow to perform tests at any loading speed without any interference of waves in the bar.

Finally, as we know aluminum alloy is not the best candidate to investigate strain rate effect on the material response. Several experimental tests have to be performed for low to high strength materials at different loading speeds and temperatures to study the behavior of the materials under shear loading at intermediate strain rates. In addition, our test bench is a first prototype, from the experimentation experience, we know that some parts of the test bench need to be improved.

## REFERENCES

- [1] C. (Christoph) Leyens, M. (Manfred) Peters, Titanium and titanium alloys : fundamentals and applications, Wiley-VCH, 2003.
- [2] C.A.L. Composition, M. T-, TIMETAL 6-4, 6-4 ELI, 6-4-.1Ru, Alloy Dig. 56 (2007) 5–6. <https://doi.org/10.31399/asm.ad.ti0143>.
- [3] I. Inagaki, T. Takechi, Y. Shirai, N. Ariyasu, Application and features of titanium for the aerospace industry, Nippon Steel Sumitomo Met. Tech. Rep. 106 (2014) 22–27.
- [4] S.P.F.C. Jaspers, J.H. Dautzenberg, Material behaviour in metal cutting: Strains, strain rates and temperatures in chip formation, J. Mater. Process. Technol. 121 (2002) 123–135. [https://doi.org/10.1016/S0924-0136\(01\)01227-4](https://doi.org/10.1016/S0924-0136(01)01227-4).
- [5] Y.B. Guo, An integral method to determine the mechanical behavior of materials in metal cutting, J. Mater. Process. Technol. 142 (2003) 72–81. [https://doi.org/10.1016/S0924-0136\(03\)00462-X](https://doi.org/10.1016/S0924-0136(03)00462-X).
- [6] E.A. Starke, J.T. Staley, Application of modern aluminium alloys to aircraft, Woodhead Publishing Limited, 2010. <https://doi.org/10.1533/9780857090256.3.747>.
- [7] A.A. Popovich, V.S. Sufiiarov, I.A. Polozov, E. V. Borisov, Microstructure and mechanical properties of Inconel 718 produced by SLM and subsequent heat treatment, in: Key Eng. Mater., Trans Tech Publications Ltd, 2015: pp. 665–670. <https://doi.org/10.4028/www.scientific.net/KEM.651-653.665>.
- [8] T. Dursun, C. Soutis, Recent developments in advanced aircraft aluminium alloys, Mater. Des. 56 (2014) 862–871. <https://doi.org/10.1016/j.matdes.2013.12.002>.
- [9] A.A.S.M. Inc., Aluminum 7075-T6;7075-T651, (n.d.). <http://asm.matweb.com/search/SpecificMaterial.asp?bassnum=MA7075T6>.
- [10] E.S. Puchi-Cabrera, M.H. Staia, E. Ochoa-Pérez, J.G. La Barbera-Sosa, C. Villalobos-Gutierrez, A. Brenlla-Caires, Flow stress and ductility of AA7075-T6 aluminum alloy at low deformation temperatures, Mater. Sci. Eng. A. 528 (2011) 895–905. <https://doi.org/10.1016/j.msea.2010.11.002>.

- [11] R.F. Muraca, J.S. Whittick, Aluminum Alloy 7075 (2nd Edition), in: Mater. Data Handb., San Carlos, California, 1972: p. 132.
- [12] UACJ, Aluminum Forged Products for Aerospace Applications, (n.d.). <https://www.uacj.co.jp/english/products/cast-forg/aerospace.htm>.
- [13] Z.C. Sun, L.S. Zheng, H. Yang, Softening mechanism and microstructure evolution of as-extruded 7075 aluminum alloy during hot deformation, Mater. Charact. 90 (2014) 71–80. <https://doi.org/10.1016/j.matchar.2014.01.019>.
- [14] H. Ferguson, Heat Treating of Powder Metallurgy Steels, Heat Treat. 4 (1991) 229–236.
- [15] N. Mahathaninwong, T. Plookphol, J. Wannasin, S. Wisutmethangoon, T6 heat treatment of rheocasting 7075 Al alloy, Mater. Sci. Eng. A. 532 (2012) 91–99. <https://doi.org/10.1016/j.msea.2011.10.068>.
- [16] F. Andreatta, H. Terryn, J.H.W. de Wit, Effect of solution heat treatment on galvanic coupling between intermetallics and matrix in AA7075-T6, Corros. Sci. 45 (2003) 1733–1746. [https://doi.org/10.1016/S0010-938X\(03\)00004-0](https://doi.org/10.1016/S0010-938X(03)00004-0).
- [17] C.E. Campbell, L.A. Bendersky, W.J. Boettinger, R. Ivester, Microstructural characterization of Al-7075-T651 chips and work pieces produced by high-speed machining, Mater. Sci. Eng. A. 430 (2006) 15–26. <https://doi.org/10.1016/j.msea.2006.04.122>.
- [18] S.C. Jacumasso, J. de P. Martins, A.L.M. de Carvalho, Analysis of precipitate density of an aluminium alloy by TEM and AFM, Rev. Esc. Minas. 69 (2016) 451–457. <https://doi.org/10.1590/0370-44672016690019>.
- [19] W. Zhang, X. Chen, B. Zhuo, P. Li, L. He, Effect of strain rate and temperature on dynamic mechanical behavior and microstructure evolution of ultra-high strength aluminum alloy, Mater. Sci. Eng. A. 730 (2018) 336–344. <https://doi.org/10.1016/j.msea.2018.06.018>.
- [20] P.L. Mao, B. Yu, Z. Liu, F. Wang, Y. Ju, Mechanical properties and electronic

- structures of MgCu<sub>2</sub>, Mg<sub>2</sub>Ca and MgZn<sub>2</sub> Laves phases by first principles calculations, *Trans. Nonferrous Met. Soc. China (English Ed.* 24 (2014) 2920–2929. [https://doi.org/10.1016/S1003-6326\(14\)63427-0](https://doi.org/10.1016/S1003-6326(14)63427-0).
- [21] J.B. Friauf, Crystal structure of magnesium, *Phys. Rev.* 29 (1924) 34–40.
- [22] T.M. Yue, L.J. Yan, C.P. Chan, C.F. Dong, H.C. Man, G.K.H. Pang, Excimer laser surface treatment of aluminum alloy AA7075 to improve corrosion resistance, *Surf. Coatings Technol.* 179 (2004) 158–164. [https://doi.org/10.1016/S0257-8972\(03\)00850-8](https://doi.org/10.1016/S0257-8972(03)00850-8).
- [23] K.B. Ahsan, A.M. Mazid, G.K.H. Pang, Morphological investigation of Ti-6Al-4V chips produced by conventional turning, *Int. J. Mach. Mach. Mater.* 18 (2016) 138–154. <https://doi.org/10.1504/IJMMM.2016.075472>.
- [24] S. Atlati, B. Haddag, M. Nouari, M. Zenasni, Thermomechanical modelling of the tool-workmaterial interface in machining and its implementation using the ABAQUS VUINTER subroutine, *Int. J. Mech. Sci.* 87 (2014) 102–117. <https://doi.org/10.1016/j.ijmecsci.2014.05.034>.
- [25] L. Deshayes, T. Mabrouki, R. Ivester, J.F. Rigal, Serrated chip morphology and comparison with finite element simulations, *Am. Soc. Mech. Eng. Manuf. Eng. Div. MED.* 15 (2004) 815–824. <https://doi.org/10.1115/IMECE2004-60717>.
- [26] G.G. Ye, Y. Chen, S.F. Xue, L.H. Dai, Critical cutting speed for onset of serrated chip flow in high speed machining, *Int. J. Mach. Tools Manuf.* 86 (2014) 18–33. <https://doi.org/10.1016/j.ijmachtools.2014.06.006>.
- [27] T. Mabrouki, F. Girardin, M. Asad, J.F. Rigal, Numerical and experimental study of dry cutting for an aeronautic aluminium alloy (A2024-T351), *Int. J. Mach. Tools Manuf.* 48 (2008) 1187–1197. <https://doi.org/10.1016/j.ijmachtools.2008.03.013>.
- [28] Anon, Friction welding, *Weld. J. (Miami, Fla.)* 78 (1999) 56. <https://doi.org/10.22486/iwj.v10i2.148764>.
- [29] G.Z. Quan, G.S. Li, Y. Wang, W.Q. Lv, C.T. Yu, J. Zhou, A characterization for the flow behavior of as-extruded 7075 Aluminum alloy by the improved arrhenius model with variable parameters, *Mater. Res.* 16 (2013) 19–27.

- <https://doi.org/10.1590/S1516-14392012005000156>.
- [30] R.A. Prado, L.E. Murr, D.J. Shindo, K.F. Soto, <Tool wear in the FSW of aluminium 6061.pdf>, 45 (2001) 75–80.
- [31] J.Q. Su, T.W. Nelson, R. Mishra, M. Mahoney, Microstructural investigation of friction stir welded 7050-T651 aluminium, *Acta Mater.* 51 (2003) 713–729. [https://doi.org/10.1016/S1359-6454\(02\)00449-4](https://doi.org/10.1016/S1359-6454(02)00449-4).
- [32] S. Benavides, Y. Li, L.E. Murr, D. Brown, J.C. McClure, Low-temperature friction-stir welding of 2024 aluminum, *Scr. Mater.* 41 (1999) 809–815. [https://doi.org/10.1016/S1359-6462\(99\)00226-2](https://doi.org/10.1016/S1359-6462(99)00226-2).
- [33] D.P. Field, T.W. Nelson, Y. Hovanski, K. V. Jata, Heterogeneity of crystallographic texture in friction stir welds of aluminum, *Metall. Mater. Trans. A Phys. Metall. Mater. Sci.* 32 (2001) 2869–2877. <https://doi.org/10.1007/s11661-001-1037-2>.
- [34] L. E. Murr, G. Liu, J. C. McClure, Dynamic recrystallization in friction-stir welding of aluminium alloy 1100, *J. Mater. Sci. Lett.* 16 (1997) 1801–1803.
- [35] G. Ipekoglu, S. Erim, G. Cam, Investigation into the influence of post-weld heat treatment on the friction stir welded AA6061 Al-Alloy plates with different temper conditions, *Metall. Mater. Trans. A Phys. Metall. Mater. Sci.* 45 (2014) 864–877. <https://doi.org/10.1007/s11661-013-2026-y>.
- [36] D. Ambrosio, V. Wagner, C. Garnier, D. Jacquin, A. Tongne, M. Fazzini, O. Cahuc, G. Desein, Influence of welding parameters on the microstructure, thermal fields and defect formation in AA7075-T6 friction stir welds, *Weld. World.* 64 (2020) 773–784. <https://doi.org/10.1007/s40194-020-00869-4>.
- [37] Y.C. Lin, X.M. Chen, A critical review of experimental results and constitutive descriptions for metals and alloys in hot working, *Mater. Des.* 32 (2011) 1733–1759. <https://doi.org/10.1016/j.matdes.2010.11.048>.
- [38] G.R. Johnson, W. Cook, A CONSTITUTIVE MODEL AND DATA FOR METALS SUBJECTED TO LARGE STRAINS, HIGH STRAIN RATES AND HIGH TEMPERATURES, *Proc. 7th Int. Symp. Ballist. Hague.* 19–21 (1983) 541–547.

- [39] A.S. Khan, S. Huang, Experimental and theoretical study of mechanical behavior of 1100 aluminum in the strain rate range  $10^{-5}$ - $10^4$ s $^{-1}$ , *Int. J. Plast.* 8 (1992) 397–424. [https://doi.org/10.1016/0749-6419\(92\)90057-J](https://doi.org/10.1016/0749-6419(92)90057-J).
- [40] A.S. Khan, H. Zhang, L. Takacs, Mechanical response and modeling of fully compacted nanocrystalline iron and copper, *Int. J. Plast.* 16 (2000) 1459–1476. [https://doi.org/10.1016/S0749-6419\(00\)00023-1](https://doi.org/10.1016/S0749-6419(00)00023-1).
- [41] A.S. Khan, Y.S. Suh, R. Kazmi, Quasi-static and dynamic loading responses and constitutive modeling of titanium alloys, *Int. J. Plast.* 20 (2004) 2233–2248. <https://doi.org/10.1016/j.ijplas.2003.06.005>.
- [42] A.S. Khan, Y.S. Suh, X. Chen, L. Takacs, H. Zhang, Nanocrystalline aluminum and iron: Mechanical behavior at quasi-static and high strain rates, and constitutive modeling, *Int. J. Plast.* 22 (2006) 195–209. <https://doi.org/10.1016/j.ijplas.2004.07.008>.
- [43] B. Farrokh, A.S. Khan, Grain size, strain rate, and temperature dependence of flow stress in ultra-fine grained and nanocrystalline Cu and Al: Synthesis, experiment, and constitutive modeling, *Int. J. Plast.* 25 (2009) 715–732. <https://doi.org/10.1016/j.ijplas.2008.08.001>.
- [44] D.S. Fields, W.A. Backofen, Determination of Strain Hardening Characteristics by Torsion Testing, *Proceeding Am. Soc. Test. Mater.* 57 (1957) 1259–1272.
- [45] A. Molinari, G. Ravichandran, Constitutive modeling of high-strain-rate deformation in metals based on the evolution of an effective microstructural length, *Mech. Mater.* 37 (2005) 737–752. <https://doi.org/10.1016/j.mechmat.2004.07.005>.
- [46] VOCE, E., The Relationship between Stress and Strain for Homogeneous Deformation, *J. Inst. Met.* 74 (1948) 537–562. <http://ci.nii.ac.jp/naid/10026664078/en/> (accessed August 10, 2021).
- [47] C. Zener, J.H. Hollomon, Effect of strain rate upon plastic flow of steel, *J. Appl. Phys.* 15 (1944) 22–32. <https://doi.org/10.1063/1.1707363>.
- [48] H. Shi, J. McLaren, C.M. Sellars, R. Shahani, R. Bolingbroke, Constitutive equations for high temperature flow stress of aluminium alloys, *Mater. Sci. Technol.* 13 (1997)

- 210–216.
- [49] Y.C. Lin, G. Liu, A new mathematical model for predicting flow stress of typical high-strength alloy steel at elevated high temperature, *Comput. Mater. Sci.* 48 (2010) 54–58. <https://doi.org/10.1016/j.commatsci.2009.06.026>.
- [50] D.N. Zhang, Q.Q. Shangguan, C.J. Xie, F. Liu, A modified Johnson-Cook model of dynamic tensile behaviors for 7075-T6 aluminum alloy, *J. Alloys Compd.* 619 (2015) 186–194. <https://doi.org/10.1016/j.jallcom.2014.09.002>.
- [51] N.S. Brar, V.S. Joshi, B.W. Harris, Constitutive model constants for Al7075-T651 and Al7075-T6, *AIP Conf. Proc.* 1195 (2009) 945–948. <https://doi.org/10.1063/1.3295300>.
- [52] A. Shrot, M. Bäker, Determination of Johnson-Cook parameters from machining simulations, *Comput. Mater. Sci.* 52 (2012) 298–304. <https://doi.org/10.1016/j.commatsci.2011.07.035>.
- [53] B. Wang, Z. Liu, Q. Song, Y. Wan, X. Ren, A modified johnson-cook constitutive model and its application to high speed machining of 7050-T7451 aluminum alloy, *J. Manuf. Sci. Eng. Trans. ASME.* 141 (2019). <https://doi.org/10.1115/1.4041915>.
- [54] G. Chen, C. Ren, Z. Ke, J. Li, X. Yang, Modeling of flow behavior for 7050-T7451 aluminum alloy considering microstructural evolution over a wide range of strain rates, *Mech. Mater.* 95 (2016) 146–157. <https://doi.org/10.1016/j.mechmat.2016.01.006>.
- [55] M. Calamaz, D. Coupard, F. Girot, A new material model for 2D numerical simulation of serrated chip formation when machining titanium alloy Ti-6Al-4V, *Int. J. Mach. Tools Manuf.* 48 (2008) 275–288. <https://doi.org/10.1016/j.ijmachtools.2007.10.014>.
- [56] F.J. Zerilli, R.W. Armstrong, Dislocation-mechanics-based constitutive relations for material dynamics calculations, *J. Appl. Phys.* 61 (1987) 1816–1825. <https://doi.org/10.1063/1.338024>.
- [57] S.R. Bodner, Y. Partom, Constitutive equations for elastic-viscoplastic strain-hardening materials, *J. Appl. Mech. Trans. ASME.* 42 (1975) 385–389. <https://doi.org/10.1115/1.3423586>.



- [58] A. Rusinek, Shear testing of a sheet steel at wide range of strain rates and a constitutive relation with strain-rate and temperature dependence of the flow stress, *Int. J. Plast.* 17 (2001) 87–115. [https://doi.org/10.1016/S0749-6419\(00\)00020-6](https://doi.org/10.1016/S0749-6419(00)00020-6).
- [59] B. Banerjee, The Mechanical Threshold Stress model for various tempers of AISI 4340 steel, *Int. J. Solids Struct.* 44 (2007) 834–859. <https://doi.org/10.1016/j.ijsolstr.2006.05.022>.
- [60] B. Banerjee, A.S. Bhawalkar, An extended mechanical threshold stress plasticity model: Modeling 6061-T9 aluminum alloy, *J. Mech. Mater. Struct.* 3 (2008) 391–424. <https://doi.org/10.2140/jomms.2008.3.391>.
- [61] S. Gourdet, F. Montheillet, A model of continuous dynamic recrystallization, 51 (2003) 2685–2699. [https://doi.org/10.1016/S1359-6454\(03\)00078-8](https://doi.org/10.1016/S1359-6454(03)00078-8).
- [62] U.M.R. Paturi, S.K.R. Narala, R.S. Pundir, Constitutive flow stress formulation, model validation and FE cutting simulation for AA7075-T6 aluminum alloy, *Mater. Sci. Eng. A.* 605 (2014) 176–185. <https://doi.org/10.1016/j.msea.2014.03.033>.
- [63] Z. Ma, H.C. Ji, W.C. Pei, S.F. Wang, Y.G. Li, Constitutive relationship of 7075 aluminum alloy Based on modified zerilli-armstrong (m-za) model, *Anal. Zavoda Za Povij. Znan. Hrvat. Akad. Znan. i Umjet. u Dubrovniku.* 60 (2021) 269–272.
- [64] A. Rusinek, J.R. Klepaczko, Shear testing of a sheet steel at wide range of strain rates and a constitutive relation with strain-rate and temperature dependence of the  $\sigma$  flow stress, n.d. [www.elsevier.com/locate/ijplas](http://www.elsevier.com/locate/ijplas).
- [65] S. Gourdet, F. Montheillet, A model of continuous dynamic recrystallization, *Acta Mater.* 51 (2003) 2685–2699. [https://doi.org/10.1016/S1359-6454\(03\)00078-8](https://doi.org/10.1016/S1359-6454(03)00078-8).
- [66] M.A. Meyers, D.J. Benson, O. Vöhringer, B.K. Kad, Q. Xue, H.H. Fu, Constitutive description of dynamic deformation: Physically-based mechanisms, *Mater. Sci. Eng. A.* 322 (2002) 194–216. [https://doi.org/10.1016/S0921-5093\(01\)01131-5](https://doi.org/10.1016/S0921-5093(01)01131-5).
- [67] L.E. Lindgren, K. Domkin, S. Hansson, Dislocations, vacancies and solute diffusion in physical based plasticity model for AISI 316L, *Mech. Mater.* 40 (2008) 907–919. <https://doi.org/10.1016/j.mechmat.2008.05.005>.

- [68] V. Kalhori, D. Wedberg, L.E. Lindgren, Simulation of mechanical cutting using a physical based material model, *Int. J. Mater. Form.* 3 (2010) 511–514. <https://doi.org/10.1007/s12289-010-0819-8>.
- [69] V. Tarigopula, O.S. Hopperstad, M. Langseth, A.H. Clausen, F. Hild, O.G. Lademo, M. Eriksson, A study of large plastic deformations in dual phase steel using digital image correlation and FE analysis, in: *Proc. Soc. Exp. Mech. Inc.*, 2008: pp. 181–196. <https://doi.org/10.1007/s11340-008-9123-7>.
- [70] B.B. Hundy, A.P. Green, A determination of plastic stress-strain relations, *J. Mech. Phys. Solids.* 3 (1954) 16–21.
- [71] L. Murr, *Metallurgical Applications of Shock-Wave and High-Strain-Rate Phenomena* Skin: structure and mechanical response View project Surrogacy of Beryllium Welds View project, n.d. <https://www.researchgate.net/publication/255500686>.
- [72] J.D. Campbell, W.G. Ferguson, The temperature and strain-rate dependence of the shear strength of mild steel, *Philos. Mag.* 21 (1970) 63–82. <https://doi.org/10.1080/14786437008238397>.
- [73] Z. Wei, J. Yu, J. Li, Y. Li, S. Hu, Influence of stress condition on adiabatic shear localization of tungsten heavy alloys, *Int. J. Impact Eng.* 26 (2001) 843–852. [https://doi.org/10.1016/S0734-743X\(01\)00137-3](https://doi.org/10.1016/S0734-743X(01)00137-3).
- [74] G.T. Gray, K.S. Vecchio, V. Livescu, Compact forced simple-shear sample for studying shear localization in materials, *Acta Mater.* 103 (2016) 12–22. <https://doi.org/10.1016/j.actamat.2015.09.051>.
- [75] M. Meyers, R. Klopp, R. Clifton, T. Shawki, Pressure-Shear impact and dynamic viscoplastic response of metals, *Mech. Mater.* 4 (1985) 387–393.
- [76] T. Ahrens, N. Thadhani, A. Mutz, J. Vreelanf, R. Schwarz, J. Tyburczy, *Shock consolidation of aluminum-lithium powder*, Marcel Dekker INC, California, 1986.
- [77] B. Dodd, Y. Bai, A. Boston, H. London, Y. Oxford, P. San, D. San, F. Singapore, S. Tokyo, *Adiabatic Shear Localization Frontiers and Advances Second Edition*, ELSEVIER, 2012.

- [78] Z. Xu, X. Ding, W. Zhang, F. Huang, A novel method in dynamic shear testing of bulk materials using the traditional SHPB technique, *Int. J. Impact Eng.* 101 (2017) 90–104. <https://doi.org/10.1016/j.ijimpeng.2016.11.012>.
- [79] J.R. Klepaczko, H.V. Nguyen, W.K. Nowacki, Quasi-static and dynamic shearing of sheet metals, *Eur. J. Mech. A/Solids*. 18 (1999) 271–289. [https://doi.org/10.1016/S0997-7538\(99\)80016-3](https://doi.org/10.1016/S0997-7538(99)80016-3).
- [80] F.F. Shi, R. Merle, B. Hou, J.G. Liu, Y.L. Li, H. Zhao, A critical analysis of plane shear tests under quasi-static and impact loading, *Int. J. Impact Eng.* 74 (2014) 107–119. <https://doi.org/10.1016/j.ijimpeng.2014.06.012>.
- [81] G.T. Gray, K.S. Vecchio, V. Livescu, Compact forced simple-shear sample for studying shear localization in materials, *Acta Mater.* (2016). <https://doi.org/10.1016/j.actamat.2015.09.051>.
- [82] M.A. Meyers, Y.B. Xu, Q. Xue, M.T. Pérez-Prado, T.R. McNelley, Microstructural evolution in adiabatic shear localization in stainless steel, *Acta Mater.* 51 (2003) 1307–1325. [https://doi.org/10.1016/S1359-6454\(02\)00526-8](https://doi.org/10.1016/S1359-6454(02)00526-8).
- [83] J. Peirs, P. Verleysen, J. Degrieck, F. Coghe, The use of hat-shaped specimens to study the high strain rate shear behaviour of Ti-6Al-4V, *Int. J. Impact Eng.* (2010). <https://doi.org/10.1016/j.ijimpeng.2009.08.002>.
- [84] J. Peirs, P. Verleysen, J. Degrieck, Novel Technique for Static and Dynamic Shear Testing of Ti6Al4V Sheet, *Exp. Mech.* 52 (2012) 729–741. <https://doi.org/10.1007/s11340-011-9541-9>.
- [85] A. Dorogoy, D. Rittel, A. Godinger, A Shear-Tension Specimen for Large Strain Testing, *Exp. Mech.* 56 (2016) 437–449. <https://doi.org/10.1007/s11340-015-0106-1>.
- [86] D. Rittel, S. Lee, G. Ravichandran, A shear-compression specimen for large strain testing, *Exp. Mech.* 42 (2002) 58–64. <https://doi.org/10.1007/BF02411052>.
- [87] Z. Xu, Y. Liu, Z. Sun, H. Hu, F. Huang, On shear failure behaviors of an armor steel over a large range of strain rates, *Int. J. Impact Eng.* 118 (2018) 24–38. <https://doi.org/10.1016/j.ijimpeng.2018.04.003>.

- [88] J. DUFFY, Experimental Studies of Shear Band Formation Through Temperature Measurements and High Speed Photography, *Le J. Phys. IV*. 01 (1991) C3-645-C3-652. <https://doi.org/10.1051/jp4:1991390>.
- [89] J. Duffy, J.D. Campbell, R.H. Hawley, On the Use of a Torsional Split Hopkinson Bar to Study Rate Effects in 1100-0 Aluminum, *J. Appl. Mech.* 38 (1971) 83. <https://doi.org/10.1115/1.3408771>.
- [90] A. Marchand, J. Duffy, An experimental study of the formation process of adiabatic shear bands in a structural steel, *J. Mech. Phys. Solids*. 26 (1988) 251–283.
- [91] X. Liu, C. Tan, J. Zhang, Y. Hu, H. Ma, F. Wang, H. Cai, Influence of microstructure and strain rate on adiabatic shearing behavior in Ti-6Al-4V alloys, *Mater. Sci. Eng. A*. 501 (2009) 30–36. <https://doi.org/10.1016/j.msea.2008.09.076>.
- [92] H. Huh, K. Ahn, J.H. Lim, H.W. Kim, L.J. Park, Evaluation of dynamic hardening models for BCC, FCC, and HCP metals at a wide range of strain rates, *J. Mater. Process. Technol.* 214 (2014) 1326–1340. <https://doi.org/10.1016/j.jmatprotec.2014.02.004>.
- [93] J. Zhu, Y. Xia, G. Gu, Q. Zhou, Extension of Non-Associated Hill48 Model for Characterizing Dynamic Mechanical Behavior of a Typical High-Strength Steel Sheet, in: *ASME 2014 Int. Mech. Eng. Congr. Expo. IMECE2014*, ASME, Montreal, 2014: pp. 1–13.
- [94] X. Xiao, Dynamic tensile testing of plastic materials, *Polym. Test*. 27 (2008) 164–178. <https://doi.org/10.1016/j.polymertesting.2007.09.010>.
- [95] B. Hopkinson, A method of measuring the pressure produced in the detonation of high explosives or by the impact of bullets, *Philos. Trans. R. Soc. London. Ser. A, Contain. Pap. a Math. or Phys. Character.* 213 (1914) 437–456. <https://doi.org/10.1098/rsta.1914.0010>.
- [96] F. Taheri-Behrooz, M.M. Shokrieh, H.R. Abdolvand, Designing and manufacturing of a drop weight impact test machine, *Eng. Solid Mech.* 1 (2013) 69–76. <https://doi.org/10.5267/j.esm.2013.08.001>.
- [97] W. Chem, B. Song, *Split Hopkinson(Kolsky)Bar*, 20th ed., Springer, 2011.

- www.springer.com/series/1161.
- [98] T. Zhang, Progress and application of combined compression and shear wave loading technique, *Adv. Mech.* 37 (2007) 398–408.
- [99] W.P. Rogers, S. Nemat-Nasser, *Transformation Plasticity at High Strain Rate in Magnesia-Partially-Stabilized Zirconia*, 1990.
- [100] G.H. Staab, A. Gilat, A Direct-tension Split Hopkinson Bar for High Strain-rate Testing, *Exp. Mech.* 31 (1991) 232–235.
- [101] F.I. Niordson, A Unit for Testing Materials at High Strain Rates, *Exp. Mech.* 5 (1965) 29–32.
- [102] N. Gebbeken, S. Greulich, A. Pietzsch, Hugoniot properties for concrete determined by full-scale detonation experiments and flyer-plate-impact tests, *Int. J. Impact Eng.* 32 (2006) 2017–2031. <https://doi.org/10.1016/j.ijimpeng.2005.08.003>.
- [103] C.R. Hoggatt, R.F. Recht, Stress-strain data obtained at high rates using an expanding ring, *Exp. Mech.* 9 (1969) 441–448. <https://doi.org/10.1007/bf02410405>.
- [104] W.E. BAKER, C.H. YEW, Strain-Rate Effects in the Propagation of Torsional Plastic Waves, *Appl. Mech.* 9 (1966). <https://doi.org/10.1115/1.3625202>.
- [105] X. Nie, R. Prabhu, W.W. Chen, J.M. Caruthers, T. Weerasooriya, A Kolsky Torsion Bar Technique for Characterization of Dynamic Shear Response of Soft Materials, *Exp. Mech.* 51 (2011) 1527–1534. <https://doi.org/10.1007/s11340-011-9481-4>.
- [106] X. Yu, L. Chen, Q. Fang, Y. Zhou, An Electromagnetic driven Torsional Split Hopkinson Bar An Electromagnetic driven Torsional Split Hopkinson Bar, (2018).
- [107] T.J. Cloete, G. Paul, E.B. Ismail, Hopkinson bar techniques for the intermediate strain rate testing of bovine cortical bone, in: *Philos. Trans. R. Soc. A Math. Phys. Eng. Sci.*, Royal Society of London, 2014. <https://doi.org/10.1098/rsta.2013.0210>.
- [108] B. Song, C.J. Syn, C.L. Grupido, W. Chen, W.Y. Lu, A Long Split Hopkinson Pressure Bar (LSHPB) for intermediate-rate characterization of soft materials, *Exp. Mech.* 48 (2008) 809–815. <https://doi.org/10.1007/s11340-007-9095-z>.
- [109] Instron, High Strain Rate VHS System, Data Sheet. (2016) 1–4.

<https://www.instron.us/-/media/literature-library/products/2019/05/vhs-high-strain-rate-system-pod.pdf?la=en>.

- [110] shimadzu, Impact Testing, (n.d.).  
<https://www.shimadzu.com/an/test/impact/index.html>.
- [111] ISO 26203-1:2018, Metallic materials — Tensile testing at high strain rates — Part 1: Elastic-bar-type systems, (n.d.) 32. <https://www.iso.org/standard/72573.html>.
- [112] ISO 26203-2:2011, Metallic materials — Tensile testing at high strain rates — Part 2: Servo-hydraulic and other test systems, (n.d.) 15.  
<https://www.iso.org/standard/46275.html>.
- [113] M.M. Leblanc, D.H. Lassila, A hybrid technique for compression testing at intermediate strain rates, *Exp. Tech.* 20 (1996) 21–24.
- [114] B. Song, B. Sanborn, J. Heister, R. Everett, T. Martinez, G. Groves, E. Johnson, D. Kenney, M. Knight, M. Spletzer, Development of “dropkinson” Bar for Intermediate Strain-rate Testing, in: *EPJ Web Conf., EDP Sciences*, 2018.  
<https://doi.org/10.1051/epjconf/201818302004>.
- [115] C. Froustey, M. Lambert, J.L. Charles, J.L. Lataillade, Design of an impact loading machine based on a flywheel device: Application to the fatigue resistance of the high rate pre-straining sensitivity of aluminium alloys, *Exp. Mech.* 47 (2007) 709–721.  
<https://doi.org/10.1007/s11340-007-9082-4>.
- [116] J.L. Sturges, B.N. Coler, The flying wedge: A method for high-strain-rate tensile testing. Part 1. Reasons for its development and general description, *Int. J. Impact Eng.* 25 (2001) 251–264.
- [117] J. Jing, F. Gao, J. Johnson, F.Z. Liang, R.L. Williams, J. Qu, Brittle versus ductile failure of a lead-free single solder joint specimen under intermediate strain rate, *IEEE Trans. Components, Packag. Manuf. Technol.* 1 (2011) 1456–1464.  
<https://doi.org/10.1109/TCPMT.2011.2146259>.
- [118] S. Mandal, M. Jayalakshmi, A.K. Bhaduri, V. Subramanya Sarma, Effect of Strain Rate on the Dynamic Recrystallization Behavior in a Nitrogen-Enhanced 316L(N), *Metall. Mater. Trans. A Phys. Metall. Mater. Sci.* 45 (2014) 5645–5656.

- <https://doi.org/10.1007/s11661-014-2480-1>.
- [119] Z.Y. Liu, T.T. Huang, W.J. Liu, S. Kang, Dislocation mechanism for dynamic recrystallization in twin-roll casting Mg-5.51Zn-0.49Zr magnesium alloy during hot compression at different strain rates, *Trans. Nonferrous Met. Soc. China (English Ed.* 26 (2016) 378–389. [https://doi.org/10.1016/S1003-6326\(16\)64126-2](https://doi.org/10.1016/S1003-6326(16)64126-2).
- [120] R. Bardenheier, G. Rogers, Dynamic impact testing with servohydraulic testing machines, *J. Phys. IV JP.* 134 (2006) 693–699. <https://doi.org/10.1051/jp4:2006134107>.
- [121] D. Zhu, S.D. Rajan, B. Mobasher, A. Peled, M. Mignolet, Modal Analysis of a Servo-Hydraulic High Speed Machine and its Application to Dynamic Tensile Testing at an Intermediate Strain Rate, *Exp. Mech.* 51 (2011) 1347–1363. <https://doi.org/10.1007/s11340-010-9443-2>.
- [122] S. Sahraoui, J.L. Lataillade, Analysis of load oscillations in instrumented impact testing, *Eng. Fract. Mech.* 60 (1998) 437–446. [https://doi.org/10.1016/S0013-7944\(98\)00024-1](https://doi.org/10.1016/S0013-7944(98)00024-1).
- [123] M.S. Found, I.C. Howard, A.P. Paran, Interpretation of signals from dropweight impact tests, *Compos. Struct.* 42 (1998) 353–363. [https://doi.org/10.1016/S0263-8223\(98\)00080-4](https://doi.org/10.1016/S0263-8223(98)00080-4).
- [124] R. Othman, P. Guégan, G. Challita, F. Pasco, D. LeBreton, A modified servo-hydraulic machine for testing at intermediate strain rates, *Int. J. Impact Eng.* 36 (2009) 460–467. <https://doi.org/10.1016/j.ijimpeng.2008.06.003>.
- [125] R. Othman, Wave separation techniques, in: *Kolsk. Bar Mach. Sel. Top.*, Springer International Publishing, 2018: pp. 183–203. [https://doi.org/10.1007/978-3-319-71919-1\\_7](https://doi.org/10.1007/978-3-319-71919-1_7).
- [126] R. Othman, *The Kolsky-Hopkinson bar machine: Selected topics*, Springer International Publishing, 2018. <https://doi.org/10.1007/978-3-319-71919-1>.
- [127] R. Othman, M.-N. Bussac, P. Collet, G. Gary, Séparation et reconstruction des ondes dans les barres élastiques et viscoélastiques à partir de mesures redondantes Separation and rebuilding of waves in elastic and viscoelastic bars using redundant measures,

- 2001.
- [128] N. Perogamvros, T. Mitropoulos, G. Lampeas, Drop Tower Adaptation for Medium Strain Rate Tensile Testing, *Exp. Mech.* 56 (2016) 419–436. <https://doi.org/10.1007/s11340-015-0112-3>.
- [129] M. Tulke, C. Scheffler, V. Psyk, D. Landgrebe, A. Brosius, Principle and setup for characterization of material parameters for high speed forming and cutting, in: *Procedia Eng.*, Elsevier Ltd, 2017: pp. 2000–2005. <https://doi.org/10.1016/j.proeng.2017.10.1058>.
- [130] I.M. Daniel, J.L. Abot, P.M. Schubel, J.J. Luo, Response and Damage Tolerance of Composite Sandwich Structures under Low Velocity Impact, *Exp. Mech.* 52 (2012) 37–47. <https://doi.org/10.1007/s11340-011-9479-y>.
- [131] A. Manjoine, M.; Nadai, High-speed tension tests at elevated temperatures, *Proc. ASTM.* 40 (1940) 822–837.
- [132] M.F. Quinlan, M.T. Hillery, High-strain-rate testing of beryllium copper at elevated temperatures, *J. Mater. Process. Technol.* 153–154 (2004) 1051–1057. <https://doi.org/10.1016/j.jmatprotec.2004.04.013>.
- [133] R. Bouix, P. Viot, J.-L. Lataillade, Polypropylene foam behaviour under dynamic loadings: Strain rate, density and microstructure effects, (2009). <https://doi.org/10.1016/j.ijimpeng.2007.11.007i>.
- [134] P. Viot, Hydrostatic compression on polypropylene foam, *Int. J. Impact Eng.* 36 (2009) 975–989. <https://doi.org/10.1016/j.ijimpeng.2008.11.010>.
- [135] W.O. Soboyejo, T.S. Srivatsan, *Advanced Structural Materials: Properties, Design Optimization, and Applications*, illustrate, CRC Press, Boca Raton, Florida, United States, 2006.
- [136] Y. Xia, J. Zhu, K. Wang, Q. Zhou, Design and verification of a strain gauge based load sensor for medium-speed dynamic tests with a hydraulic test machine, *Int. J. Impact Eng.* 88 (2016) 139–152. <https://doi.org/10.1016/j.ijimpeng.2015.10.004>.
- [137] A.E. Groves, S.E.; Sanchez, R.J.; Lyon, R.E.; Brown, High Strain Rate Effects for



- Composite Materials, Elev. Vol. Compos. Mater. Des. Camponeschi, E., Ed.; ASTM West Conshohocken, PA, USA, (1993) 162–176.
- [138] A. Kussmaul, K.; Demler, T.; Klenk, Advanced Testing Methods for Rotating Disk Impact Machines, Mechanical Properties of Materials at High Rates of Strain, N Conf. Ser. Physics; Inst. Phys. Oxford, UK, (1989) 162–176.
- [139] P. Follansbee, Compression Testing by Conventional Load Frames., Met. Handbook, 9th Ed.; Am. Soc. Met. ASM Int. Cleveland, OH, USA. (1985) 192–193.
- [140] M. Lataillade, J.; Bacon, C.; Collombet, F.; Delaet, The benefit of Hopkinson bar techniques for the investigation of composite and ceramic materials., Wave Propag. Emerg. Technol. ASME New York, NY, USA, (1994).
- [141] M.R. Rokni, A. Zarei-Hanzaki, A.A. Roostaei, H.R. Abedi, An investigation into the hot deformation characteristics of 7075 aluminum alloy, Mater. Des. 32 (2011) 2339–2344. <https://doi.org/10.1016/j.matdes.2010.12.047>.
- [142] T.C. Joshi, U. Prakash, V. V. Dabhade, Microstructural development during hot forging of Al 7075 powder, J. Alloys Compd. 639 (2015) 123–130. <https://doi.org/10.1016/j.jallcom.2015.03.099>.
- [143] W. Xiao, B. Wang, Y. Wu, X. Yang, Constitutive modeling of flow behavior and microstructure evolution of AA7075 in hot tensile deformation, Mater. Sci. Eng. A. 712 (2018) 704–713. <https://doi.org/10.1016/j.msea.2017.12.028>.
- [144] J. Lopez, Conception et réalisation d’une machine à choc pour l’étude de la déchirure à grandes vitesses de tôle en composites, in: Mémoire Diplôme d’ingénieur Du Cent. Natl. Des Arts Métiers, 1992.
- [145] D.R. Chichili, K.T. Ramesh, K.J. Hemker, Adiabatic shear localization in  $\alpha$ -titanium: Experiments, modeling and microstructural evolution, J. Mech. Phys. Solids. 52 (2004) 1889–1909. <https://doi.org/10.1016/j.jmps.2004.02.013>.
- [146] P. Verleysen, Shear testing using the Kolsky-Hopkinson bar machine, in: Kolsk. Bar Mach. Sel. Top., Springer International Publishing, 2018: pp. 75–120. [https://doi.org/10.1007/978-3-319-71919-1\\_3](https://doi.org/10.1007/978-3-319-71919-1_3).

- [147] Z. Jian, Z. Dong, Z. Zhe, A Non-Contact Varying Temperature Strain Measuring System Based on Digital Image Correlation, *Exp. Tech.* 40 (2016) 101–110. <https://doi.org/10.1007/s40799-016-0014-z>.
- [148] J.J.O. and H.S. M. A. Sutton, *Image Correlation for Shape, Motion and Deformation Measurement*, n.d.
- [149] Y.H. Pao, High.Rate Decremental-I-Strain-Rate Test, *Exp. Mech.* (1988) 322–325.
- [150] U.S.L. and L.M. Yeakley, High Strain-rate Testing: Tension and Compression, *Exp. Mech.* 34 (1968) 1–9.
- [151] J.L. Chiddister, L.E. Malvern, Compression-impact Testing of Aluminum at Elevated Temperatures A split Hopkinson pressure-bar technique obtains stress-strain curves and stress vs. strain-rate relations for 1/4-in. long 1/2-in. diam specimens at six temperatures up to 550 ~ C, *Exp. Mech.* 3 (1963) 81–90.
- [152] A. Gilat, X. Wu, Elevated Temperature Testing with the Torsional Split Hopkinson Bar, *Exp. Mech.* . 34 (1994) 166–170.
- [153] Y. Li, K.T. Ramesh, E.S.C. Chin, The mechanical response of an A359/SiCp MMC and the A359 aluminum matrix to dynamic shearing deformations, *Mater. Sci. Eng. A.* 382 (2004) 162–170. <https://doi.org/10.1016/j.msea.2004.04.062>.
- [154] A. Nadai, *Theory of Flow and Fracture of Solids*, vol. 1, McGraw-Hill, New york, 1950.
- [155] J.H. Chen, W.F. Xu, R.Z. Xie, F.J. Zhang, W.J. Hu, X.C. Huang, G. Chen, Sample size effect on the dynamic torsional behaviour of the 2A12 aluminium alloy, *Theor. Appl. Mech. Lett.* 7 (2017) 317–324. <https://doi.org/10.1016/j.taml.2017.09.008>.
- [156] T. Rahmaan, A. Abedini, C. Butcher, N. Pathak, M.J. Worswick, Investigation into the shear stress, localization and fracture behaviour of DP600 and AA5182-O sheet metal alloys under elevated strain rates, *Int. J. Impact Eng.* 108 (2017) 303–321. <https://doi.org/10.1016/j.ijimpeng.2017.04.006>.
- [157] B. Dodd, Y. Bai, Width of adiabatic shear bands, *Mater. Sci. Technol. (United Kingdom)*. 1 (1985) 38–40. <https://doi.org/10.1179/mst.1985.1.1.38>.

- [158] G. Box, N. Draper, *Empirical Model-Building and Response Surfaces*, Wiley series in probability and mathematical statistics : Applied probability and statistics, John Wiley & Sons, 1987., 1987.
- [159] D. Doehlert, V. Klee, Experimental designs through level reduction of the d-dimensional cuboctahedron, *Discrete Math.* 2 (1972) 309–334.
- [160] D. Benoist, Y. Tourbier, S. Germain-Tourbier, *Plan d'expériences : construction et analyse.*, Lavoisier - Tec & Doc, 1994.
- [161] J. Dreesbeke, G. Saporta, J. Fine, S. de statistique de France, *Plans d'expériences : applications à l'entreprise.*, Technip, 1997.
- [162] W.-S. Lee, W.-C. Sue, C.-F. Lin, Chin-Jyi Wu Department, The strain rate and temperature dependence of the dynamic impact properties of 7075 aluminum alloy, *J. Mater. Process. Technol.* 100 (2000) 116–122.
- [163] T. Rahmaan, P. Zhou, C. Butcher, M.J. Worswick, Strain rate and thermal softening effects in shear testing of AA7075-T6 sheet, *EPJ Web Conf.* 183 (2018). <https://doi.org/https://doi.org/10.1051/epjconf/201818302037,02037>.
- [164] T. Engdahl, V. Hansen, P. Warren, K. Stiller, Investigation of fine scale precipitates in Al–Zn–Mg alloys after various heat treatments, *Mater. Sci. Eng., A.* 327 (2002) 59–64.
- [165] E. El-Magd, M. Abouridouane, Characterization, modelling and simulation of deformation and fracture behaviour of the light-weight wrought alloys under high strain rate loading, *Int. J. Impact Eng.* 32 (2006) 741–758. <https://doi.org/https://doi.org/10.1016/j.ijimpeng.2005.03.008>.
- [166] Z.C. Sun, H.L. Wu, J. Cao, Z.K. Yin, Modeling of continuous dynamic recrystallization of Al-Zn-Cu-Mg alloy during hot deformation based on the internal-state-variable (ISV) method, *Int. J. Plast.* 106 (2018) 73–87. <https://doi.org/https://doi.org/10.1016/j.ijplas.2018.03.002>.
- [167] V.G. WH, M. WZ, W. PT., Grain structure evolution in a 6061 aluminum alloy during hot torsion. ., *Mater Sci Eng A.* 419(1–2) (2006) 105–14. <https://doi.org/https://doi.org/10.1016/j.msea.2005.12.018>.

- [168] X. Yang, H. Miura, T. Sakai, Continuous Dynamic Recrystallization in a Superplastic 7075 Aluminum Alloy, 2002.
- [169] K. Huang, R.E. Logé, A review of dynamic recrystallization phenomena in metallic materials, *Mater. Des.* 111 (2016) 548–574. <https://doi.org/10.1016/j.matdes.2016.09.012>.
- [170] A. HV, B. K, V. G., Recrystallization in the semi-solid state in 7075 aluminium alloy., *Mater Sci Eng A.* 490(1–2) (2008) 266–76. <https://doi.org/https://doi.org/10.1016/j.msea.2008.01.057>.
- [171] M. Sasso, A. Forcellese, M. Simoncini, D. Amodio, E. Mancini, High strain rate behaviour of AA7075 aluminum alloy at different initial temper states, *Key Eng. Mater.* 651–653 (2015) 114–119. <https://doi.org/10.4028/www.scientific.net/KEM.651-653.114>.
- [172] U.M.R. Paturi, S.K.R. Narala, Constitutive flow stress formulation for aeronautic aluminum alloy AA7075-T6 at elevated temperature and model validation using finite element simulation, *Proc. Inst. Mech. Eng. Part L J. Mater. Des. Appl.* 230 (2016) 994–1004. <https://doi.org/10.1177/1464420715591860>.
- [173] W.. Johnson, G.R. and Cook, A Constitutive Model and Data for Metals Subjected to Large Strains, High Strain Rates, and High Temperatures, in: *Proc. 7th Int. Symp. Ballist., The Hague, 1983: pp. 541–547*.
- [174] B.D. GOLDTHORPE, Constitutive Equations for Annealed and Explosively Shocked Iron for Application To High Strain Rates and Large Strains, *Le J. Phys. IV.* 01 (1991) C3-829-C3-835. <https://doi.org/10.1051/jp4:19913116>.
- [175] D. Samantaray, S. Mandal, A.K. Bhaduri, A comparative study on Johnson Cook, modified Zerilli-Armstrong and Arrhenius-type constitutive models to predict elevated temperature flow behaviour in modified 9Cr-1Mo steel, *Comput. Mater. Sci.* 47 (2009) 568–576. <https://doi.org/10.1016/j.commatsci.2009.09.025>.
- [176] Rulexim.Ro, Produe – Rulexim, (2021). <https://rulexim.ro/produse/>.
- [177] Webtools3.Skf.Com., SKF Housing Select, (2021). <http://webtools3.skf.com/housings/search>.

- [178] Festo.Com, Products | Festo Great Britain, (2021). [https://www.festo.com/cat/en-gb\\_gb/products#](https://www.festo.com/cat/en-gb_gb/products#).
- [179] Composants.emile-maurin.fr, Goupilles industrielles de qualité - Maurin Composants, (2021). [https://composants.emile-maurin.fr/fr/elements-standard-mecaniques/elements-standard-mecaniques/centrage\\_e/serie-32\\_3\\_e/](https://composants.emile-maurin.fr/fr/elements-standard-mecaniques/elements-standard-mecaniques/centrage_e/serie-32_3_e/).

## ANNEX

### A1.Design and dimensioning of the parts required for TF1

The essential parts to design are those playing a fundamental role in the operation of the torsion device. So, in this section, the design of the coupling pin (as load fuse), the proper selection of bearing, housing and the correct selection of the pneumatic cylinder is given.

- **Spherical Roller bearing:**

The criteria to design the spherical roller bearing is based on different factors. Here, the bearings can be selected depends on the diameter of the shaft (cylindrical axle diameter), prevent the misalignment and application of load (radial and axial). It is considered that the constant rotation of the bearing.

The given data:

- $F_{\text{radial}} = 66000 \text{ N}$  (estimated according to a static calculation in a most unfavourable position when in the initial high position)
- Length of the bearing:  $L = 19 \text{ mm}$  (arbitrarily fixed to allow a good guide in rotation and checked with SKF manual guide)
- $d = 30 \text{ mm}$  (diameter of the cylindrical axle equal to the diameter of the inner case of the bearing)
- $w = 66 \text{ rad / s}$  (angular rotation of the cylindrical axle)

where:

The axial load applied on the bearings is considered as zero. All the technical data are given to the SKF bearing company to select the best bearing required for the given solution. The SKF also suggested that the spherical roller bearing is the most suitable option to guide the cylindrical axle in the rotation. The schematic diagram Figure 19 of the spherical roller bearing taken from the SKF website[176] shown below.

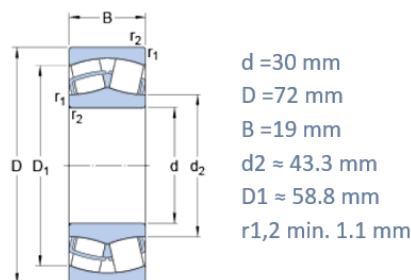


**Figure A1. 1:**The schematic diagram spherical bearing system

- **Bearing Housing Assembly:**

Bearing housing is an assembly designed to install bearings and anvil cylinder. Housings are available in many sizes and generally divided into several categories based on load, speed, and operating environmental conditions such as split Plummer (or pillow) block housings, non-split Plummer block housings, flanged housings, take-up housings and two-bearing housings.

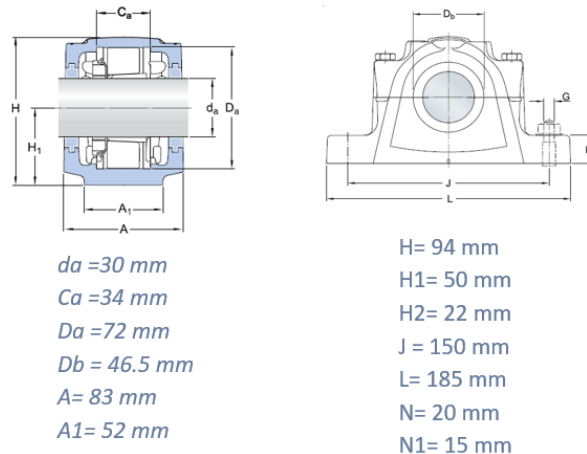


**Figure A1. 2:** Schematic diagram of Split Plummer block housing [176]

Among all the housing, the Split Plummer block housings are the most popular bearing housings on the market, considered to be the first choice for design, quality and economy. The dimension of housing is selected according to the design of a spherical roller bearing, as shown in Figure 20 [177]. The housing is fixed in the right position of the test bench. Finally, bearing and cylindrical axle are mounted on the housing. The housings can be purchased directly from the SKF company.

- **Pneumatic cylinder**

The pneumatic cylinder is a device used to position the anvil in contact with the hammer at the right moment. For every pneumatic application, 'Festo' company has a wealth of ideas to offer Standard pneumatic cylinders. The double-acting pneumatic cylinder is selected for this solution to push the anvil.


The system parameters required to select the suitable pneumatic cylinder are given below:








- The desired positioning times

- The required stroke length
- The direction of the movement (extend and retract)
- Air supply pressure
- Load setting (Moving mass)

**Partlist**

**FESTO**



Type	Designation	Part no.
 ADN-25-30-A-P-A	compact cylinder	536256
 GRLA-M5-QS-4-D	one-way flow control valve	193138
 PUN-H-4X0,75-BL	plastic tubing	197383
 CRQSL-M5-4	push-in L-fitting	162870
 VUVG-L10-M52-RT-M5-1P3	solenoid valve	566457
 CRQSL-M5-4	push-in L-fitting	162870
 PUN-H-4X0,75-BL	plastic tubing	197383

**Figure A1. 3:**Part list of the pneumatic cylinder [177]

The installation time required to position the anvil in contact with the flywheel hammer is less than 0.3 sec (minimum time the flywheel can take to complete one rotation). The stroke length of the pneumatic cylinder must be equal to the exact displacement of an anvil to be in contact with a hammer, which is almost 30mm. The direction of the movement is linear in both direction (extend and retracted); it allows to retract the anvil to its original position at the end of the test. Air pressure inside the cylinder is considered as 8 bar to move the mass of 400gm of the anvil. The Festo provided the following components to carry out the installation of the pneumatic cylinder based on the above parameters [178].

- **Coupling Pin:**

The coupling pin is a machine element used to connect a rotating element to a shaft. The pin prevents relative rotation between the two parts and may enable torque transmission. For a pin to function, the shaft and rotating element must have a slot, which is the pocket in which the pin fits. The coupling pin is also called a load fuse when it is used for preventing the damage to the system.

For the given case, the coupling pin is chosen as a full solid pin instead of the hollow pin to avoid sagging after the test, and it will be easy to extract from the shaft. The material used



to design the coupling pin is steel material; it has high elastic resistance property. The schematic diagram of the coupling pin is shown below.

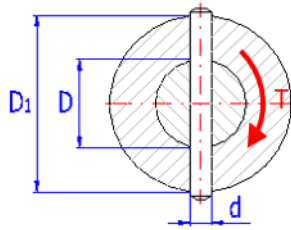


**Figure A1. 4:**Coupling pin, Loading with the torsional moment.

Given:

The torque (T) is applied by the shaft (D) to transfer the angular moment to the external shaft ( $D_1$ ) through a coupling pin with a diameter of d. The applied torque, in this case, is based on the maximum torque required to break the specimen.

- Torque (T) = =1000 Nm. (torque requires to break the specimen made up of IN718)
- The diameter of the shaft (D)= 30mm
- The diameter of the external shaft ( $D_1$ ) = 45mm
- A tangential force applied by the shaft ( $F_t$ ) =  $\frac{T}{D/2} = 66$  kN is obtained.

Where:

- Shear stress applied to the coupling pin ( $\tau$ ) =  $\frac{F_t}{A_{pin}}$
- The allowable shear stress for the hard steel cast material is  $R_e=480\text{N/mm}^2$  [179]

To design the coupling pin:

- The allowable shear stress must be maximum than applied shear stress:

$$\circ \tau = \frac{F_t}{A_{pin}} < R_e$$

- Area of coupling pin under shear stress:

$$\circ A_{pin} = \frac{\pi * d^2}{4}$$

- Hence, the minimum radius of the coupling pin is

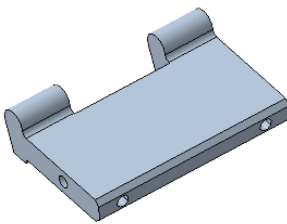
$$\circ d = \sqrt{\frac{F_t}{\pi * R_e}} \sim 10\text{mm}$$

The coupling pin diameter required to break the specimen is 10mm.

- **3D Design model**

The 3D parts of the torsion device are designed using the CATIA® V5 software. The 3D design easily defines the dimensions of the parts and their relationships. It will help to visualize the working principle of each component, including its movement and mechanical relation. The description of each 3D components of the torsion device is explained below in more detailed, including their mechanism:

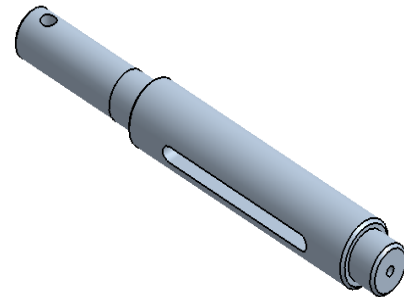
### 1) Anvil



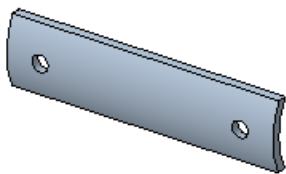
The anvil is one of the most important parts of the torsion device where the hammer impinges the anvil to transfer the rotational moment. The curved profile is designed on the crenelated shape of the anvil. The curve profile of anvil is the path traced by a point during impact rolls without slipping on the circumference of a hammer. The

### 2) Cylindrical axle

The cylindrical axle transmits the torque from the anvil to the specimen. The entire anvil will be inserted into the cylindrical axle through the groove. The gap between the width of the groove and the width of the anvil is kept as small as possible, so that

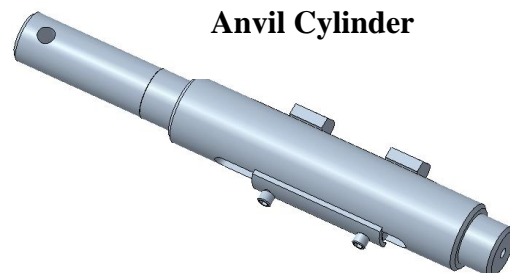


### 3) Anvil Holder



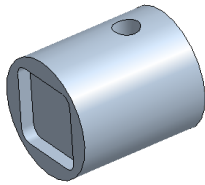
It is important to fix the anvil in the cylindrical axle by maintaining the free sliding movement of the anvil inside the groove. The solution is to place the anvil holder behind the anvil part, and

The mounting of the anvil cylinder shows that the anvil holder fixes the anvil on the rear side of the anvil within the groove section of the cylinder axle.



**Anvil Cylinder**

#### 4) Clamp (Specimen and anvil cylinder)



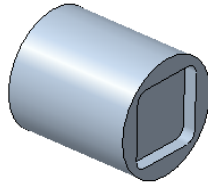
The clamp is placed between the anvil cylinder and the specimen by means of a coupling pin to transfer the rotational movement to the specimen. It is clearly observed that the square notch in the clamp used to fix the sample. The clamp also helps to protect the torsion

#### 5) Coupling pin

The coupling pin is designed to transfer the limited amount of shear load to the specimen. The coupling pin rotates the specimen until it reaches the maximum shear load. If the load reaches the critical value, it disconnects the specimen from the anvil cylinder in order to protect from the catastrophic damage to the torsion device.



#### 6) Clamp (Specimen and Hopkinson bar)



The clamp is designed to hold the specimen firmly and the other end is connected to the Hopkinson bar;

#### 7) Hopkinson bar

---

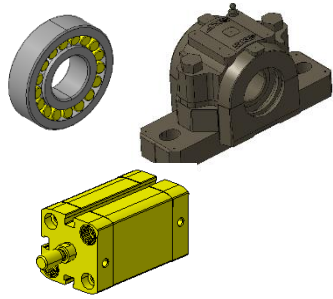
The Hopkinson bar is a long brass bar used for a torque transducer. It is connected to the sample by clamping. It is supported by the rod holder. Teflon is used to create a

#### 8) Connecting bar



The connecting rod connects the pneumatic cylinder and the anvil via the cylinder axle. It transfers the translational movement of the pneumatic cylinder to the anvil so that it slides

### 9) Bearing, housing and pneumatic cylinder



Bearing are designed to guide the anvil cylinder into rotation. In the present study, the spherical roller bearings are selected for high impact loading. The housing is an assembly designed to make it easy to install bearings and anvil cylinder.

The pneumatic cylinder is a device used to position the anvil in contact with the hammer at the right moment by sliding the anvil in groove section of the cylindrical axle. All these components are directly purchased from the retail shop.

### A2.Review of intermediate strain rate testing devices

As a result of this research work, based on chapter 1, the review paper is published in scientific journal. A general description of the testing device is systematically reviewed, which includes the working principles, some critical theories, technological innovation in load measurement techniques, components of the device, basic technical assumption, and measuring techniques. In addition, some research direction on future implementation and development of an intermediate strain rate apparatus is also discussed in detail.

✓ "Review of Intermediate Strain Rate Testing Devices" *Metals* 10, no. 7: 894.

### A3.New test bench development

Design procedure and development of the new torsion device is presented in the following deliverable 1.5 and the paper is under review based on the chapter 2.

✓ D 1.5 New Experimental Test Bench Development:Torsion Device.

✓ “Design and validation of new torsion test bench for intermediate strain rate testing”. Under Revision in International Journal of Impact Engineering.

#### **A4.New test procedure to perform simple shear test using compression/tensile apparatus at high temperature**

At the beginning of the thesis, we have decided to perform a new alternative method to perform shear tests using traditional tensile and compression test device. So, we designed an appropriate shear compression/tensile specimen in order to obtain a dominant shear at high temperature in addition to the design of new torsion testing device. However, the experimental tests performed on these specimens are in quasi-static not in dynamic. Two papers are accepted for publication based on this method, the first in a scientific journal and the second in an international conference:

- ✓ “Experimental characterization of the AA7075 aluminum alloy using hot shear compression test”. *Archiv.Civ.Mech.Eng* 21, 45 (2021).
- ✓ “Experimental characterization of the AA7075 aluminum alloy using hot shear tensile test”. 5th International Conference on Frontiers of Composite Materials, Melbourne.